BRAINPOWER CONGRESS 2023

ร่วมกันสร้างและขับเคลื่อนงานวิจัยขั้นแนวหน้า
สู่อุตสาหกรรมแห่งอนาคต

มหาวิทยาลัยเทคโนโลยีสุรนารี

สร้างคน ข้ามพรมแดน

Dehydrogenation of Mg-Fe-Ni-H based hydrogen storage tank under different operating temperatures and hydrogen flow rates

Praphatsorn Plerdsranoy, Palmarin Dansirima, and Rapee Utke*

School of Chemistry, Institute of Science, Suranaree University of Technology, Nakhon Ratchasima 30000, Thailand:
Phone +66 87877 6398, Email: praphatsorn@sut.ac.th

Introduction:

From our previous work, $Mg_2Fe_{(1-x)}Ni_xH_6$ hydrides were synthesized by compositing Mg_2FeH_6 with Mg_2NiH_4 (2:1, 1:1, and 1:2 mole ratios). Ni substitution degree increased from x=0.26 to 0.47 with Mg_2NiH_4 contents during sample preparation and was constant at x = 0.5 upon cycling, resulting in reversible capacities in the range of 2.70-3.15 wt. % H_2 (T=280 °C). Compared with Mg_2FeH_6, all $Mg_2Fe_{(1-x)}Ni_xH_6$ showed fast kinetics with the reduced onset desorption temperature (ΔT= up to 45 °C). Since Mg_2FeH_6-Mg_2NiH_4 composite with 1:1 mole ratio prepared in laboratory scale showed the highest reversible hydrogen contents upon 6 cycles (2.90-3.15 wt. % H_2), this sample is selected for upscaling to the small tank[1].

Objectives:

1. To upscale the Mg-Fe-Ni hydride from Lab scale (~3 g sample) to a small hydrogen storage tank (~60 g sample mass) with a packing volume of ~96 mL.
2. To study the effects of operating and hydrogen release rates on kinetics and de/rehydrogenation mechanisms of Mg-Fe-Ni-H based tank.

[1] Plerdsranoy P, et al. J Alloys Compd 2023;937:168212. https://doi.org/10.1016/J.JALLCOM.2022.168212.

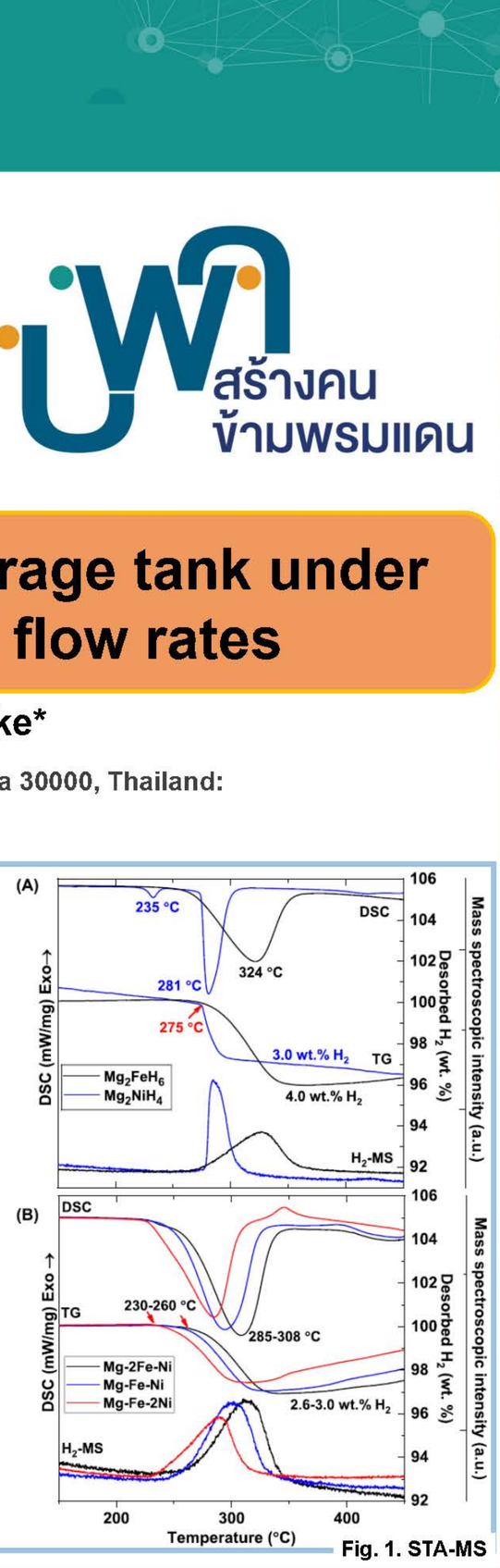

Fig. 1. STA-MS

Sample preparation and characterization

Ball milling

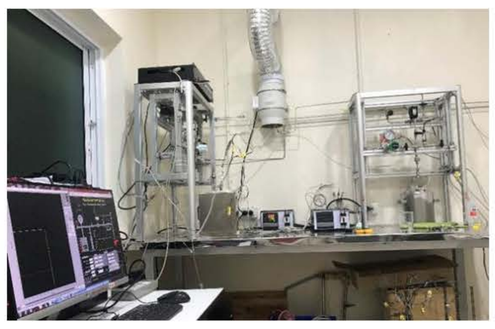

Kinetic measurement

Hydrogen storage tank with the packing volume of 96.2 mL

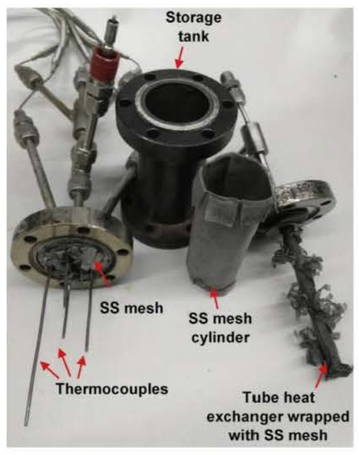

Tank components

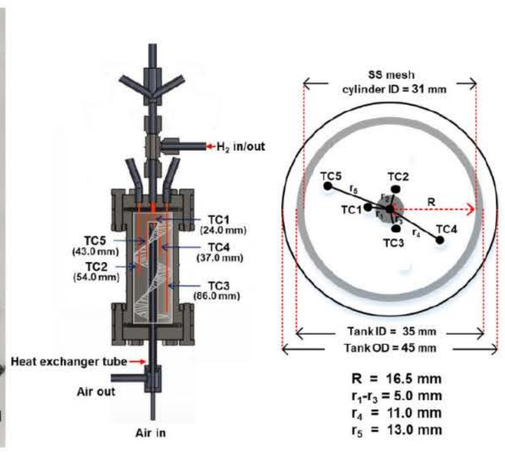

TC positions

Effect of operating temperature and H_2 release rate

[1] Dehydrogenation profiles during kinetic measurement

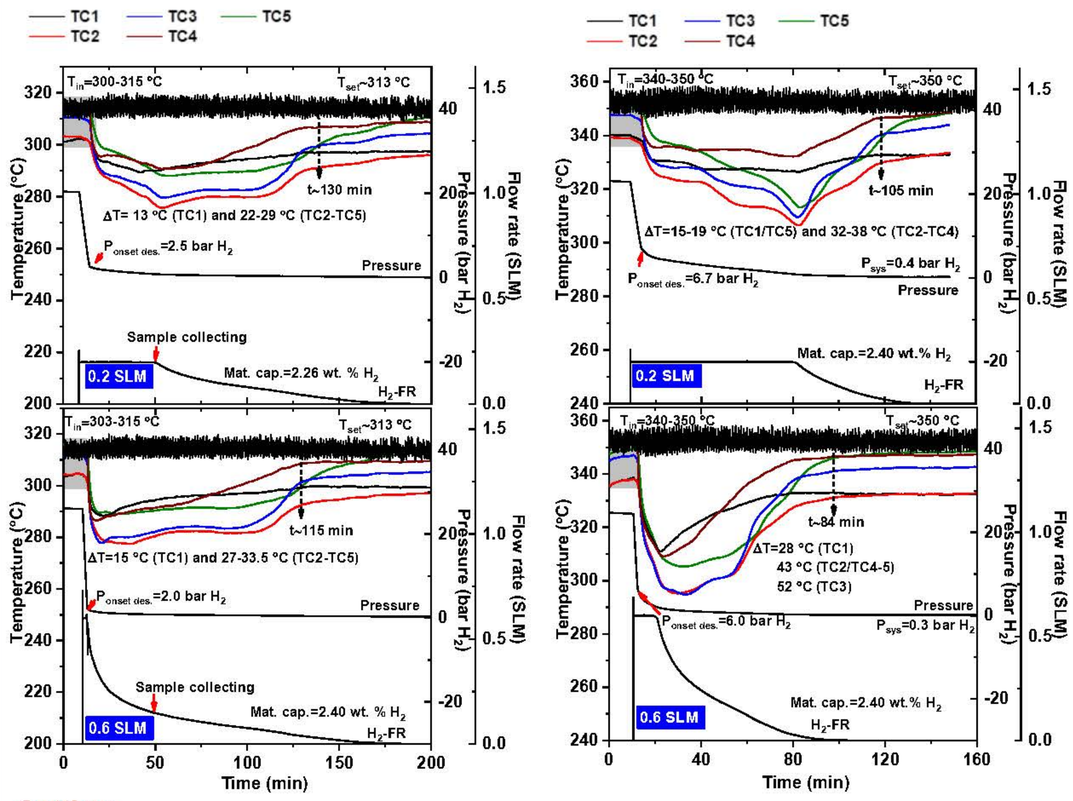

Setting temperature: 310 °C 350 °C

Effect of operating temperature and H_2 release rate

[2] Dehydrogenation kinetics under different temperatures and H_2 flow rates

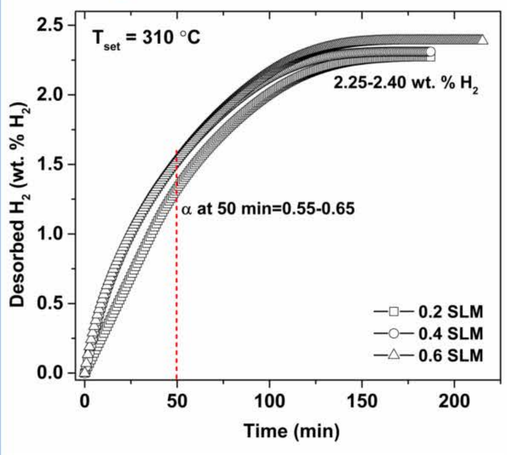

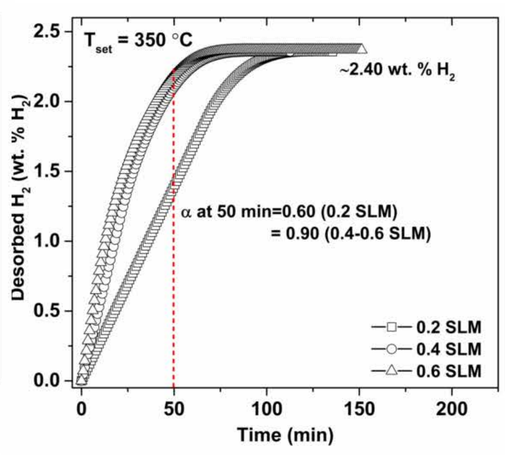

[3] Reversible hydrogen capacities

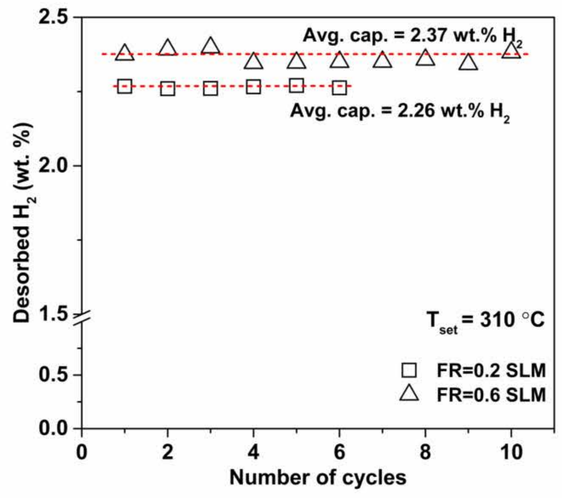

Conclusions

- ✓ At low operating temperatures, the H_2-FR does not affect the reaction rate significantly.
- ✓ The experiment with high operating temperature, resulting in the enhanced decomposition rate requires fast H_2-FR to reach the best dehydrogenation kinetics.

Acknowledgement

This research has received the funding support from (i) Suranaree University of technology (SUT) and (ii) the NSRF) via the Program Management Unit for Human Resources & Institutional Development, Research and Innovation (PMU-B) [grant numbers: B13F660067].

BRAINPOWER CONGRESS 2023

ร่วมกันสร้างและขับเคลื่อนงานวิจัยขั้นแนวหน้า
สู่อุตสาหกรรมแห่งอนาคต

ปพ. สร้างคน ข้ามพรมแดน

A PROTOTYPE DEVELOPMENT OF AN ONLINE AIRBORNE PARTICULATE MONITORING STATION

-Postmaster Researcher (First author)
Wisanapat Rattanachan

-Principle investigator (Corresponding author)
Assoc. Prof. Dr.Panich Intra

-Sompol Tarchai (T&P INNOVATION CO., LTD.)

-(Affiliation)Chiang Mai University,
Rajamangala University of Technology Lanna

RATIONALE / PROBLEM STATEMENT / INTRODUCTION

The northern air pollution problem Dust or micro particles smaller than 2.5 (PM2.5) and 10 (PM10) in the air cause health effects. Increase the number of illnesses and deaths. Both in the general public and at-risk groups, including young children and the elderly People with chronic respiratory illnesses, heart disease, etc., therefore need to use accurate measuring and sampling tools to collect data continuously. To indicate the amount and source of this dust, which is important information to carry out control, prevention, alertness, and improvement. Environmental quality These dust measuring instruments that are used and sold in Thailand are currently being produced and imported entirely from foreign countries. Since there is no production of commercial dust measuring tools in Thailand, causing a lot of expenses Therefore, the development of a prototype of a low-cost online aerosol measurement station by using appropriate technology and materials 100% manufactured in assembly, installation, and construction from the country. The machine is designed to be convenient to move and durable. Suitable for field work

METHODS

1.Design and build a network of air quality measurement stations and fire haze alarms. That can be measured as follows: PM10, PM2.5

2. Install and test the field, measure, and collect prototype samples with machines that use the FRM (federal reference method) state correlation method in accordance with the United States Environmental Protection Agency (U.S. EPA) by continuously collecting samples in the air for 24 hours. Bring the values that compare the measurement results. Analyze data by finding the relationship between the measurement results from the analyzer and the reference method meter using the Pearson correlation method.

RESULTS & DISCUSSION

Compared with automatic and semi-automatic tools that can report results immediately, the tape system meter, expert emission, and microbalance (Tapered Element Oscillating Microbalance) found that the prototype of the aerosol measurement station online is low-cost. Can detect and collect dust samples in the air, both PM10 and PM2.5 dust, quickly, with a processing time of up to 0.1 seconds.

CONCLUSION

Developing a prototype of a low-cost online aerial aerosol measurement station That uses the principle of measuring static electricity of particles through high-performance dust filters, able to quickly detect and collect dust samples in the air, both PM10 and PM2.5 dust, takes up to 0.1 seconds to process technology. And the right material to actually work is about three times cheaper but can work comparable to the tools currently used. With data for measuring PM2.5 and PM10, it can also be utilized in the calculation or forecasting model, forecasting the quantity and behavioral motion of near dust. Real-time in the future.

ACKNOWLEDGEMENTS

This research has received funding support from the NSRF via the Program Management Unit for Human Resources & Institutional Development, Research and Innovation grant number B13F660068

BRAINPOWER CONGRESS 2023

ร่วมกันสร้างและขับเคลื่อนงานวิจัยขึ้นแนวหน้า
สู่อุตสาหกรรมแห่งอนาคต

RMUTT สร้างคน ข้ามพรมแดน
www.rmutt.ac.th ราชมงคลธัญบุรี

CLEAN CARE CONCEPT MANUFACTURING CO., LTD.

Fabrication of cellulose-based capsule containing fragrances via interfacial photo-initiated crosslinking for used in fabric softener products

Latdamanee Phutthatham[1], Preeyaporn Chaiyasat[1,2] and Amorn Chaiyasat[1,2*]
[1]Department of Chemistry, Faculty of Science and Technology, Rajamangala University of Technology Thanyaburi, Pathum Thani, Thailand 12110
[2]Advanced Materials Design Development (AMDD) Research, Institute of Research and Development,
Rajamangala University of Technology Thanyaburi, Pathum Thani, Thailand 12110
*E-Mail: a_chaiyasat@mail.rmutt.ac.th (Phone +66 2549 3536, Fax +66 2549 3526)

1 Introduction

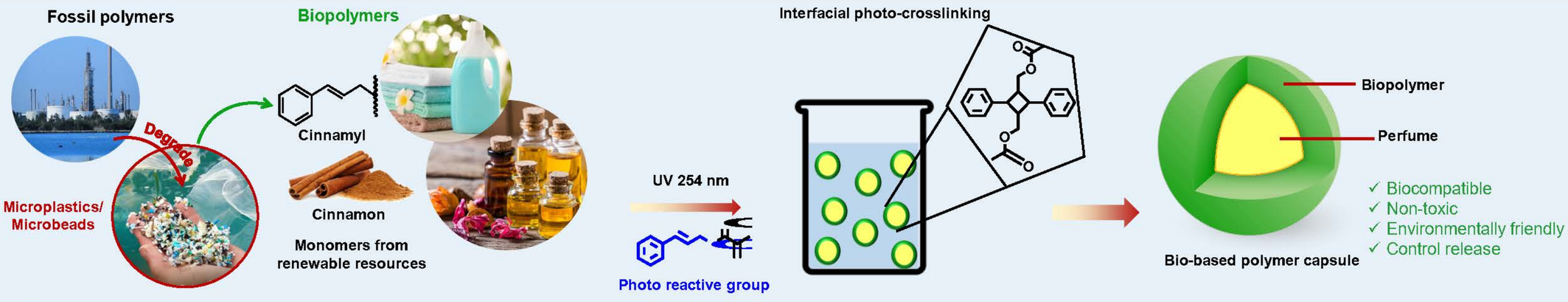

2 Methods

2.1 Preparation of the bio-based monomers

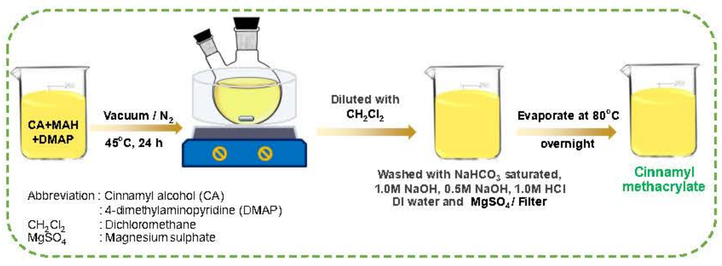

2.2 Synthesis of bio-based polymer

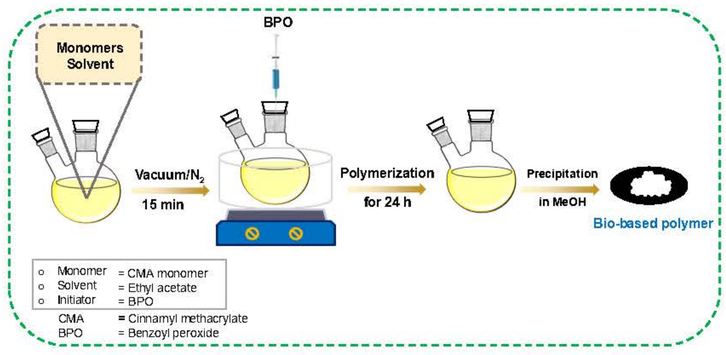

2.3 Preparation of bio-based polymer microcapsule

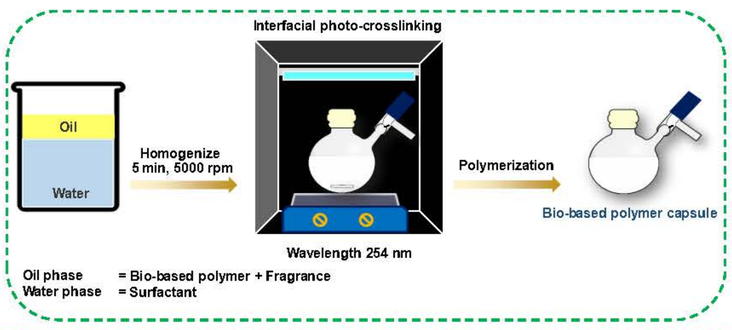

3.2 Preparation of bio-based polymer

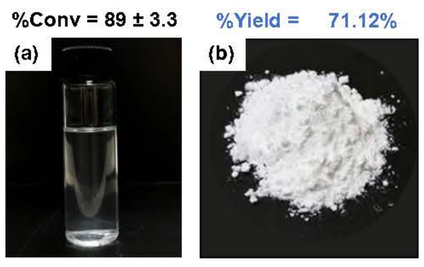

Fig.3 Bio- based solution of PCMA (a) and after purification (b)

3 Conclusions

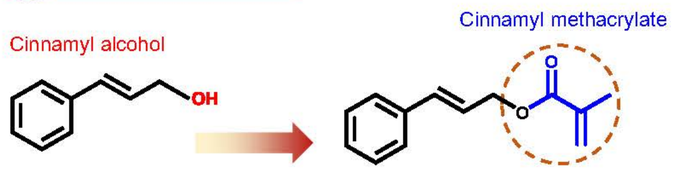

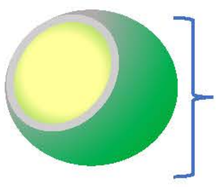

Successfully modify CMA monomer, synthesize PCMA polymer and produce PCMA/Perfume microcapsule with photoirradiation

5 Acknowledgements

This research has received funding support from the NSRF via the Program Management Unit for Human Resources & Institutional Development, Research and Innovation [grant number B13F660068

3 Result and Discussion

3.1 Preparation of the bio-based monomers

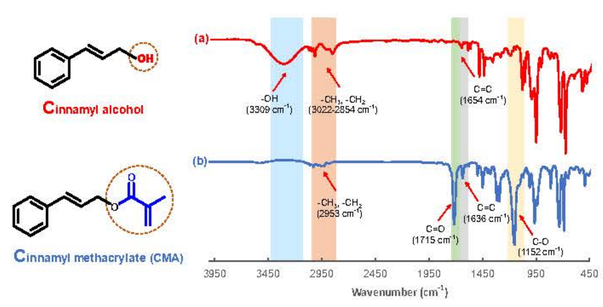

Fig. 3 FT-IR spectra of (a) cinnamyl alcohol and (b) CMA

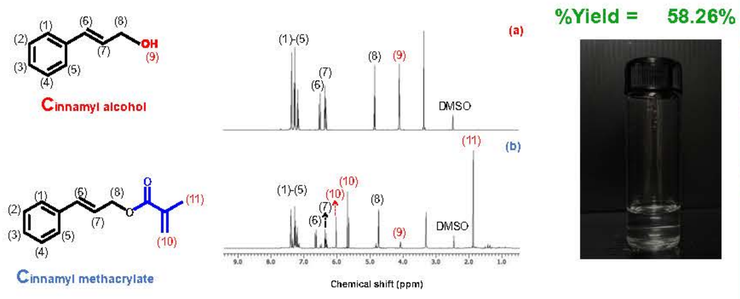

Fig. 2 ^{1}H-NMR spectra of (a) cinnamyl alcohol and (b) CMA

%Yield = 58.26%

3.3 Preparation of bio-based polymer microcapsule

➢ Time of photoirradiation

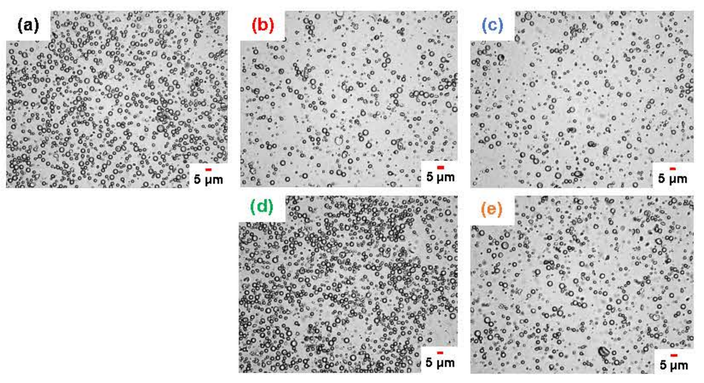

Fig. 4 Optical micrographs of PCMA Particle ; before (a) and after photo-induced crosslinking (b-e) at various times: 2h (b), 4h (c), 6h (d), and 8h (e)

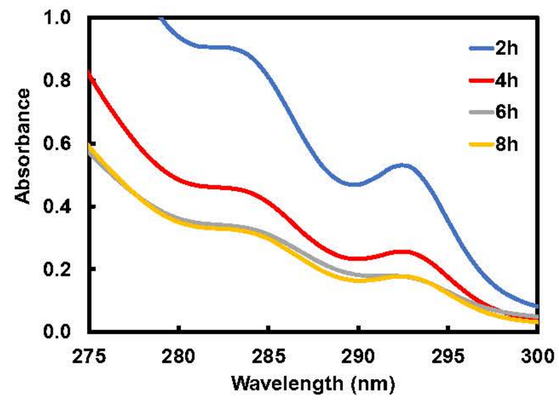

Fig. 5 UV visible spectra of poly (cinnamyl methacrylate) after photo-induced crosslinking at various times

➢ *Polymer: Perfume ratio*

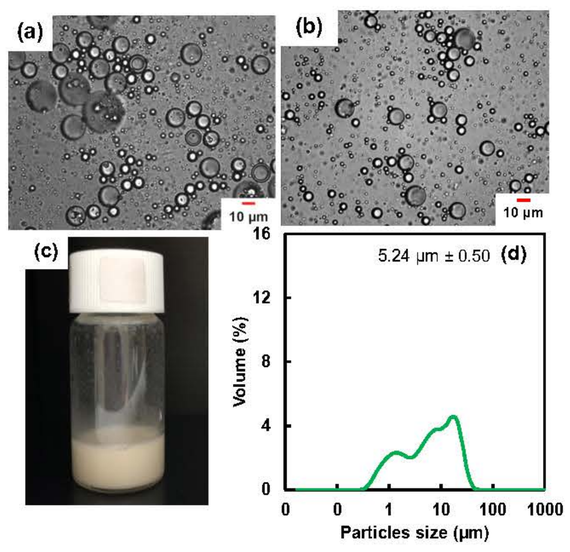

Fig. 6 Optical micrographs (a and b), suspension photo (c) and DLS histogram of polymer solution droplet (a) and microcapsule (b, c and d) after photo-induced crosslinking with 6h

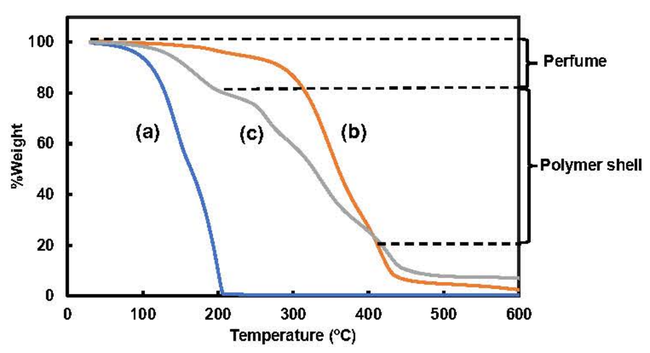

Fig. 7 TGA thermograms of perfume (a), PCMA (b) and PCMA/Perfume microcapsules after photo-induced crosslinking (c)

6 References

[1] P. Chaiyasat, S. Noppalit, M. Okubo, and A. Chaiyasat, "Innovative synthesis of high performance poly(methyl methacrylate) microcapsules with encapsulated heat storage material by microsuspension iodine transfer polymerization (ms ITP)", Solar Energy Materials and Solar Cells, vol. 157, 2016, p. 996.

[2] D. Lerari "Synthesis and Characterization of New Copolymer Based Cinnamyl Methacrylate Monomer: Determination of Monomer Reactivity Ratio and Statistical Sequence" Materials Research. 2015; 18(5): 1008-1014.

[3] Y.Kitayama, K. Yoshikawa, and T. Takeuchi "Efficient Pathway for Preparing Hollow Particles: Site-Specific Crosslinking of Spherical Polymer Particles with Photoresponsive Groups That Play a Dual Role in Shell Crosslinking and Core Shielding" Langmuir 2016, 32,9245−9253.

[4] A. B. Mapossa, W. W. Focke, R. K. Tewo, R. Androsch, and T. Kruger, "Mosquito-repellent controlled-release formulations for fighting infectious diseases", Malaria Journal, vol. 20, no. 1, 2021, p. 165

BRAINPOWER CONGRESS 2023
ร่วมกันสร้างและขับเคลื่อนงานวิจัยขึ้นแนวหน้า สู่อุตสาหกรรมแห่งอนาคต

Development of controlled-release bio-based polymer microcapsules encapsulating mosquito repellents

Kanlapangha Rattanasaikaew[1], Preeyaporn Chaiyasat[1,*] and Prachoom Rattanasaneewat[2]

[1] *Department of Chemistry, Faculty of Science and Technology, Rajamangala University of Technology Thanyaburi, Klong 6, Thanyaburi, Pathum Thani 12110, Thailand*

[2] *CLEAN CARE CONCEPT MANUFACTURING CO.,LTD., 29/3 MOO 10 Buengkamproi, Lumlukka, Pathum Thani 12150,Thailand*

** Corresponding email: (p_chaiyasat@mail.rmutt.ac.th)*

1. Introduction

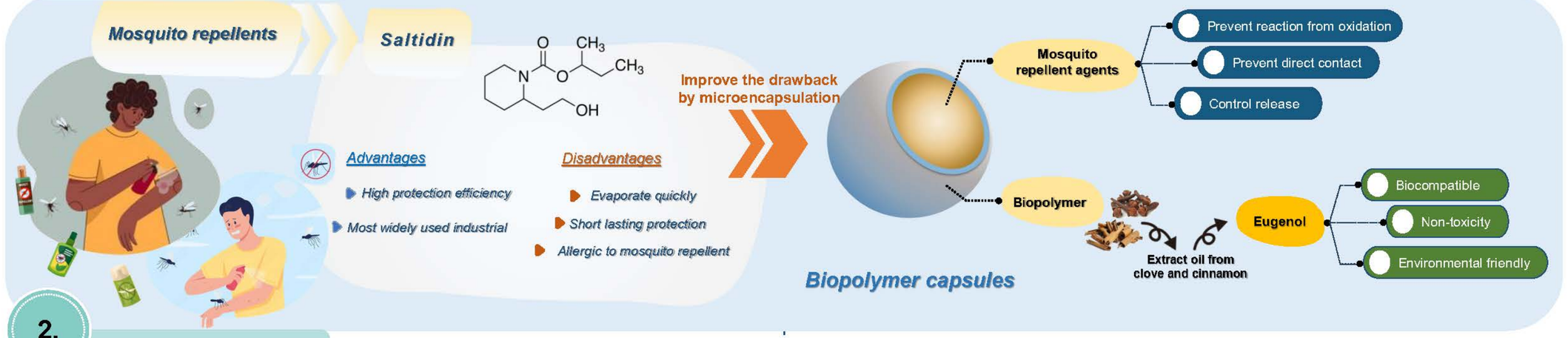

2. Methods

2.1 Preparation of bio-monomer

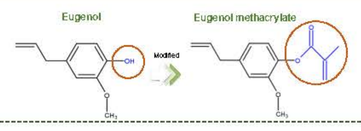

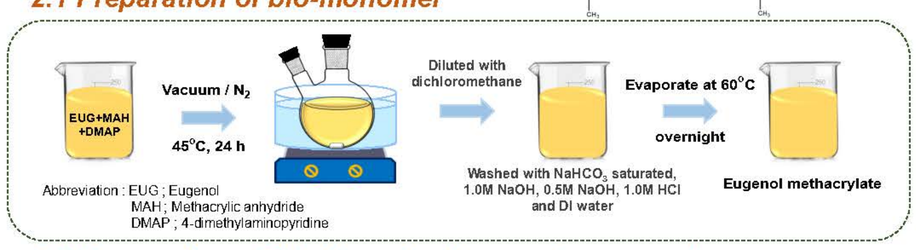

2.2 Preparation of bio-based polymer microcapsules by microsuspension polymerization

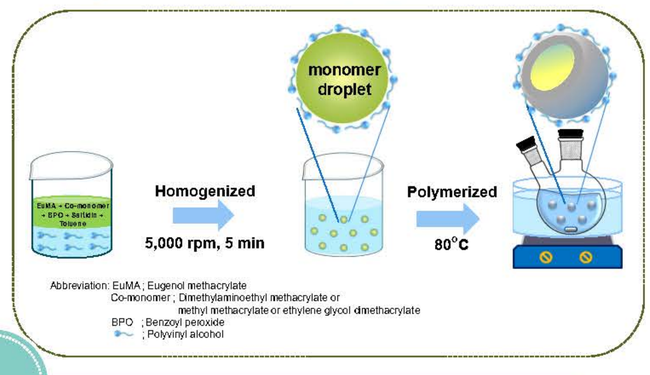

Optimization

- *Type of co-monomer*
- *Ratio of EuMA: EGDMA*
- *Ratio of monomer: saltidin*

3. Results and Discussion

3.1 Preparation of bio-monomer

%Yield = 51.36

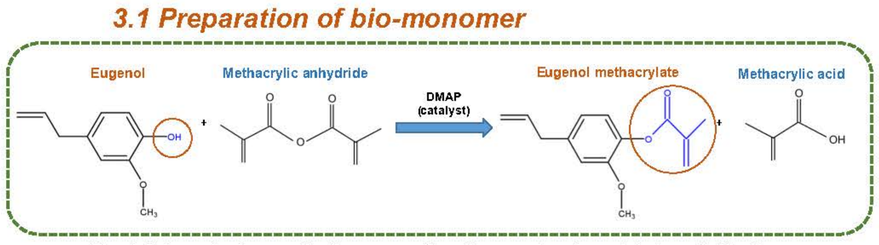

Fig. 1 Schematic diagram for the preparation of eugenol methacrylate by esterification

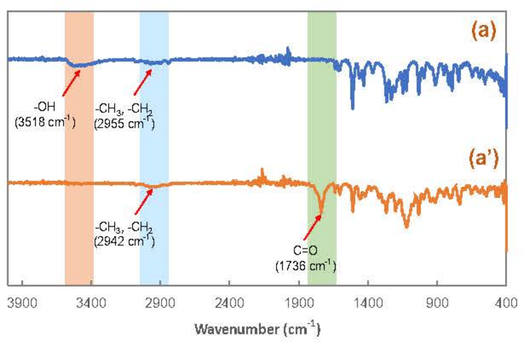

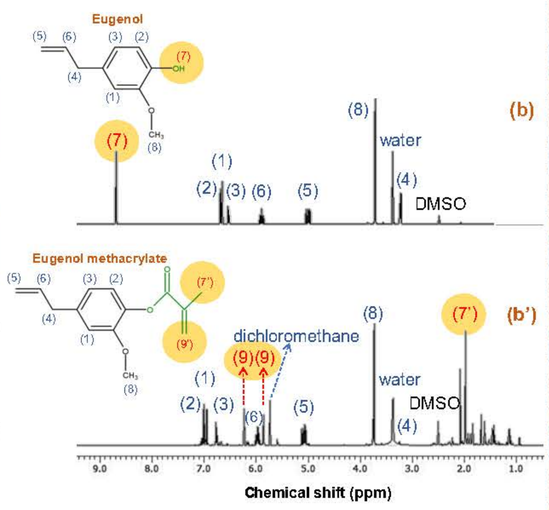

Fig. 2 FT-IR and H¹-NMR spectra of (a and b) eugenol and (a' and b') eugenol methacrylate

3.2 Preparation of bio-based polymer microcapsules by microsuspension polymerization

Type of co-monomer

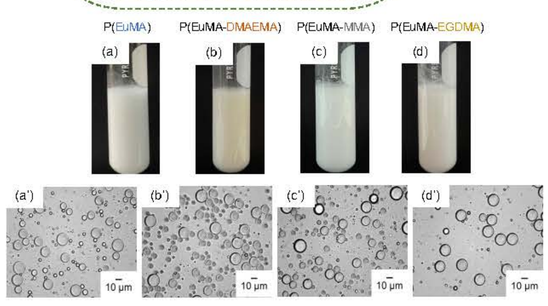

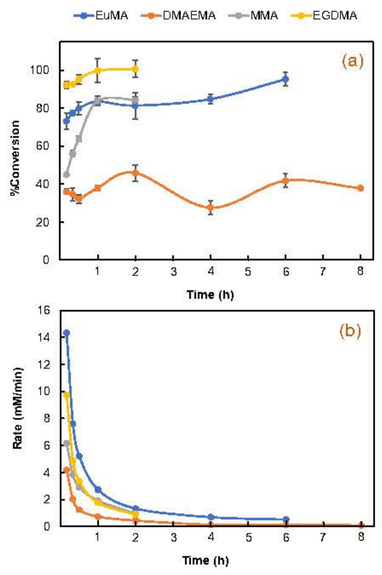

Fig. 3 Photos (a-d) and optical micrographs (a'-d') of P(EuMA-*co*-monomer)/saltidin by using various type of co-monomer; (a and a') without; (b and b') DMAEMA; (c and c') MMA and (d and d') EGDMA

Fig. 4 Conversion time curve (a) and rate of polymerization

Ratio of EuMA: EGDMA

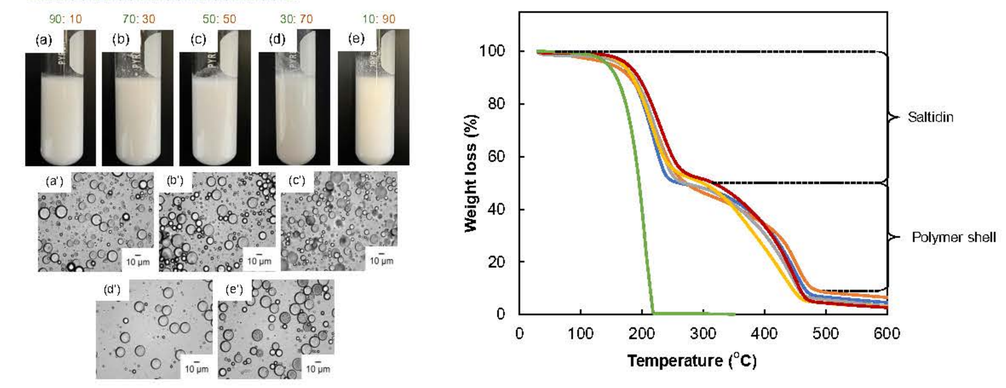

Fig. 5 Photos (a-e) optical micrographs (a'-e') and TGA thermograms of P(EuMA-*co*-EGDMA)/saltidin microcapsules

EuMA: EGDMA (wt%)	%Conversion (wt%) (±SD)	Loading (wt%)		Encapsulation (wt%)
		Experiment (±SD)	Calculation	
90: 10	56.84 (±1.91)	54.01 (±1.10)	66.41	81.32
70: 30	51.49 (±5.41)	50.95 (±0.40)	70.56	72.22
50: 50	70.19 (±1.46)	49.58 (±0.35)	60.24	82.31
30: 70	100.66 (±4.55)	46.18 (±0.89)	52.22	88.44
10: 90	81.82 (±0.79)	47.20 (±0.26)	57.07	82.71

High loading
High encapsulation

Ratio of monomer: saltidin

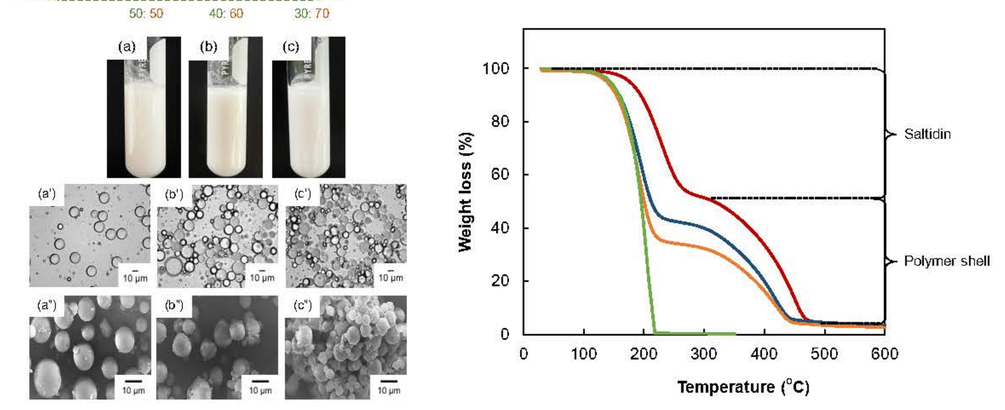

Fig. 6 Photos (a-c) optical micrographs (a'-c') SEM (a"-c") and TGA thermograms of P(EuMA-*co*-EGDMA)/saltidin microcapsules

Monomer: saltidin (wt%)	%Conversion (wt%) (±SD)	Loading (wt%)		Encapsulation (wt%)
		Experiment (±SD)	Calculation	
50: 50	100.66 (±4.55)	46.18 (±0.89)	52.22	88.44
40: 60	44.80 (±5.74)	55.31 (±2.12)	82.23	67.26
30: 70	20.24 (±11.65)	64.64 (±0.32)	114.07	56.67

High loading
High encapsulation

4. Conclusions

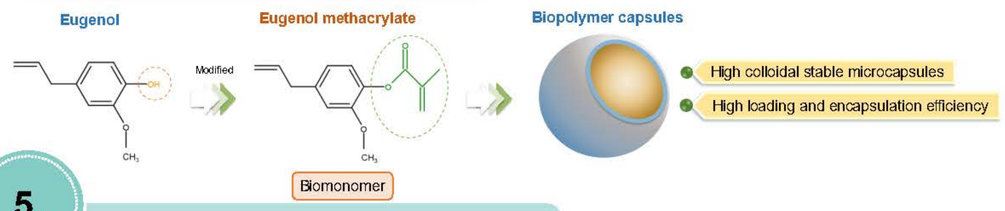

5. Acknowledgement

This research has received funding support from the NSRF via the Program Management Unit for Human Resources & Institutional Development, Research and Innovation [grant number B13F660068]

6. References

[1] A. B. Mapossa, W. W. Focke, R. K. Tewo, R. Androsch, and T. Kruger, "Mosquito-repellent controlled-release formulations for fighting infectious diseases," *Malaria Journal*, vol. 20, no. 1, 2021, p. 165

[2] P. Chaiyasat, S. Noppalit, M. Okubo, and A. Chaiyasat, "Innovative synthesis of high performance poly(methyl methacrylate) microcapsules with encapsulated heat storage material by microsuspension iodine transfer polymerization (ms ITP)," *Solar Energy Materials and Solar Cells*, vol. 157, pp. 996-1003, 2016/12/01/ 2016.

[3] D. C. Abrantes *et al.*, "Repellent active ingredients encapsulated in polymeric nanoparticles: potential alternative formulations to control arboviruses," (in eng), *J Nanobiotechnology*, vol. 20, no. 1, p. 520, 2022

BRAINPOWER CONGRESS 2023

ร่วมกันสร้างและขับเคลื่อนงานวิจัยขั้นแนวหน้า
สู่อุตสาหกรรมแห่งอนาคต

PMU-B Brainpower Congress 2023 Frontier Research to Future Industries by I conNEXT with U

Synergistic Effects of Micronanobubbles and AC/Ag-TiO_2 Nanocomposites in Photocatalysis for Enhanced Dye Treatment

Yuwadee Leelert, Orawan Rojviroon, Sumonman Naimlang, Thammasak Rojviroon, Ranjith Ranjendran, Nicharee Akechatree, Sutthida Wongwichian, Sanya Sirivithayapakorn, SDG LINK company limited

1 INTRODUCTION

Thailand possesses a substantial quantity of agricultural waste materials, sparking the notion that these resources could be leveraged to add value and address environmental pollution issues. An avenue for extending the technological applications in this realm involves the creation of composite materials with enhanced characteristics. This can be achieved by utilizing agricultural waste materials to manufacture activated carbon (AC) due to its exceptional adsorption capabilities and high porosity. Additionally, applying the photocatalyst coating to the surface in the photocatalytic process can further elevate the potential of these composite materials, resulting in improved absorption and reactivity properties. This, in turn, can facilitate the decomposition of various pollutants and contaminants that afflict the environment. The uncontrolled discharge of contaminated effluents from industrial, agriculture and community activities poses a grave and imminent threat to the ecological integrity of natural water sources. Among the diverse array of photocatalysts, titanium dioxide (TiO_2) has emerged as a standout candidate, primarily owing to its remarkable ability to harness solar energy and initiate the generation of electron-hole pairs, which, in turn, facilitate the degradation of organic contaminants..

The research paper provides a comprehensive investigation into improving the efficiency of the photocatalytic process for the treatment of dyes, pesticides, and microorganisms in wastewater. The main emphasis of the study is the development of a novel Ag-TiO_2 photocatalyst using the sol-gel method, followed by its application as a coating on AC, creating a composite material termed AC/Ag-TiO_2. This novel catalyst is expected to exhibit exceptional efficacy in the removal of challenging compound dyes, pesticides, and microorganisms from wastewater, thus mitigating their adverse impact on natural water sources. To further optimize the photocatalytic system, the research delves into the incorporation of micro-nanobubbles (MNBs), which are minute gas bubbles boasting an extensive interfacial area and extended lifetime. These MNBs serve as efficient carriers of reactive species to the catalyst surface, leading to the acceleration of the photocatalytic reaction rate, resulting in faster dyes and pesticides degradation and heightened photocatalytic efficiency. Additionally, the presence of MNBs allows for effective separation of the photocatalyst from the treated water phase, minimizing the risk of potential micro-pollution residues and the loss of photocatalyst during the wastewater treatment process. The study aspires to establish a sustainable and eco-friendly approach to wastewater treatment by synergistically incorporating innovative catalyst preparation techniques and harnessing micro-nanobubbles to enhance the photocatalytic process. The anticipated outcomes hold the potential to make significant contributions toward a cleaner and more environmentally responsible future. Photocatalysis is poised to play a pivotal role in effectively addressing the challenges posed by compound dyes, pesticides, and other recalcitrant pollutants in wastewater, ultimately promoting environmental preservation and sustainability. Through this groundbreaking research, the scientific community can pave the way for transformative advances in wastewater treatment technology, making substantial progress toward a cleaner, healthier, and more environmentally conscious world.

2 METHODS

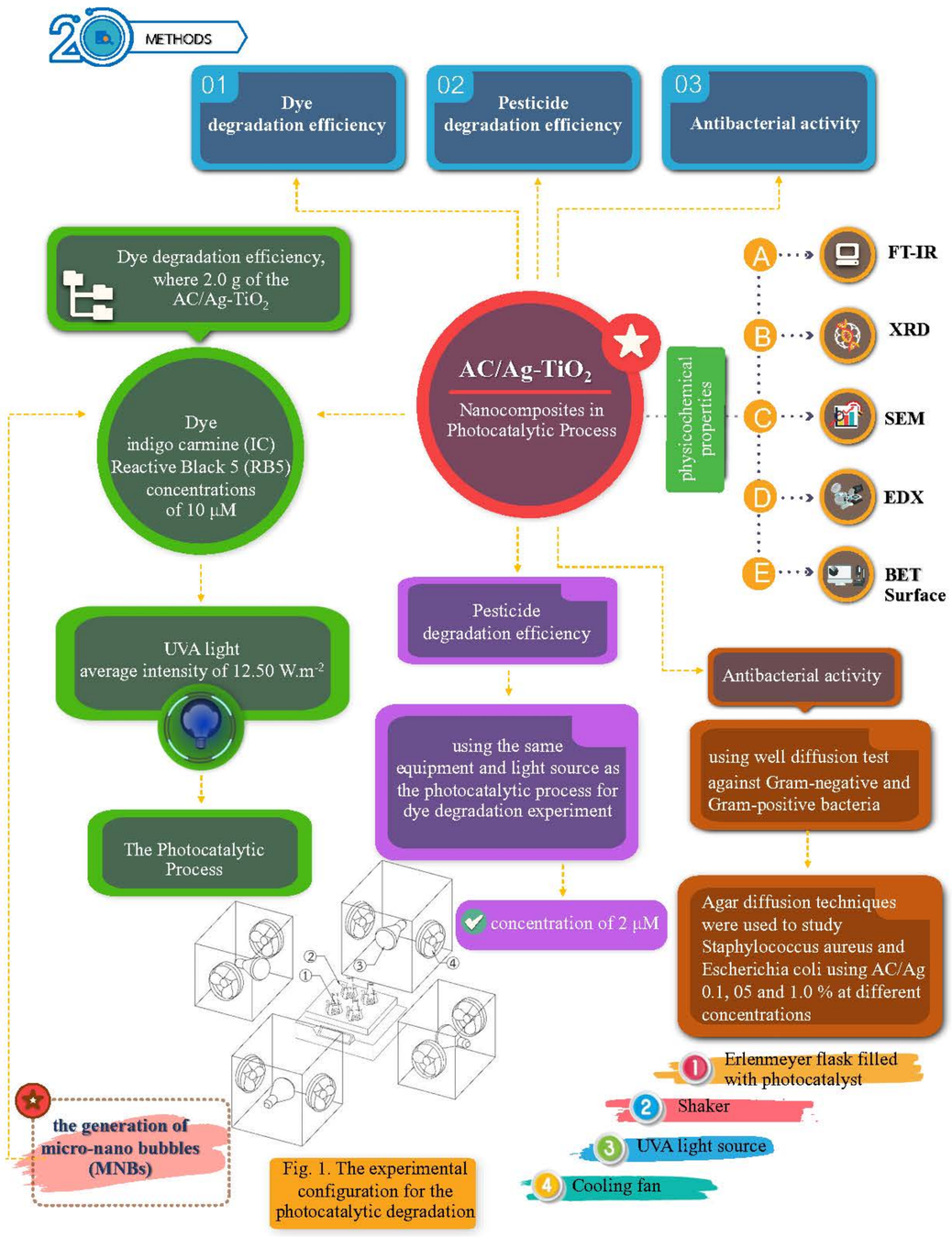

Fig. 1. The experimental configuration for the photocatalytic degradation

3 RESULTS AND DISCUSSION

Structural analysis

The crystalline structure and face purity of the synthesized AC/0.1%Ag/TiO_2 AC/0.5%Ag/TiO_2 and AC/1%Ag/TiO_2 nanocomposites, were verified using the powder X-ray diffraction (XRD) method. As shown in Fig. 2a, the data indicates that all the samples display peaks at 2θ values of 24.8° and 43.6°, which correspond to reflections in the (002) plane and (100) plane, respectively. These findings confirm the presence of the quartz phase, characterized by a two-dimensional disordered stacking of micrographites. Furthermore, when the Ag concentration increased, the XRD peaks of the AC/Ag/TiO_2 samples were slightly displaced to the lower angle side. The shift makes sense because the doped Ag ions may likely be incorporated into the AC/TiO2 lattice is not directly related to the doping concentration. However, the TiO_2 peaks did not appear due to the very low concentration of TiO_2 compared with AC. The presence of the AC/Ag/TiO_2 Photocatalyst was confirmed through EDX analysis.

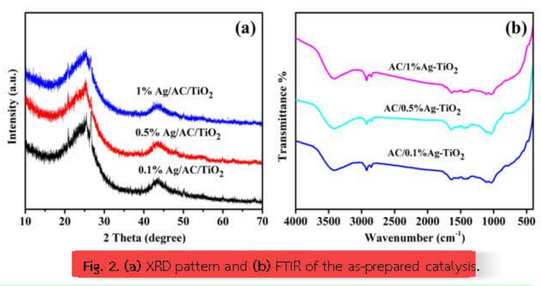

Fig. 2. (a) XRD pattern and (b) FTIR of the as-prepared catalysis.

The FTIR technique was employed to detect and identify the vibrational modes associated with the functional groups in the prepared material and the results are presented in Fig. 2. The peak observed at 3,423 cm^{-1} may be attributed to the stretching of –OH groups found in polymeric compounds or the presence of N-H groups. The peaks at 2,928 and 2,855 cm^{-1} are indicative of C–H stretching vibrations, while the peak at 1,428 cm^{-1} signifies the presence of C=C groups in carbon. The band at 1,626 cm^{-1} corresponds to the carbonyl stretching vibration of amide, likely resulting from the combined effects of double-bond stretching vibration and -NH deformation in lead-loaded activated carbon. Additionally, the minor peaks at 1,115 and 1,032 cm^{-1} suggest the presence of S=O groups. It is noteworthy that both C=O and S=O functional groups are known to exhibit strong coordination with trace metals. Furthermore, as the concentration of Ag increased in AC/Ag/TiO_2, the band shifted to lower wavenumbers, providing evidence for the presence of Ag within the AC/TiO_2 nanoparticles.

Surface morphological and elemental analysis

The surface properties and elemental composition of both the uncoated AC and the AC/Ag-TiO_2 photocatalyst are shown in Figures 3(a) and (b). The SEM images clearly depict the nanostructured surface of the activated carbon coated with the Ag-TiO_2 photocatalyst, where well-distributed nanoparticles are apparent (Fig. 3(b)). These results provide strong evidence of the successful application of Ag-TiO_2 nanoparticles onto the activated carbon surface. To provide additional details regarding the nanostructure of the AC/0.5%Ag-TiO_2 photocatalyst were conducted through high-resolution transmission electron microscopy (HR-TEM) analysis, and the findings are presented in Fig. 3. These results indicate that the nanoparticles exhibit an almost spherical shape, with particle sizes distributed within the range of 6 to 10 nanometers. In Fig. 3a and 3b clearly show the presence of dark spots on the surface of the AC in the presence of Ag-TiO_2 particles. In Fig. 3d shows the electron diffraction patterns revealing the brightness and intensity of the polymorphic discrete ring of the highly crystalline structure.

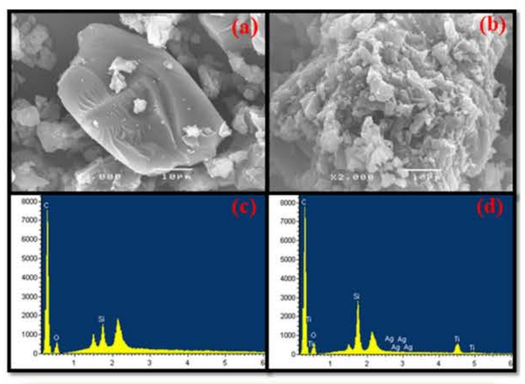

Fig. 3. SEM images for (a) uncoated AC, (b) AC/0.5%Ag-TiO_2, (c) EDX spectrum of uncoated AC (d) AC/0.5%Ag-TiO_2 photocatalyst.

Table 1 Elemental composition and BET surface property of AC/Ag-TiO_2 photocatalyst

Photocatalyst Properties		AC	AC coated with 0.1%Ag-TiO_2	AC coated with 0.5%Ag-TiO_2	AC coated with 1.0%Ag-TiO_2
Bandgap Energy (eV)		-	1.74	1.70	1.67
Composition (%)	Ti	-	2.93	3.06	2.98
	Ag	-	0.09	0.52	0.98
	C	99.14	95.81	95.26	95.44
	Si	0.86	0.77	0.83	0.41
	Al	-	0.41	0.34	0.28
BET Analysis	Surface area ($m^2 g^{-1}$)	553.98	438.89	455.44	518.03
	Pore volume ($cm^3 g^{-1}$)	0.33	0.19	0.20	0.21
	Pore size (nm)	2.41	1.52	1.51	1.51

The elemental composition and BET surface characteristics for the uncoated AC and the AC/Ag-TiO_2 photocatalyst are also included in Table 1. Fig. 2 shows the EDS image of the AC/0.5%Ag-TiO_2 photocatalyst, revealing prominent peaks corresponding to Ti and Ag with 0.74 wt% and 0.50 wt% of Ti and Ag, respectively, indicating a successful coating on the AC surface. Table 1 presents the composition of the AC coated with different amounts of Ag-TiO_2, and it also identifies the presence of other elements on the AC surface, such as carbon (C), silicon (Si), and oxygen (O). The EDS analysis was conducted to determine the chemical composition of the catalyst, thereby confirming the successful integration of Ag and TiO_2 elements and validating the presence of the targeted species. This precise control over the Ag coating composition facilitates the optimization of photocatalyst properties.

The BET analysis findings indicate that the coating of Ag-TiO_2 onto the surface of AC led to a noticeable reduction in the surface area, volume, and pore size of AC this aligns with results reported in prior studies . The decrease in size can be ascribed to a variety of factors, such as the obstruction of surface area, the agglomeration of Ag-TiO_2 particles, consolidation during the coating procedure, and the chemical interactions between Ag-TiO_2 and AC. The catalyst surface area increases when the amount of Ag in the photocatalyst that is applied to AC is increased. On the other hand, there were no noticeable differences in the volume or pore size of the Ag-TiO_2 coated AC

UV-vis DRS analysis

The UV-vis DRS spectra obtained for AC/Ag-TiO_2 nanoparticles unveiled absorbing optical characteristics. The spectrum showed a broad absorption band in the visible region, which is indicative of the nanoparticles ability to absorb visible light. This absorption behavior holds immense significance for photocatalytic applications, as it suggests enhanced light-harvesting capabilities.

The obtained band gap energy of the AC/0.1%Ag-TiO_2, AC/0.5%Ag-TiO_2 and AC/1%Ag-TiO_2 catalyst were 1.74, 1.69 and 1.67 eV, respectively. The understanding of the optical properties, particularly the bandgap energy, of AC/0.1%Ag-TiO_2 holds great promise application for photocatalysis. In environmental remediation, these nanoparticles can be employed for the degradation of organic pollutants and the removal of contaminants from wastewater. The ability to harness ultraviolet and visible light ensures their versatility in different environmental conditions.

MNBs aeration

The size distribution of MNBs in the samples was evaluated using the Nano Tracking Analysis (NTA) method on a sophisticated nanoparticle size and concentration analyzer, namely the Malvern Panalytical NanoSight. The Stokes-Einstein equation, which computes particle size in terms of hydrodynamics, was then used to determine the size of these entities in the liquid phase. The physical analysis results of MNBs showed that the average bubble size was 125.90 ± 2.70 nm, and the most common size was 86.90 ± 2.00 nm. This implies that the aeration of MNBs with this apparatus produces air bubbles that are similar in size to MNBs. Due to the production of tiny, nanoscale air bubbles, the dissolved oxygen (DO) levels increased proportionately as the MNBs aerated. As a consequence, the desired DO range of 10.78–10.88 mgL^{-1} was reached in about 15 minutes. The reason why smaller MNBs are preferred is because of their longer lifetime in water and intrinsic stability, which raises DO levels. As a result, the addition of MNBs increased the oxidation-reduction potential (ORP), increasing noticeably from 249 mV in the cases when MNBs were not present to 275 mV in the cases where MNBs were present.

Dye degradation efficiency

Table 2 presents a comparison of IC and RB5 dye degradation efficiency at the 180-minutes mark for experimental conditions 1 and 2, both with an initial dye concentration of 10 µM. The photocatalytic degradation of IC dye under experimental condition 1 showed the following efficiencies: 87.03%, 93.66%, and 91.16% when using AC/Ag-TiO_2+UVA+MNBs as the catalyst. For RB5 dye, the corresponding efficiencies were 75.72%, 88.66%, and 86.69% with AC/0.5%Ag-TiO_2, AC/1.0%Ag-TiO_2, and AC/1.0%Ag-TiO_2 photocatalysts, respectively. While, in experimental condition 2, without MNBs, the photocatalytic degradation efficiencies for IC dye were 65.54%, 70.15%, and 68.20% with AC/0.5%Ag-TiO_2, AC/1.0%Ag-TiO_2, and AC/1.0%Ag-TiO_2 as catalysts, respectively. For RB5 dye in the same conditions, the photodegradation efficiencies were 62.11%, 66.90%, and 63.68% with AC/0.5%Ag-TiO_2, AC/1.0%Ag-TiO_2, and AC/1.0%Ag-TiO_2 catalysts, respectively.

Table 2 Dye degradation efficiency under various conditions given 180 min UVA irradiation time under initial dye concentrations of 10 µM.

Experimental condition	Description	Dye degradation efficiency (%) IC	RB5
1	AC/0.1%Ag-TiO_2+UVA+ MNBs	87.03	75.72
	AC/0.5%Ag-TiO_2+UVA+ MNBs	93.66	88.66
	AC/1.0%Ag-TiO_2+UVA+ MNBs	91.16	81.69
2	AC/0.1%Ag-TiO_2+UVA	65.54	62.11
	AC/0.5%Ag-TiO_2+UVA	70.15	66.90
	AC/1.0%Ag-TiO_2+UVA	68.20	63.68

Based on the comprehensive experiment results, it is evident that the photocatalyst prepared for the UVA-driven photocatalytic process demonstrated the capacity to degrade both IC and RB5 dyes, achieving degradation rates of approximately 65.54% to 70.15% for IC and 62.11% to 66.90% for RB5. Notably, the photocatalyst AC/0.5%Ag-TiO2 exhibited the highest degradation efficiency. This enhanced performance can be attributed to its physical properties, specifically the functional groups on AC that exhibit strong coordination with Ag, influencing the optimal band gap size for the photocatalytic process. The resulting photocatalyst boasts an increased number of active sites, a larger surface area, and heightened absorption capabilities. Moreover, the addition of MNBs to the photocatalytic reaction led to a noticeable improvement in efficiency. Both dyes underwent evident oxidation.

Further studies were carried out to investigate the kinetics and advancement of the reaction (Fig. 4). Specifically, the reaction rates observed during the photocatalyst cracking of IC and RB5 with and without MNBs were compared. The findings showed that there were differences in the reaction rates for both compounds when MNBs were present versus absent. It was clear from analyzing the first-order reaction constants that MNBs were essential in promoting the photocatalytic reactions for AC/0.1%Ag-TiO_2, AC/0.5%Ag-TiO_2, and AC/1.0%Ag-TiO_2. In particular, the rates of reaction were roughly 1.58, 2.79, and 1.75 times higher for IC and1.70, 1.99, and 1.10 times higher for RB5, respectively. MNBs, in summary, showed a noteworthy capacity to increase the effectiveness of photocatalytic processes in the degradation of IC and RB5. With AC/0.1%Ag-TiO_2, AC/0.5%Ag-TiO_2, and AC/1.0%Ag-TiO_2, the greatest photocatalytic rate constants for IC degradation in the absence of MNBs were 0.76×10^{-2}, 0.91×10^{-2}, and 0.79×10^{-2} min^{-1}, respectively. In a similar vein, the corresponding rate constants for RB5 degradation in the absence of MNBs were 0.61×10^{-2}, 0.90×10^{-2}, and 0.86×10^{-2} min^{-1}. When MNBs were added, the maximum photocatalytic rate constants for IC degradation increased to 1.20×10^{-2}, 2.54×10^{-2}, and 1.38×10^{-2} min^{-1}; for RB5 degradation, the rates increased to 1.04×10^{-2}, 1.79×10^{-2}, and 0.95×10^{-2} min^{-1} with AC/0.1%Ag-TiO_2, AC/0.5%Ag-TiO_2, and AC/1.0%Ag-TiO_2, among others. The results showed that by creating a heterojunction structural system between AC and Ag-TiO_2, adding Ag-TiO_2 to AC facilitated photocatalytic degradation. Therefore, compared to certain previously described photocatalysts, it can be concluded that the production of AC/Ag-TiO_2 leads in increased photocatalytic activity.

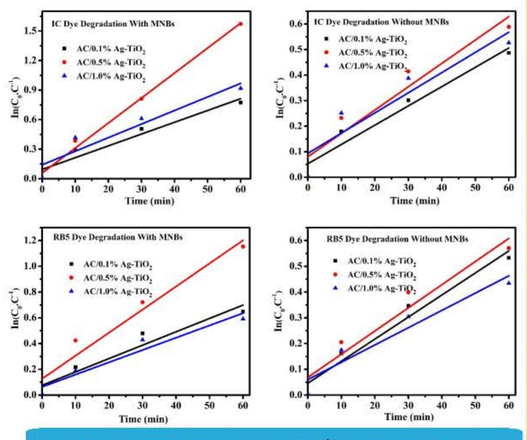

Fig. 4. Pseudo first-order kinetic plots of $\ln(C.C_0^{-1})$ relative to time for IC and RB5 dye degradation with various photocatalysts under with and without MNBs

Antibacterial activity

The agar well diffusion approach was used to investigate AC doped Ag 0.1, 0.5, and 1% antibacterial properties. The study utilized Gram (+ve) (S. aureus) and Gram (-ve) (E. coli) bacteria. Fig. 5 shows inhibited zones for E. coli and S. aureus against standard drugs and developed AC/Ag NPs at 50 and 100µg/mL the two doses. Synthesized NPs had a stronger antibacterial impact than traditional antibiotics (Fig.12). The zone of inhibition of AC/Ag NPs in E. coli was 10–16 mm, while conventional drugs were 16–20 mm. Zone inhibition enhanced with higher concentrations of silver nanoparticle-doped activated carbon. AC/Ag NPs (1.0%) at 100 µg/mL showed greater antibacterial properties against E. coli (15 mm) and S. aureus (12 mm) than 0.1%. Ag NPs bind to bacteria for three reasons. Initially microbes positively charged membrane proteins and negatively charged Ag NPs (stabilized carboxylate) may interact via electrostatic attraction. Second, physical alterations in the bacterial cell wall may lead to cellular material release and cell death. Third, Ag NPs permeate bacterial membranes. Ag NPs may impede bacterial DNA replication and respiration, damaging the cells (Sagar et al., 2023).

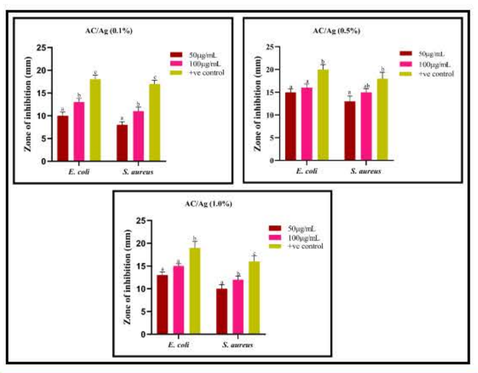

Fig. 5. Zone of inhibition of developed AC/0.1%Ag-TiO_2, AC/0.5%Ag-TiO_2, and AC/1.0%Ag-TiO_2 using well diffusion assay against *E. coli* and *S. aureus*.

Photocatalytic mechanisms

The effective treatment of pollutants can be greatly enhanced by the use of a hybrid photocatalyst, in which Ag-TiO_2 is coated over AC. Adsorption of contaminants can be carried out with great efficiency according to the intrinsic characteristics of AC precursors, which include critical surface area and porosity. By producing ROS and facilitating efficient charge separation, Ag-TiO_2 improves the photocatalyst's photocatalytic activity, which is supported by Ag nanoparticles. When these characteristics are combined, the adsorption and degradation processes of various pollutants are synchronized, producing a synergistic effect. Photoexcited carriers are quickly transferred to the particle surface through physical property manipulation such as band gaps, charge carrier separation, and plasmonic phenomena. A significant improvement in the total photocatalytic activity is achieved by this effective transfer mechanism, which significantly lowers carrier recombination rates.

4 CONCLUSION

The photocatalyst AC/0.5%Ag-TiO_2 clearly shows advantageous qualities for the removal of various pollutants when the experimental results are summarized. The coating of Ag-TiO_2 onto AC enhances the photocatalytic process by increasing the surface area, promoting efficient charge separation, generating ROS, creating a synergistic effect between adsorption and degradation, and introducing antibacterial properties. Within the photocatalytic process, the introduction of MNBs is found to operate as a catalyst for oxidation reactions, promoting the production of ROS including $\bullet O_2^-$, H_2O_2, and. Interestingly, increased DO concentrations enhance the production and quantity of ROS, such as $^1O_2$, H_2O_2, $\bullet OH$, and $\bullet O_2$. More DO during the photocatalytic degradation process is thought to be the cause of the enhanced presence of these free radicals. Moreover, the used AC/0.5%Ag-TiO_2 photocatalyst shows strong antibacterial activity against E. coli and S. aureus bacteria even in the absence of additional MNBs. This demonstrates the photocatalyst's intrinsic capacity to provide substantial value, generated from agricultural waste materials, expanding its applicability in a wide range of environmental pollutant treatment scenarios. Overall, the study results demonstrate the diverse range of applications and efficiency of agricultural waste-derived catalysts in tackling environmental issues.

5 ACKNOWLEDGMENTS

The authors wish to extend their heartfelt thanks to the Faculty of Engineering at Rajamangala University of Technology Thanyaburi (RMUTT) for their invaluable assistance. Furthermore, the authors appreciate the financial support received from the NSRF through the Program Management Unit for Human Resources & Institutional Development Research and Innovation [Grant No. B13F660068].

BRAINPOWER CONGRESS 2023

ร่วมกันสร้างและขับเคลื่อนงานวิจัยขึ้นแนวหน้า
สู่อุตสาหกรรมแห่งอนาคต

การประยุกต์ใช้คะตะลิสต์แบบแขวนลอยบำบัดสีย้อมด้วยกระบวนการโฟโตคะตะลิติกร่วมกับนาโนบับเบิ้ล

Micro-Nano Bubbles in Action: AC/TiO_2 Hybrid Photocatalysts for Efficient Organic Pollutant Degradation and Antibacterial Activity

Nicharee Akechatree, Orawan Rojviroon, Sumonman Naimlang, Thammasak Rojviroon, Ranjith Ranjendran, Yuwadee Leelert, Sutthida Wongwichian, Sanya Sirivithayapakorn, SDG LINK company limited

Introduction

The discharge of improperly treated dye wastewater into watercourses causes ecological imbalance by affecting sunlight penetration, reducing dissolved oxygen, causing eutrophication, and harming aquatic life. As a result, several treatment techniques have been proposed to treat dye wastewater. However, the existing treatment techniques are somewhat inefficient and/or costly. The photocatalytic degradation of dyes utilising semiconductor materials is one of the efficient processes for rapid and low-cost treatment.

In dye wastewater treatment, hybrid photocatalysts, such as activated carbon coated with TiO_2, have been increasingly adopted to enhance the photocatalytic process. The augmentation of the photocatalytic process with micro-nano bubbles (MNB) aeration potentially enhances the photocatalytic degradation of dyes in wastewater. The fine bubbles provide a large interfacial area for efficient contact between dye molecules and the photocatalyst.

Specifically, this research comparatively investigates the photocatalytic degradation efficiency of synthetic dyes in wastewater using a hybrid photocatalyst (HP) with and without MNB aeration under UVA irradiation (i.e., HP+UVA+MNB and HP+UVA). The hybrid photocatalyst was AC coated with TiO_2.

Methods

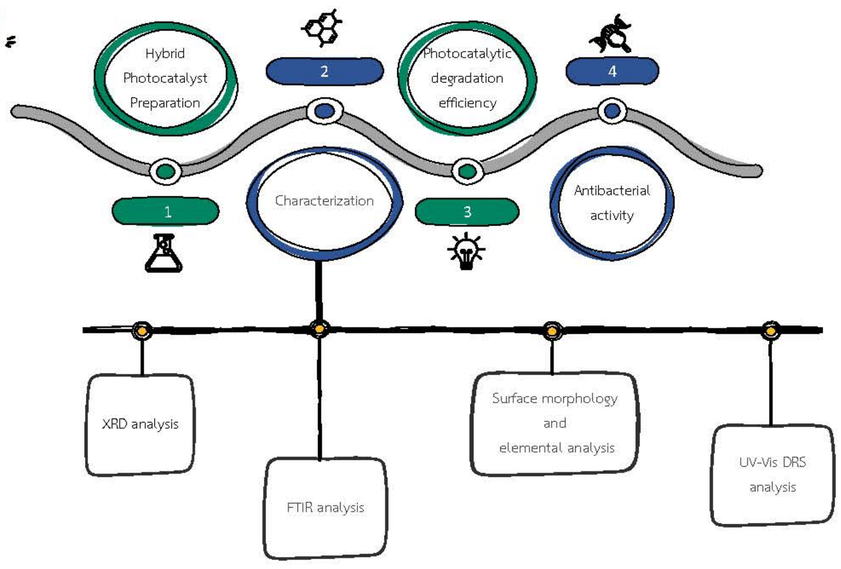

Results and discussion

1 XRD analysis

The crystal structure and phase composition of the as-prepared AC and HP photocatalyst. the results were shown in Fig. 1. Two broad peaks can be seen in the XRD pattern of the AC photocatalyst at 24.8° and 43.6°, which correspond to reflections in the (002) plane and (100) plane, respectively. These confirm the presence of the quartz phase at two-dimensional thoughts of disordered stacking of micrographites. Furthermore, The XRD peaks of the HP photocatalyst were slightly shifted to a lower angle side and reduced the intensity by adding TiO_2 nanoparticles. The shift is reasonable because the TiO_2 was incorporated into the AC lattice, but the TiO_2 peak has not appeared because the TiO_2 concentration is very low compared to AC.

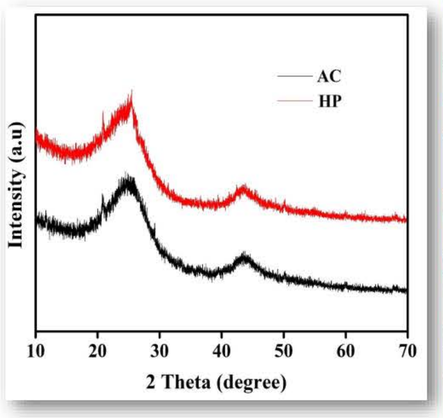

Fig. 1. XRD spectra of the as-prepared photocatalyst.

2 FTIR analysis

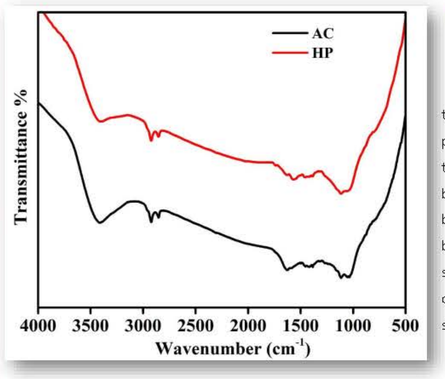

Fig. 2. FTIR spectra of AC and HP Photocatalysts

FTIR spectra examined the effect of activated carbon on the surface functional groups, and the results are shown in Fig. 2. The band at 3,423 cm^{-1} could be due to the –OH stretching of polymeric compounds or the presence of N-H groups. The peaks at 2,928 and 2,855 cm^{-1} indicate the C–H stretching vibrations, and the peak at 1,428 cm^{-1} indicates C=C groups in carbon. The band at 1,626 cm^{-1} corresponds to the carbonyl stretching vibration of amide, which is thought to be caused by the combined action of double-bond stretching vibration and -NH deformation band for lead-loaded activated carbon. Additionally, the minor peaks at 1,115 and 1,032 cm^{-1} suggest the S=O. The C=O and S=O functional groups have been reported to show very high coordination with trace metals. Also, in this case of AC-coated TiO_2 nanoparticles, the band shifted to a higher wavenumber, indicating the presence of AC in TiO_2 nanoparticles.

3 Surface morphology and elemental analysis

The surface morphology and particle size of the AC and the HP photocatalyst are characterized through the SEM and HR-TEM analysis. Fig. 3(a) and (b) illustrate the surface morphology and elemental composition of the uncoated AC and the HP photocatalyst, respectively. The AC surface with large agglomerates and inhomogeneous were observed. In Fig. 3(b) clearly shows that the TiO_2 nanoparticles were efficiently coated on the AC surface. Fig. 3. shows the EDS image of the HP photocatalyst demonstrating the strong peaks of Ti, with 0.74 wt% of Ti coated on the AC surface (Table 1). The other elements present on the AC surface were carbon (C), silicon (Si), and oxygen (O). The HP photocatalyst morphology was further revealed by High-resolution transmission electron microscopy (HRTEM); the results are shown in Fig. 4a-d. The images clearly show they had a quasi-spherical shape-like morphology with an average size of 8-15 nm.

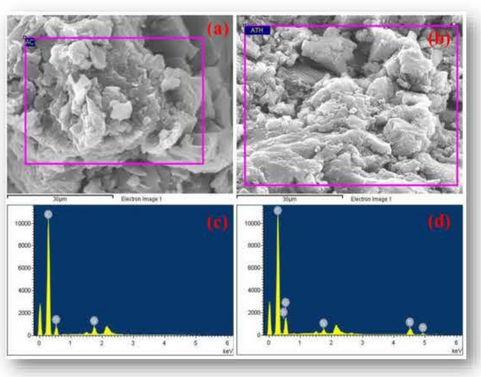

Fig. 3. SEM images and EDS elemental composition of: (a) uncoated AC, (b) HP photocatalyst.

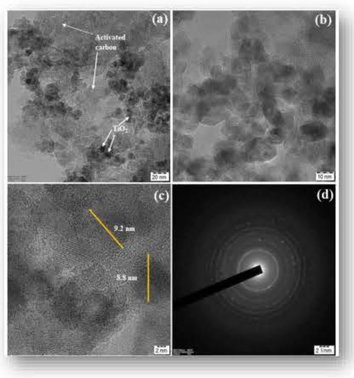

Fig. 4. TEM images of HP photocatalyst.

The BET surface area, pore volume, and pore 227 size of the HP photocatalyst slightly decreased. Due to the blockage of surface area, agglomeration of TiO_2 particles, sintering during the coating process, and chemical reaction between TiO_2 and AC. Despite the smaller specific surface area, pore size, and volume of the HP photocatalyst, they are insignificantly different from the uncoated AC (Table 1).

Table 1 Elemental composition and BET surface property of uncoated AC and HP photocatalyst.

Experiment condition	Composition (%)				Surface property		
	Ti	C	Si	O	Surface area ($m^2.g^{-1}$)	Pore volume ($mL.g^{-1}$)	Pore size (Å)
Uncoated AC	-	27.26	0.40	72.54	1.981×10^2	0.183	6.235×10^1
HP	0.74	26.83	0.21	72.21	1.603×10^2	0.170	4.253×10^1

Regarding the data concerning the particle size, size distribution, and MNB concentration in experimental condition 1 (HP+UVA+MNB), MNB was produced using the RMUTT-MNB generator, operating at a flow rate of 20 to 80 $L.min^{-1}$ and a pressure range of 220 to 230 kPa. The particle sizes of MNB varied between 86.9 and 258.2 nm, with the most prevalent bubble size measuring 103.5±4.8 nm, accompanied by dissolved oxygen (DO) concentrations ranging from 10.78 to 10.88 $mg.L^{-1}$.

4 UV-Vis DRS analysis

The optical absorption properties of the as-prepared AC and the HP photocatalyst were analyzed by the UV-Visible Diffuse Reflectance Spectrometer (UV- DRS). In Fig.5a, both AC and the HP photocatalyst have shown a broad visible absorption edge, which indicates the catalyst's good absorption property. their results are shown in Fig.5b. The obtained band gap energy of the AC and the HP catalyst are 1.63 and 1.72 eV, respectively. While adding the TiO_2 nanoparticle on AC, the bandgap energy was shifted to a higher angle side.

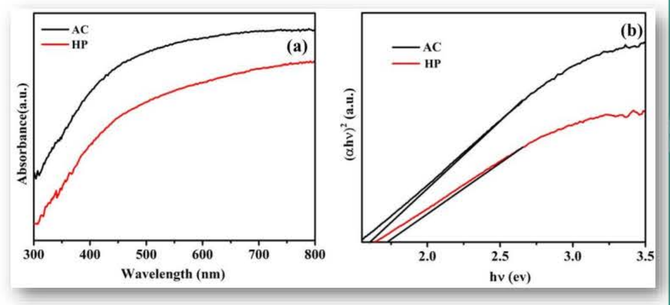

Fig. 5. (a) UV-Vis Diffuse reflectance spectra and (b) Tauc plots of AC and HP nanoparticles.

5 Photocatalytic degradation efficiency

Fig. 6. The IC, MB, and RB5 dye degradation efficiency of experimental conditions 1 (HP+UVA+MNB) achieved the highest dye degradation efficiency of 69.09%, 60.06%, and 55.19% for IC, MB, and RB5, respectively. The dye degradation efficiency was lower under the experimental condition 2 (HP+UVA) due to the absence of MNB (50.22%, 44.19%, and 37.88% for IC, MB, and RB5). The HP photocatalyst provided larger surface area for the photocatalytic reaction. However, in the absence of MNB, the photocatalytic reaction proceeded at a slower rate.

The experimental condition 3 (HP+MNB) was ineffective for treatment of dye wastewater due to the lack of UVA irradiation. The experimental conditions 4 (AC+UVA+MNB), 5 (AC+MNB), 6 (AC+UVA) and 7 (AC) exhibited only adsorption and absorption on the uncoated-AC Meanwhile, the experimental condition 8 (MNB) showed that the sole use of MNB aeration achieved poor dye degradation performance.

The comparison, the structure of RB5 was highly complex, followed by MB and IC. As a result, MB and IC were readily degradable by the photocatalytic process due to their simpler structures that are more susceptible to reactive oxygen species (ROS) attack. Meanwhile, RB5 has a more complex structure that demands greater energy for degradation. Besides, due to the presence of a sulfonate group (SO_3^-), RB5 is negatively charged, thus hindering the adsorption of dye onto the photocatalyst surface.

The MNB aeration levels of experimental condition 1 (HP+UVA+MNB) is positively correlated with the DO levels and oxidation-reduction potential (ORP) of the photocatalytic process. In other words, higher DO levels result in higher ORP, which in turn promotes the generation of electron-hole pairs. Higher ORP also promotes the formation of ROS, which enhances the photocatalytic degradation of dye molecules and organic pollutants. As a result, ORP can be used to assess the dye degradation efficiency of the photocatalytic process.

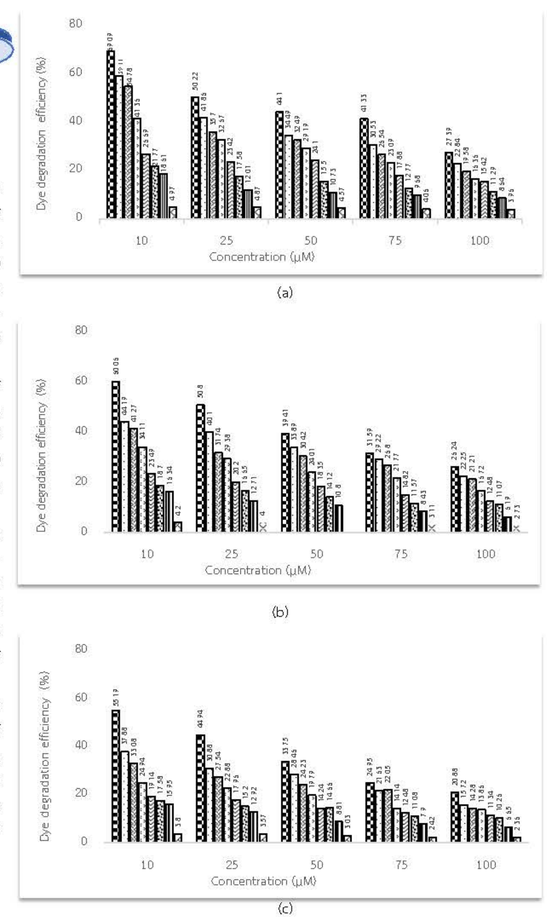

Fig. 6. Dye degradation efficiency of the experimental conditions being studied at termination (at 180 minutes) under variable initial dye concentrations: (a) IC, (b) MB, (c) RB5.

Antibacterial activity

The present study manufactured AC and HPNPs found a larger bacteria inhibition zone than the standard antibiotic. The highest antibacterial activity was observed at 100 $\mu g.mL^{-1}$ against Gram-positive S. aureus and Gram-negative E. coli. The HP showed a higher zone of inhibition (ZOI) for E. coli (19.50 ± 0.5 mm) and S. aureus (14.5 ± 0.2 mm) clearance after 24 hours of incubation. Negative control (10% DMSO) showed no ZOI (Fig.7 & Fig.8). TiO_2 nanoparticles interact with sulfur-containing proteins in the bacterial surface and phosphorus-containing molecules like DNA. Titanium has a stronger binding affinity for sulphur and phosphorus-containing cell biomolecules. Sulphur-containing proteins in cell membranes, within cells, and phosphorus-containing components like DNA will be the preferred locations for HP nanoparticle binding. When TiO_2 nanoparticles penetrate a bacterial cell, they produce a low molecular weight zone that protects DNA from titanium ions. The nanoparticles target the respiratory chain, causing cell division and death. In bacterial cells, nanomaterials release ions that boost bactericidal action.

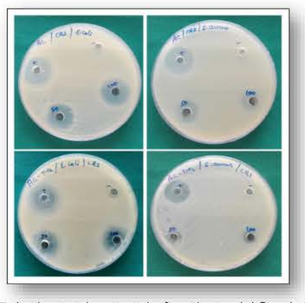

Fig. 7. Antibacterial potential of synthesized AC and HP on Gram- positive S. aureus and Gram-negative E. coli bacteria.

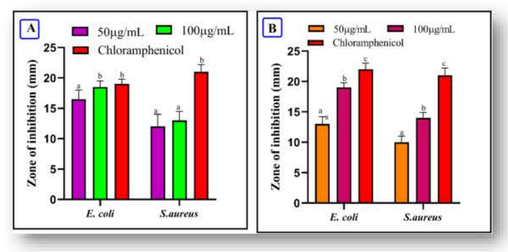

Fig. 8. Zone of inhibition for synthesized A). Activated carbon and B). Activated carbon

Conclusion

This research comparatively investigated the photocatalytic degradation efficiency of synthetic dyes in dye wastewater using hybrid photocatalyst (HP) with and without MNB aeration under UVA irradiation (i.e., HP+UVA+MNB and HP+UVA). The experimental synthetic dyes were IC, MB, and RB5, and the initial dye concentrations were varied between 10, 25, 50, 75 and 100 μM. The hybrid photocatalyst was TiO_2-coated AC. The experimental results showed that HP+UVA+MNB enhanced the degradation efficiency of the dyes, achieving the highest degradation efficiency of 69.09%, 60.06%, and 55.19% for IC, MB, and RB5, respectively, given 180 minutes of UVA irradiation and 10 μM initial dye concentration. Specifically, the HP photocatalyst augmented with MNB aeration enhanced the adsorption mechanism and the photocatalytic activity. Essentially, HP+UVA+MNB enhanced the photocatalytic degradation activity of synthetic dyes, rendering the technology operationally and environmentally suitable for dye wastewater treatment. The produced AC and HP also demonstrated an improved ZOI towards both bacterial strains.

Acknowledgments

The authors would like to express their sincere gratitude to the Faculty of Engineering at Rajamangala University of Technology Thanyaburi (RMUTT) for their valuable support. Additionally, the authors are thankful for the financial assistance provided by the NSRF via the Program Management Unit for Human Resources & Institutional Development Research and Innovation [Grant No. B13F660068].

BRAINPOWER CONGRESS 2023

ร่วมกันสร้างและขับเคลื่อนงานวิจัยขึ้นแนวหน้า
สู่อุตสาหกรรมแห่งอนาคต

Performance of thermal reflection paint from the nanocellulose material with natural bamboo for energy savings

Prasan Chaisaenrith[1], kriengsak Pojthanaditee[2], Sakchai Pojthanaditee[2], Sorapong Pavasupree[1*]

[1]Department of Materials and Metallurgical Engineering, Faculty of Engineering, Rajamangala University of Technology Thanyaburi, Pathumthani, 12110, Thailand

[2]Toppaint Perfect Company Limited, Bong Bon sub district, Nong Sua district, Pathumthani, 10170, Thailand

*Email: sorapong.p@en.rmutt.ac.th

I. INTRODUCTION

Saving energy and Environment

Global warming

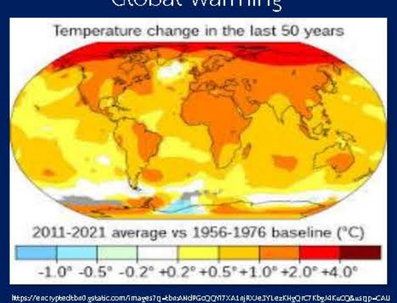

1.5 ° C

Climate change

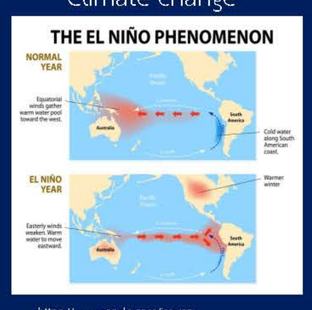

https://www.google.com/imgres

Create or develop materials technology

Natural bamboo

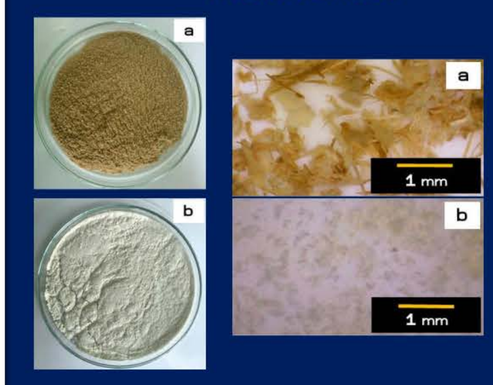

Fig. 1 natural bamboo (a) and (b) natural bamboo after synthesis and griding with ball mill 2 hrs.

Paint reflectance Technology

IP : หมายเลขคำขอ 2303000171

II. METHODOLOGY

Hydrolysis process

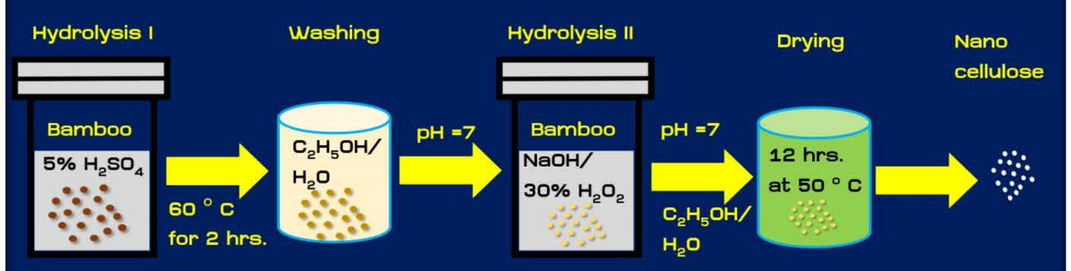

Fig.2 Schematic representation of the preparation of nanomaterials with the hydrolysis technique from natural bamboo for 60 ° C at 2 hrs.

Thermal reflection paint

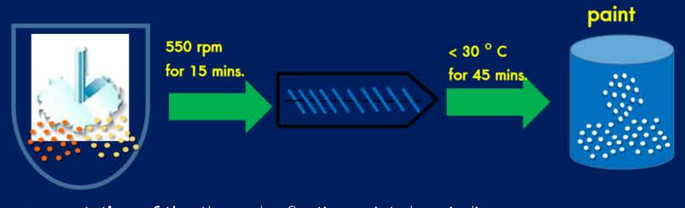

Fig.3 Schematic representation of the thermal reflection paints by grinding process.

Thermal performance

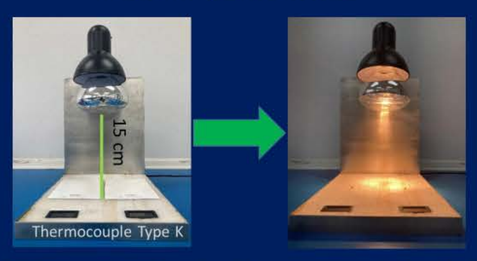

Fig.4 Schematic representation of the apparatus developed for exposure to IR radiation (ASTM E 903) .

III. RESULT AND DISCUSSION

Characterization

XRD

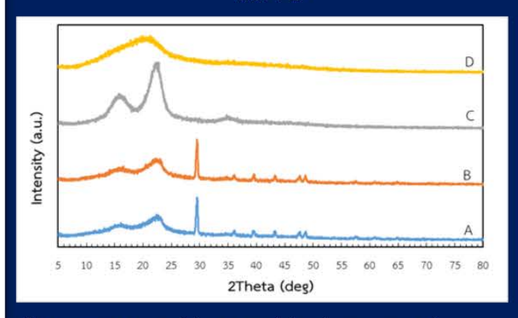

Fig.5 XRD pattern of the natural bamboo prepare by hydrolysis process for 60 ° C at 2 hrs.

SEM

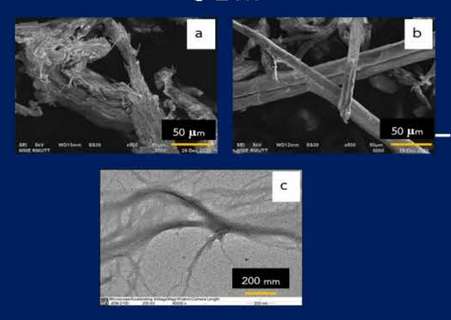

Figs.6 SEM image of the natural bamboo after grinding (a, b) and (c) nano cellulose prepare by hydrolysis process and after grinding by TEM.

Application properties

Table 1 Physical properties of thermal reflection paints.

Type	Density (g/cm^2) ASTM D1963	Viscosity (K.U) ASTM D562	Non volatile (%) ASTM D2832	Hiding power (%) ASTM D344
Titanium dioxide	1.174	78.0	46.8	91.0
Nano P-25	1.144	88.0	45.0	87.0
Nano Cellulose	1.140	83.0	45.0	88.0
Commercial in market	1.214	94.0	46.7	97.4

Table 2 The CIELab value of thermal reflection paints (ASTM D 2244).

Type	Color coordinate D65, 10 °		
	L	a*	b*
Titanium dioxide	96.78	-0.69	1.24
Nano P-25	96.48	-0.63	2.38
Nano Cellulose	96.85	-0.68	1.31
Commercial in market	97.76	-0.72	0.72

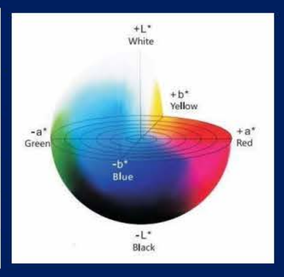

Thermal performance properties

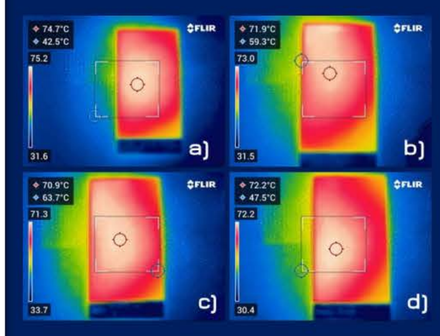

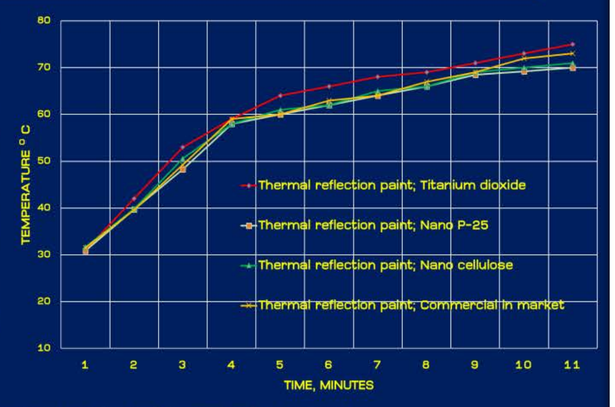

Figs. 7 Temperature back side surface of thermal reflection paints.

Field Test in next time

IV. CONCLUSION

- The natural bamboo can synthesize nanoparticles through the hydrolysis process.
- Thermal reflection paint using nanocellulose contains a small particle size, which also acts as a barrier and can reduce the surface temperature of the tin plate.
- Passively decreasing the building's heating load consumption was achieved by a possible roof and wall improvement using nanocellulose in thermal reflection paint.

ACKNOWLEDMENTS :

- This research has received funding support from the NSRF via the Program Management Unit for Human Resources & Institutional Development, Research and Innovation [grant number B13F660068]
- Rajamangala University of Technology Thanyaburi, Thailand
- Toppaint Perfect Company Limited, Thailand

BRAINPOWER CONGRESS 2023

ร่วมกันสร้างและขับเคลื่อนงานวิจัยขั้นแนวหน้า
สู่อุตสาหกรรมแห่งอนาคต

การวิเคราะห์ผลกระทบทางความร้อนของสายไฟฟ้าแรงสูงใต้ดินในท่อร้อยสายแบบต่าง ๆ

นายฤทธิชัย ราชแป้น รองศาสตราจารย์ ดร.บุญยัง ปลั่งกลาง และนายยุทธพงษ์ ศรีวิชัยมูล
ภาควิชาวิศวกรรมไฟฟ้า คณะวิศวกรรมศาสตร์ มหาวิทยาลัยเทคโนโลยีราชมงคลธัญบุรี
บริษัท ไททัม จำกัด 63/10 ม.4 ต.บึงคำพร้อย อ.ลำลูกกา จ.ปทุมธานี 12150

ความสำคัญของปัญหา

1. พื้นที่สำหรับก่อสร้างสาธารณูปโภคดินมีพื้นที่จำกัด
2. การก่อสร้างมีผลกระทบต่อผู้ใช้ทางสาธารณะ
3. ลดงานก่อสร้างโดยเพิ่มประสิทธิภาพของสายไฟฟ้า

ภาพที่ 1 ภาพผลกระทบจากงานก่อสร้าง

วิธีการดำเนินงาน

1. ศึกษาและออกแบบพร้อมเสนอแบบก่อสร้างท่อร้อยสายแบบใหม่
2. จำลองความร้อนเพื่อศึกษาผลกระทบต่อกระแสของสายไฟฟ้าใต้ดินในท่อร้อยสายแบบต่าง ๆ ในสภาวะไม่มีน้ำท่วมสายไฟฟ้า ด้วยวิธีไฟไนต์เอลิเมนต์
3. จำลองความร้อนเพื่อศึกษาผลกระทบต่อกระแสของสายไฟฟ้าใต้ดินในท่อร้อยสายแบบต่าง ๆ ในสภาวะที่มีน้ำท่วมสายไฟฟ้า ด้วยวิธีไฟไนต์เอลิเมนต์
4. เปรียบเทียบและวิเคราะห์ผลการจำลองของการติดตั้งสายไฟฟ้าใต้ดินแต่ละรูปแบบของท่อร้อยสายแบบต่าง ๆ
5. เปรียบเทียบต้นทุนการก่อสร้างระบบไฟฟ้าใต้ดินในท่อร้อยสายแบบต่าง ๆ
6. เปรียบเทียบระยะเวลาก่อสร้าง ช่วงตั้งแต่เริ่มเปิดผิวจราจรจนถึงขั้นตอนคืนผิวจราจรถาวร ของท่อร้อยสายแบบต่าง ๆ

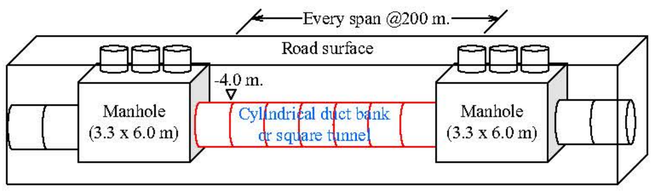

ภาพที่ 2 รูปแบบท่อร้อยสายไฟฟ้าใต้ดิน

จากภาพที่ 2 เป็นรูปแบบท่อร้อยสายไฟฟ้าใต้ดิน ที่ก่อสร้างด้วยวิธี Pipe Jacking ซึ่งงานวิจัยนี้พิจารณาท่อร้อยสายแบบ Cylindrical duct bank ซึ่งเป็นรูปแบบดั้งเดิม และนำเสนอแบบ Square tunnel ซึ่งเป็นรูปแบบใหม่ มีรายละเอียดดังภาพที่ 3 และภาพที่ 4

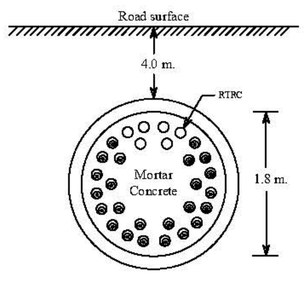

ภาพที่ 3 Cylindrical duct bank (ใช้งานในปัจจุบัน)

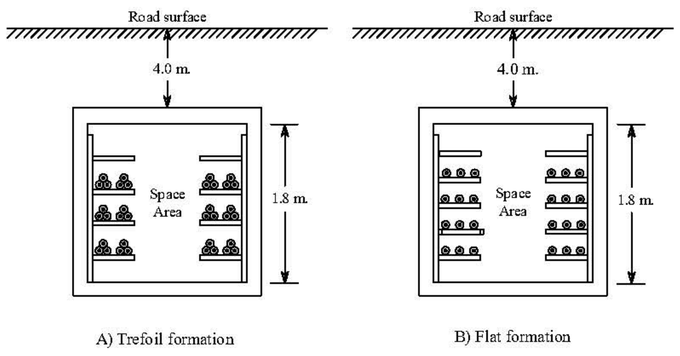

ภาพที่ 4 Square tunnel (รูปแบบที่นำเสนอ)

ผลการวิจัย

จากการศึกษาและออกแบบพร้อมนำเสนอแบบก่อสร้างท่อร้อยสาย นำไปสู่การจำลองความร้อนเพื่อศึกษาผลกระทบต่อกระแสของสายไฟฟ้าใต้ดินที่ติดตั้งในท่อร้อยสายแบบต่าง ๆ ด้วยวิธีไฟไนต์เอลิเมนต์ ซึ่งได้ผลการวิจัยดังนี้

1.กระแสของสายไฟฟ้าที่ได้จากการจำลองความร้อนด้วยไฟไนต์เอลิเมนต์ของสายไฟฟ้าใต้ดินที่ติดตั้งในท่อร้อยสายแบบต่าง ๆ ในสภาวะไม่มีน้ำท่วมสายไฟฟ้า นำเสนอได้ดังนี้

ตารางที่ 1 กระแสของสายไฟฟ้า ในสภาวะไม่มีน้ำท่วมสายไฟฟ้า

Number of conductors	Ampacity (A)		
	Cylindrical duct bank	Square tunnel	
	Trefoil	Flat	Trefoil
6	829	748	725
12	669	652	637
18	570	532	520
24	509	494	483
30	-	-	426
36	-	-	405

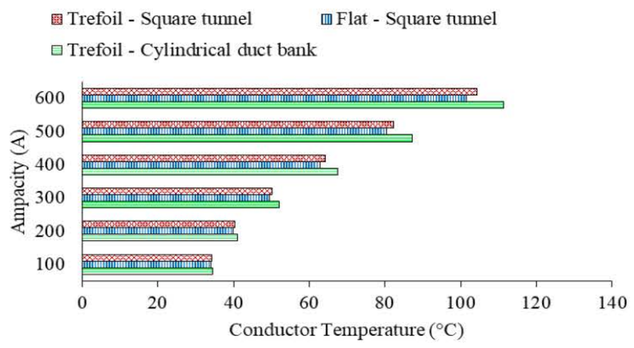

ภาพที่ 5 อุณหภูมิตัวนำที่ขนาดกระแสต่าง ๆ ในสภาวะไม่มีน้ำท่วม

2. กระแสของสายไฟฟ้าที่ได้จากการจำลองความร้อนด้วยไฟไนต์เอลิเมนต์ของสายไฟฟ้าใต้ดินที่ติดตั้งในท่อร้อยสายแบบต่าง ๆ ในสภาวะที่มีน้ำท่วมสายไฟฟ้า นำเสนอได้ดังนี้

ตารางที่ 2 กระแสของสายไฟฟ้า ในสภาวะที่มีน้ำท่วมสายไฟฟ้า

Number of conductor	Ampacity (A)		
	Cylindrical duct bank	Square tunnel	
	Trefoil	Flat	Trefoil
6	912	1,112	1,108
12	697	811	810
18	590	668	600
24	523	579	577
30	-	-	478
36	-	-	445

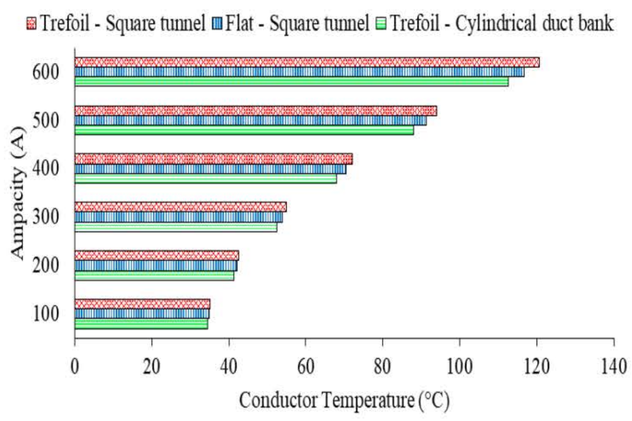

ภาพที่ 6 อุณหภูมิตัวนำที่ขนาดกระแสต่าง ๆ ในสภาวะที่มีน้ำท่วม

3. ต้นทุนค่าก่อสร้างระบบไฟฟ้าใต้ดินของสายไฟฟ้าที่ติดตั้งในท่อร้อยสายแบบ Cylindrical duct bank และแบบ Square tunnel ซึ่งก่อสร้างท่อร้อยสายโดยวิธี Pipe Jacking ที่ระดับลึกจากผิวจราจรถึงหลังท่อร้อยสาย ระยะ 4.00 เมตร ซึ่งการคำนวณต้นทุนระบบไฟฟ้าใต้ดิน คิดเฉพาะต้นทุนทางตรงที่ระยะทาง 1,000 เมตร ซึ่งสามารถแสดงได้ดังตารางที่ 3

ตารางที่ 3 เปรียบเทียบต้นทุนค่าก่อสร้างระบบไฟฟ้าใต้ดิน

Description	Cost (Baht)	
	Cylindrical duct bank	Square tunnel
Design	175,000	175,000
Topographic survey	100,000	100,000
Traffic management	350,000	350,000
Manhole work	18,764,000	18,764,000
Pipe jacking work	35,260,000	40,640,000
Inner duct (RTRC)	11,720,000	-
Grouting work	9,590,000	-
Cable racks	-	3,960,000
Cable cleats	-	16,400,400
Pavement	791,000	791,000
Summary cost	76,750,000	81,180,000
Cost per circuit	19,187,500	13,530,000

4. ระยะเวลาก่อสร้าง ช่วงที่ทำการก่อสร้างท่อร้อยสายไฟฟ้า เริ่มตั้งแต่สกัดเปิดผิวจราจรจนกระทั่งคืนผิวจราจรถาวรแล้วเสร็จ คิดเฉพาะงานก่อสร้างด้านโยธาที่ส่งผลกระทบต่อการจราจรและส่งผลกระทบต่อผู้ใช้เส้นทาง พบว่าการก่อสร้างท่อร้อยสายแบบ Square tunnel สามารถคืนผิวจราจรถาวรได้เร็วกว่าแบบ Cylindrical duct bank ซึ่งนำเสนอได้ดังตารางที่ 4

ตารางที่ 4 เปรียบเทียบระยะเวลาก่อสร้างด้านโยธา

Description	Construction Period (Day)					
	MH.1	MH.2	MH.3	MH.4	MH.5	Sum
Cylindrical duct bank	85	85	85	85	85	425
Square tunnel	65	65	65	65	65	325

สรุปผลการวิจัย

การวิเคราะห์ผลกระทบทางความร้อนของสายไฟฟ้าแรงสูงใต้ดินในท่อร้อยสายแบบต่าง ๆ สามารถสรุปผลการวิจัยได้ดังนี้

1. ในสภาวะที่ไม่มีน้ำท่วมสายไฟฟ้า สายไฟฟ้าที่ติดตั้งใน Cylindrical duct bank จะรับภาระกระแสได้สูงที่สุด ในขณะที่การจัดเรียงสายแบบ Trefoil ใน Square tunnel จะรับภาระกระแสได้ต่ำที่สุด
2. ในสภาวะที่มีน้ำท่วมสายไฟฟ้า สายไฟฟ้าที่ติดตั้งใน Cylindrical duct bank จะรับภาระกระแสได้ต่ำที่สุด ในขณะที่การจัดเรียงสายแบบ Flat ใน Square tunnel จะรับภาระกระแสได้สูงที่สุด
3. การไฟฟ้านครหลวง ใช้สายส่งไฟฟ้า ขนาด 800 ตร.มม. จำนวน 6 เส้นต่อวงจร ซึ่ง Cylindrical duct bank สามารถรองรับได้จำนวน 4 วงจร ในขณะที่ Square tunnel จัดเรียงสายแบบ Flat ได้จำนวน 4 วงจร และจัดเรียงสายแบบ Trefoil ได้จำนวน 6 วงจร
4. ต้นทุนค่าก่อสร้างระบบไฟฟ้าใต้ดิน ด้วยวิธี Pipe Jaking โดยใช้แบบ Square tunnel จะมีต้นทุนค่าก่อสร้างสูงกว่าแบบ Cylindrical duct bank 5.77% ในทางกลับกันหากเปรียบเทียบต้นทุนต่อวงจร จะพบว่าแบบ Square tunnel มีต้นทุนต่อวงจรถูกกว่า 29.49%
5.ระยะเวลาก่อสร้างของท่อร้อยสาย แบบ Square tunnel สามารถคืนผิวจราจรถาวรได้เร็วขึ้น 23.53%

กิตติกรรมประกาศ

งานวิจัยนี้ได้รับเงินทุนสนับสนุนจาก NSRF ผ่านทางหน่วยบริหารและจัดการทุนด้านการพัฒนากำลังคนและทุนด้านการพัฒนาสถาบันอุดมศึกษา การวิจัยและการสร้างนวัตกรรม (บพค.) [หมายเลขทุน BIBF660068]

BRAINPOWER CONGRESS 2023

ร่วมกันสร้างและขับเคลื่อนงานวิจัยขั้นแนวหน้า
สู่อุตสาหกรรมแห่งอนาคต

Performance Analysis and Econometric Assessment of A Community Waste Power Plant Biogas System

Oluwaseun Olanrewaju Akinte and Boonyang Plangklang

Department of Electrical Engineering, Faculty of Engineering, Rajamangala University of Technology Thanyaburi (RMUTT), Pathum Thani, 12110 Thailand.

Rationale

1. To perform a techno-economic analysis and assessment of the first community waste power plant (biogas) system in Thailand.
2. The potential Capability of the biogas plant to operate as a sustainable, safe and clean alternative energy system within the human community (Onnut).
3. To determine the most efficient and effective energy cost operation between the grid-biomass network and grid-biomass-storage network configurations.
4. To utilize food scraps (highest solid wastes composition) within the community in generating electricity to support the grid system.

Problem statement

1. Energy demand variation.
2. Biomass energy fraction and penetration on grid system.
3. Techno-economical reliability of the integrated grid-biogas-storage network system.
4. Flexibility issue and storage control against capacity shortage.
5. Wastes to Energy Conversion and utilization.

Introduction

The impact of hybrid energy sources (biomass energy, nuclear power plant, thermal power plant, solar power, wind power plant, and hydroelectricity) from energy production (generation), energy regulation (transmission stations and distribution stations), energy control measure (control center system) and energy conversion process (energy storage system: batteries, capacitors, ultracapacitors, and flywheel) makes power system network flexible enough to accommodate excessive energy demand (power consumers: smart cities and smart houses) and provide support towards the utility grid system in overcoming congestions, capacity shortage from energy sources and unmet load, respectively. Hence, the need for ancillary services from renewable energy systems integration with the grid network to reduce toxic emission into the society, maintain safe and clean energy production and providing a standby generator (backup stable secondary energy source: biomass generator, hydropower, and hybrid storage system) against power fluctuation from the main (primary) energy sources is essential to maintain a continuous energy flow network.

This present research adopted a community waste power plant biogas system in Thailand that will maintain a sustainable, safe, and alternative clean energy system for the human environment when it is integrated with the utility grid system and hybrid storage system, respectively. A standby operation (secondary energy source) from the biomass generator will maintain a backup power plan with the storage system (Lithium-ion, Li-NEC and Zinc bromide batteries) against the unreliable grid network when unexpected outage, grid schedule and congestion occur from the grid network.

Methodology

1.The potential resources (biomass) for the case study area (Onnut) will be obtained from data record of Onnut community.

2. Mathematical modelling of the energy system components (Grid system, biomass generator, batteries and power converter).

3.Experimental model (grid-forming and grid following) of the biogas-grid system network of Onnut community and simulation model application of HOMER PRO Microgrid analysis for the hybrid network.

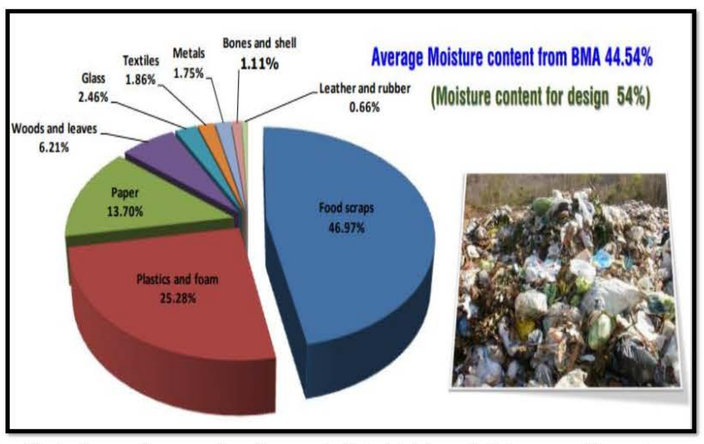

Fig1: Onnut Community: Research Sub-Division, Solid waste, Hazardous waste and Night soil Management Division, Department of Environment, BMA (Bangkok Metropolitan Area).

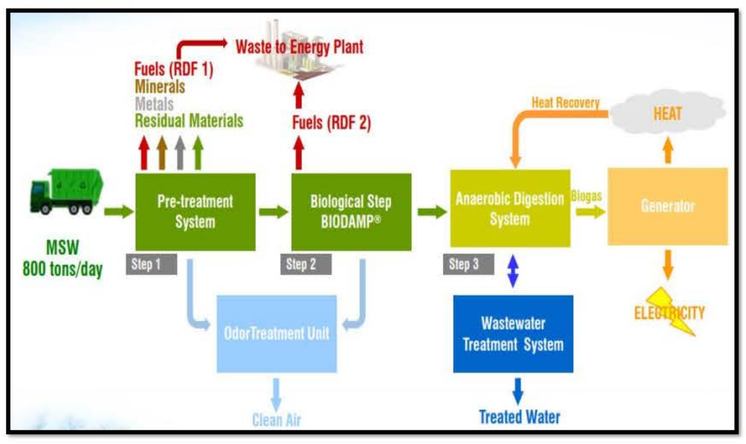

Fig 2: Current Waste to Energy Conversion Technology from Onnut Community

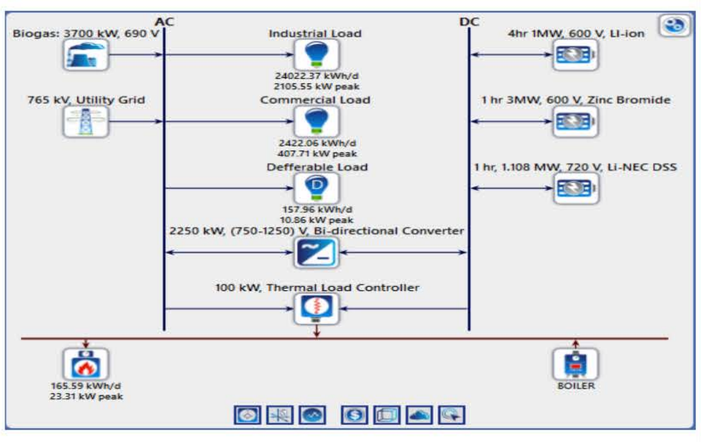

Fig 3: Proposed Waste to Energy Conversion Technology Design for Onnut Community

Result and Discussion

The econometric assessment and performance analysis of the first community waste power plant biogas system integration with the utility grid and hybrid storage system (Li-ion, Li-NEC, and ZnBr batteries) in Thailand was carried out through a novel investigation of a dynamic multi-task control system (cycle charging and load following control systems) that interfaced over the biomass gasifier-utility grid energy system, off-grid biomass gasifier-storage energy system and biomass gasifier-utility grid-storage energy system operational modes effectively to serve the load fully. The utility grid-biomass gasifier generator-storage energy system configuration adopted cycle charging and load following control systems with a thermal load controller (to limit the amount of current the load can draw from the energy sources) while the off-grid biomass gasifier generator-storage energy system configuration adopted cycle charging and thermal load controller strategy to determine the best reliable, efficient, and cost minimization system.

The off-grid energy system recorded ZnBr battery as producing the highest output energy (5,335,103 kWh/yr) over Li-ion battery (3,125,919 kWh/yr), thereby, consuming more energy (5,927,893 kWh/yr) than Li-ion energy (3,468,114 kWh/yr) system. The grid connected mode of the integrated biogas-storage network indicated that Li-ion battery consumed (288,925 kWh/yr) and gave out (263,173 kWh/yr) more energy than the ZnBr input (72,231 kWh/yr) and output (65,767 kWh/yr) energies. The Li-NEC battery maintained its maximum state of charge (100 %) with no inflow and outflow of energy.

Performing the econometric analysis of the entire system, the integrated grid-biogas-storage system estimated the Li-NEC network configuration as the most economically efficient system with the highest internal rate of return, IRR: 899 %, return on investment, ROI: 856 %, payback period: 0.11 year over the Li-ion network configuration with IRR: 620 %, ROI: 588 %, payback period:0.16 year and ZnBr network system with IRR: 518 %, ROI: 489 % with payback period: 0.19 year. The off-grid network shows that the ZnBr network configuration as the only economically feasible network system with IRR: 20 %, ROI: 23 % and payback period of 3.7 years while Li-ion and Li-NEC network systems are not economically feasible.

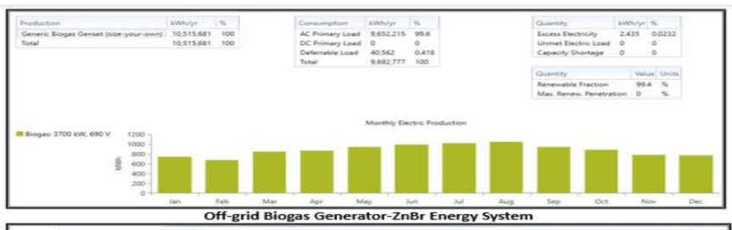

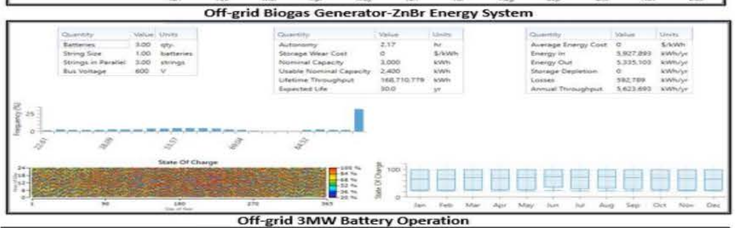

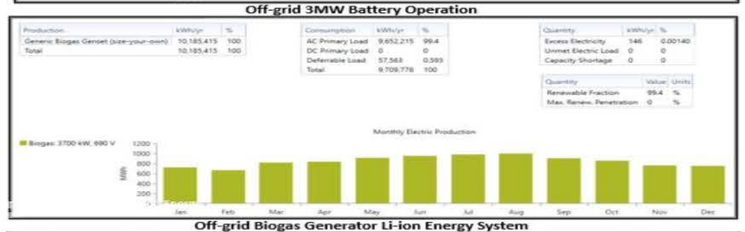

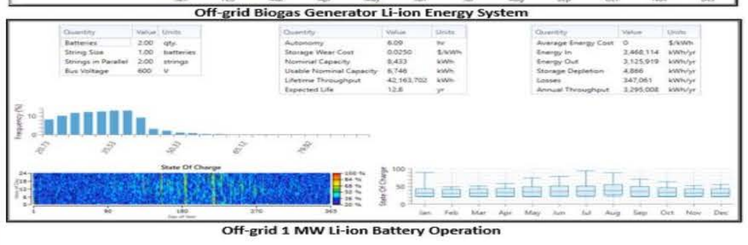

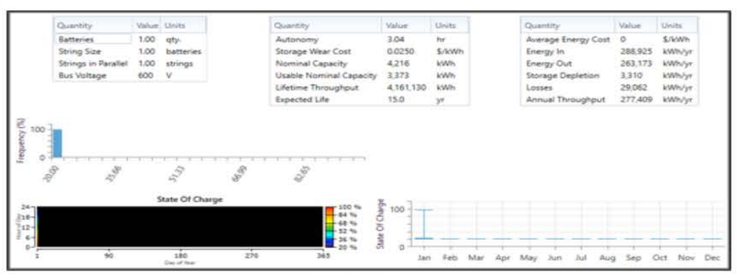

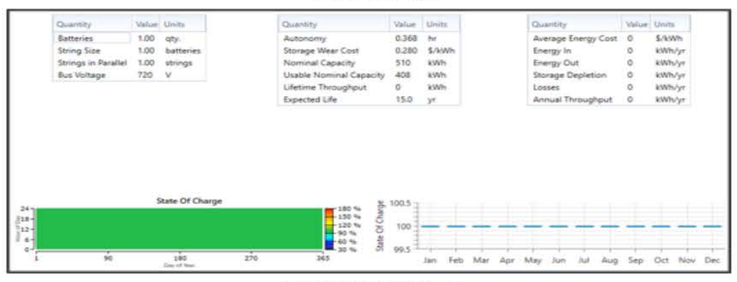

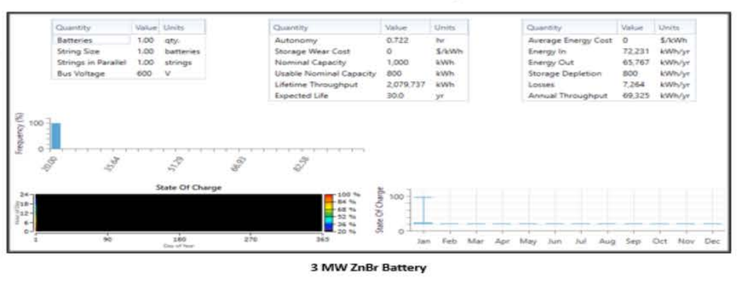

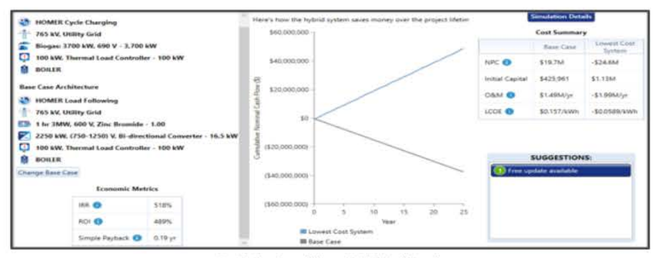

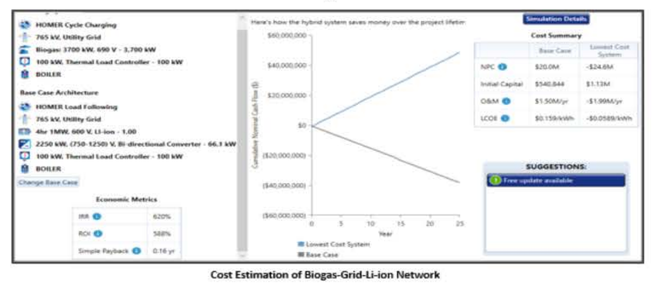

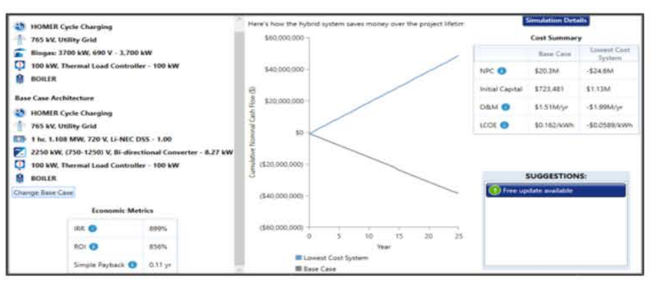

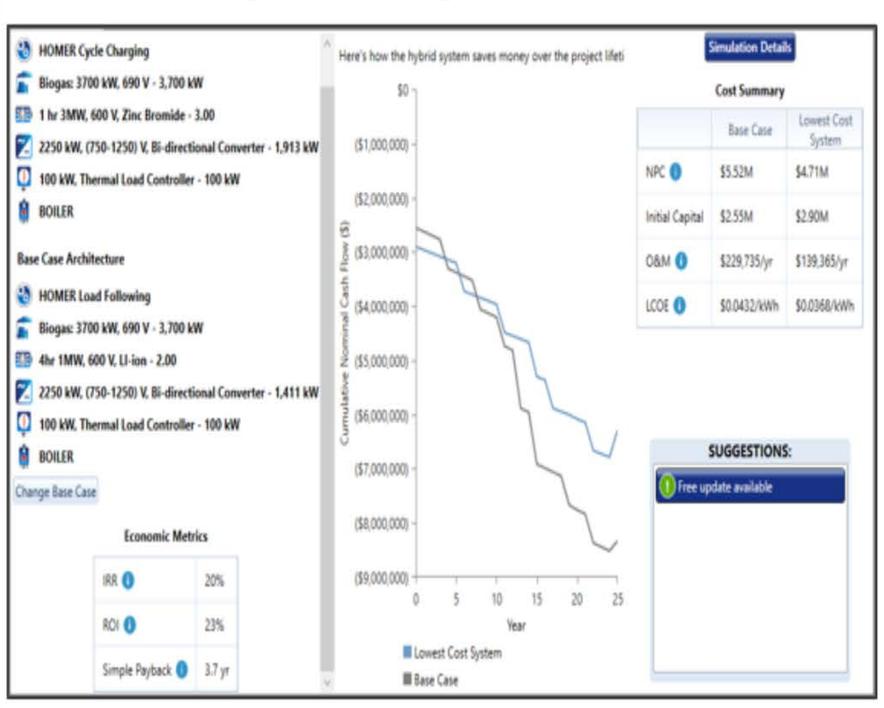

The IRR: Internal Rate of Return and ROI: Return on Investment was feasible under the operation of biogas generator with Zinc bromide and lithium-ion batteries only when the microgrid system was disconnected from the utility grid network. The Li-NEC distribution storage system was not feasible economically and technically at the off-grid mode.

Conclusion

Storage Management System

The ZnBr battery gave out more energy (5,335,103 kWh/yr) than Li-ion battery (3,125,919 kWh/yr) and in turn consumed more energy (5,927,893 kWh/yr) than Li-ion battery (3,468,114 kWh/yr) at the off-grid operational mode.

The grid connected mode of the intgrated biogas-storage network indicated that Li-ion consumed (288,925 kWh/yr) and gave out (263,173 kWh/yr) more energy than the ZnBr input (72,231 kWh/yr) and output (65,767 kWh/yr) energies. The Li-NEC battery maintained its maximum state of charge (100 %) with no energy gain or energy loss.

Multiple Control Strategy

The Cycle Charging strategy enables the utility grid network to feed the load and allows the biogas generator to charge the batteries fully.

The Load following strategy allows the utility grid and biogas generator to operate simultaneously against capacity shortage from the power sources and feed the load to produce excess electricity.

The biomass generator's penetration was greater than the grid's penetration. There was no shortage in capacity from the energy sources at the grid and off-grid modes and the loads were fully met.

Grid sales was dominant over the grid purchase at the grid configurations' set up.

Flexible Operation

The unreliable utility grid and stable DC power sources (batteries) received support from the stable AC power source (biomass gasifier generator).

The utility grid system can send excess electricity to the hybrid storage system and storage load, respectively.

The utility grid system can also receive excess electricity from the stable AC power (biogas generator) and DC power (batteries) sources after serving the load fully.

Econometrics Analysis

The integrated grid-biomass-storage system estimated the Li-NEC network configuration as the most economical efficient system with the highest IRR: 899 %, ROI: 856 %, payback period (0.11 year) over the Li-ion network system: IRR (620 %), ROI (588 %), payback period (0.16 year) and Zn-Br network system: IRR (518 %), ROI (489 %) with payback period (0.19 year).

The off-grid network shows the Zn-Br network configuration as the only economically feasible system with IRR (20 %), ROI (23 %) and payback period of 3.7 years while Li-ion and Li-NEC network system are not economically feasible.

In overall, the grid connected system is more technically and economically feasible than the off-grid (biogas-storage system configuration).

Acknowledgement

รหัส BIBF660068
โครงการการพัฒนาผู้มีศักยภาพสูงของกลุ่มมหาวิทยาลัยเทคโนโลยีราชมงคล ระดับหลังปริญญาโทและปริญญาเอก เพื่อส่งเสริมการวิจัยเชิงลึกในการยกระดับขีดความสามารถของอุตสาหกรรม"

The authors are thankful for the financial assistance provided by the NSRF via the Program Management Unit for Human Resources & Institutional Development Research and Innovation [B13F660068]

BRAINPOWER CONGRESS 2023

ร่วมกันสร้างและขับเคลื่อนงานวิจัยขั้นแนวหน้า
สู่อุตสาหกรรมแห่งอนาคต

การใช้เศษขยะอุตสาหกรรมจากการผลิตหลอดยาสีฟันสำหรับผลิตหวายเทียมจักสานเฟอร์นิเจอร์ภายในอาคาร

The utilization of industrial waste from the production of the toothpaste tube to produce artificial rattan for fabricating indoor furniture

นายวิศรุจน์ จันแป้น (นักวิจัยหลังปริญญาโท) [1] และ รองศาสตราจารย์ ดร.อนินท์ มีมนต์ (นักวิจัยพี่เลี้ยง) [2]

[1] บริษัท แอดวานซ์ แมท จำกัด และ [2] มหาวิทยาลัยเทคโนโลยีราชมงคลธัญบุรี

บทนำ

หลอดยาสีฟันเมื่อพิจารณาจากภายนอกจะไม่สามารถรู้ได้เลยว่ามีองค์ประกอบอะไรบ้าง ในรูปที่ 1 แสดงถึงองค์ประกอบที่สำคัญของวัสดุที่นำมาผลิตเป็นหลอดยาสีฟัน ซึ่งประกอบไปด้วยชั้นของวัสดุหลากหลายชนิดทั้งพลาสติกและโลหะ เช่น พอลิเอทีลีน, พอลิเอทีลีนโคพอลิเมอร์ และชั้นของอะลูมิเนียม ซึ่งวัสดุเหล่านี้จะทำหน้าที่เป็นบรรจุภัณฑ์ที่รักษาคุณภาพของยาสีฟันให้มีกลิ่น รสชาติ และควบคุมคุณภาพของเนื้อยาสีฟันให้มีความสดใหม่ เมื่อเป็นขยะแล้ววิธีการกำจัดส่วนใหญ่จะเป็นรูปแบบของการฝังกลบไม่สามารถรีไซเคิลหรือนำกลับมาใช้ใหม่เนื่องจากมีส่วนประกอบของวัสดุที่หลากหลายจึงถูกจัดให้อยู่ในกลุ่มของขยะกำพร้า (ขยะที่ไม่สามารถรีไซเคิลได้) จากข้อมูลทางด้านสิ่งแวดล้อมมีการนำเสนอข้อมูลขยะจากหลอดยาสีฟันในหนึ่งปีที่สหรัฐอเมริกา พบว่ามีขยะที่เกิดจากหลอดยาสีฟัน 1,000 ล้านชิ้น และอังกฤษมีขยะหลอดยาสีฟัน 300 ล้านกว่าชิ้น และมีการประมาณการว่าถ้านำเอาหลอดยาสีฟัน 300 ล้านชิ้นมาเรียงต่อกันจะมีความยาวประมาณ 75,000 กิโลเมตร ซึ่งสามารถพันรอบโลกได้ 2 รอบ จากตัวอย่างข้อมูลของปริมาณขยะจากหลอดยาสีฟันทำให้นึกถึงจำนวนประชากรในประเทศไทยจำนวน 80 ล้านคน จะมีจำนวนขยะเหล่านี้เหลือทิ้งอยู่ในปริมาณเท่าไร หรือพิจารณาไปถึงกระบวนการผลิตหลอดยาสีฟันจะมีปริมาณขยะอุตสาหกรรมที่เหลือทิ้งอีกจำนวนเท่าไร และแน่นอนว่าปริมาณของขยะจากบรรจุภัณฑ์นี้จะมีการเพิ่มปริมาณขึ้นตามการขยายตัวของประชากร ซึ่งจะก่อให้เกิดปัญหาขยะจากบรรจุภัณฑ์ที่ใช้แล้วหรือขยะที่เหลือทิ้งจากกระบวนการผลิตบรรจุภัณฑ์เหล่านี้มากขึ้นไปด้วย และในปัจจุบันปัญหาเหล่านี้ส่งผลกระทบอย่างมากต่อสิ่งแวดล้อม ดังนั้นการศึกษาวิจัยในกระบวนการนำขยะอุตสาหกรรมที่เหลือทิ้งจากบรรจุภัณฑ์หลอดยาสีฟันที่สะอาดยังไม่ได้มีการปนเปื้อนให้สามารถรีไซเคิลกลับมาใช้ใหม่ได้ในรูปแบบของผลิตภัณฑ์ชนิดอื่นโดยไม่ก่อมลพิษ จะสามารถลดปัญหาด้านสิ่งแวดล้อมไปได้มาก รวมทั้งส่งเสริมการสร้างแพลตฟอร์มการพัฒนาธุรกิจรูปแบบเศรษฐกิจหมุนเวียน การพัฒนาเทคโนโลยีและนวัตกรรมการใช้วัตถุดิบรอบสองเพื่อสร้างมูลค่าเพิ่มในระดับอุตสาหกรรมหมุนเวียน สร้างกระบวนการพัฒนาปัจจัยเอื้อ ข้อมูลฐาน และมาตรฐานด้านเศรษฐกิจหมุนเวียน เพื่อให้เกิดการกระบวนการหรือการตระหนักถึงการอยู่กับสิ่งแวดล้อมได้อย่างยั่งยืน

ขยะอุตสาหกรรมจากการผลิตสีฟันสำหรับผลิตหวายเทียมจักสานเฟอร์นิเจอร์ภายในอาคาร

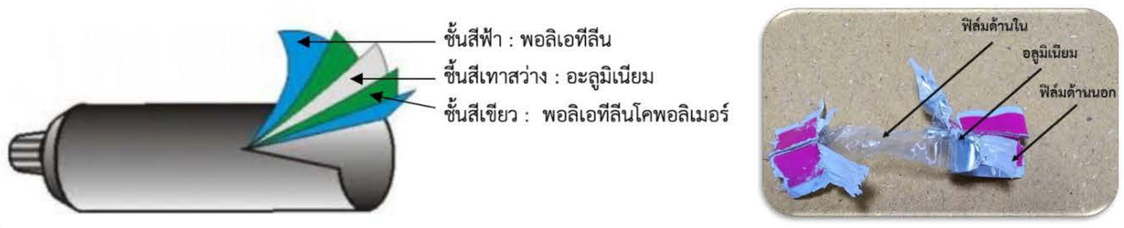

รูปที่ 1 องค์ประกอบของวัสดุที่ผลิตเป็นหลอดยาสีฟัน

รูปที่ 2 เศษขยะอุตสาหกรรมจากการผลิตสีฟันที่จะใช้สำหรับผลิตหวายเทียมจักสานเฟอร์นิเจอร์ภายในอาคาร

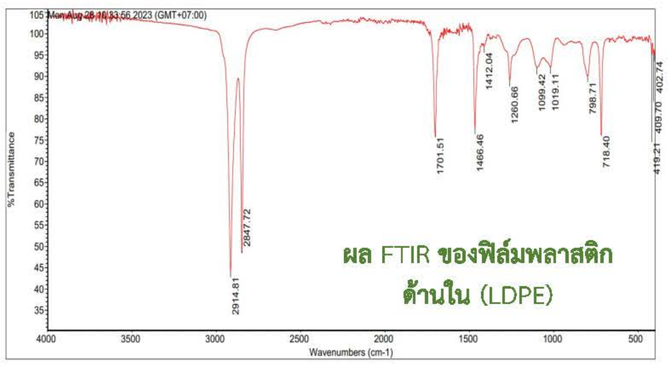

ผล FTIR ของฟิล์มพลาสติกด้านใน (LDPE)

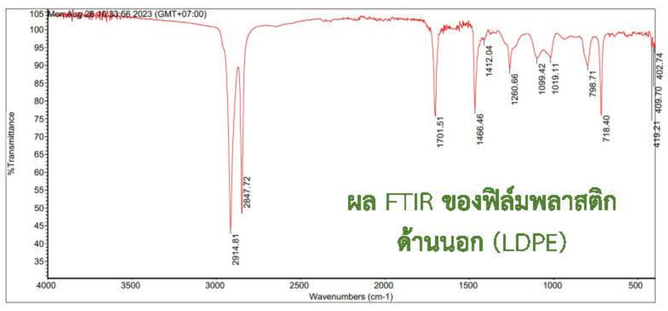

ผล FTIR ของฟิล์มพลาสติกด้านนอก (LDPE)

ผลการตรวจสอบชนิดของฟิล์มพลาสติกที่เป็นองค์ประกอบของหลอดยาสีฟัน

เครื่องฟลูเรียร์ทรานส์ฟอร์มอินฟราเรดสเปกโทรมิเตอร์

(Fourier transmission infrared (FTIR) ; ATR Model : Nicolet iS5-iD7 Thermo Scientific)

รูปที่ 3 ผลการทดลองขึ้นรูปเม็ดคอมพาวนด์จากขยะอุตสาหกรรมการผลิตหลอดยาสีฟัน

การทดสอบสมบัติทางกลของคอมพาวนด์รีไซเคิลจากขยะอุตสาหกรรมการผลิตหลอดยาสีฟัน

การทดสอบแรงดึง (Tensile test) **ตามมาตรฐาน** ASTM D638

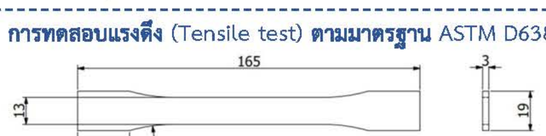

a) ขนาดมาตรฐานของชิ้นทดสอบแรงดึง

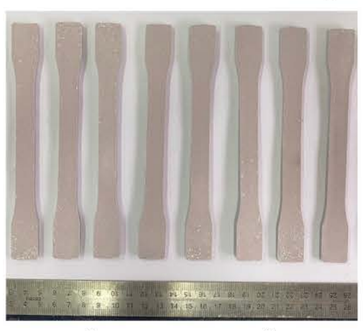

b) ชิ้นทดสอบแรงดึงจากการฉีดขึ้นรูป

b) เครื่องทดสอบแรงดึง

การทดสอบแรงดัด (Bending test) **ตามมาตรฐาน** ASTM D 790

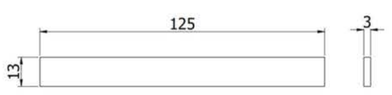

a) ขนาดมาตรฐานของชิ้นทดสอบแรงดัด

b) ชิ้นทดสอบแรงดัด

c) เครื่องทดสอบแรงดัด

การทดสอบแรงกระแทก (Impact test) **ตามมาตรฐาน** ASTM D256

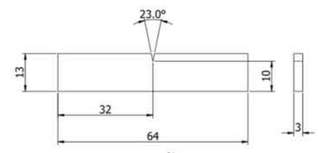

a) ขนาดมาตรฐานของชิ้นทดสอบแรงกระแทก

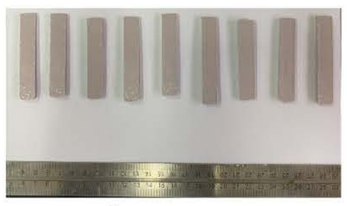

b) ชิ้นทดสอบแรงกระแทก

c) เครื่องทดสอบแรงกระแทก

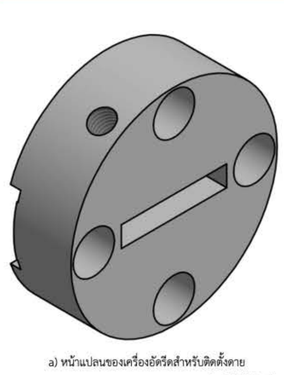

a) หน้าแปลนของเครื่องอัดรีดสำหรับติดตั้งตาย

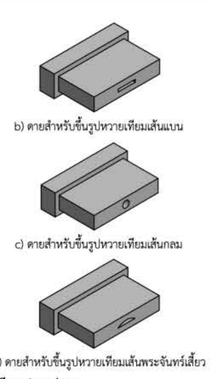

b) ตายสำหรับขึ้นรูปหวายเทียมเส้นแบน

c) ตายสำหรับขึ้นรูปหวายเทียมเส้นกลม

d) ตายสำหรับขึ้นรูปหวายเทียมเส้นพระจันทร์เสี้ยว

การออกแบบตายสำหรับอัดรีดเส้นหวายเทียมรูปแบบต่าง ๆ

กิตติกรรมประกาศ

รหัส BIBF660068 **โครงการการพัฒนาผู้มีศักยภาพสูงของกลุ่มมหาวิทยาลัยเทคโนโลยีราชมงคล ระดับหลังปริญญาโทและปริญญาเอก เพื่อส่งเสริมการวิจัยเชิงลึกในการยกระดับขีดความสามารถของอุตสาหกรรม**

BRAINPOWER CONGRESS 2023

ร่วมกันสร้างและขับเคลื่อนงานวิจัยขึ้นแนวหน้า
สู่อุตสาหกรรมแห่งอนาคต

Development of a smart grid stabilization system using a diesel engine from waste fuel

Paitoon Laodee[a], Pisit Maneechot[a], Unchittha Prasatsap[a], Sakda Somkun[a], and Preecha Sriprapakhan[b*]

[a]School of Renewable Energy and Smart Grid Technology, Naresuan University, Tha Pho Subdistrict, Mueang Phitsanulok District, Phitsanulok Province 65000

[b]Faculty of Science Mahasarakham University, Kham Riang Subdistrict, Kantharawichai District Maha Sarakham Province 44150

Rationale

The plastic waste amount 13.97 percent of the total waste generated of 9,600 tons per day. Thailand has plastic waste amounting to 13.97 percent of the total amount of waste generated or 9,600 tons/day. The amount of waste increased by 100 tons/day or 1 percent compared to the amount of plastic waste in 2019. The rate of plastic waste generation increased from 96 grams/person/day increased from before to 137 grams/person/day. This is an alarming number. If there is no smart waste management strategy, it will have an impact in the near future. Disposing of plastic waste through the pyrolysis process into oil. Plastic waste can be turned into advanced bio-oil to be used as fuel for internal combustion engines for generating electricity to enhance the stability of smart grids using IoT systems. to help manage and control work. which is waste management and electricity production using alternative fuels Including to strengthen the electrical stability of the smart grid system in the future for energy security to support economic and technological growth.

Methods

This research method an experimental, main parameter is approximate diesel fuel consumption rate (gal/h) of the IC-engine. The characteristic of electricity showing, current (A), voltage (V), Frequency (Hz),

Figure. 1. Modified a Diesel IC-engine

Figure. 2. Generator connected with IC-engine setting up

Figure. 3. Fuel freed stock

Fig. 1. showed the diesel IC-engine type is motor diesel horizontal 4-stroke, direct injection. 1 cylinder, displacement volume is 0.638 lit. Specific fuel consumption is 181 gr/ hp*h.

Fig.2. showed the generator connecting with IC-engine, the generator is a Permanent Magnet Synchronous Generator (PMSG), the maximum power is 2 kW power: 220V/5.2A/50Hz and maximum speed 1000 rpm

Fig. 3. showed modified a plastic water bottle as a fuel freed stock, it was marked at a certain point.

Results & Discussion

This result was showing preliminary testing of the internal combustion engine, IC-engine combine with the generator testing

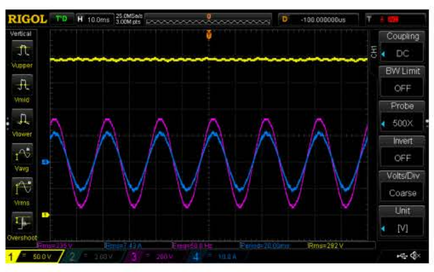

Figure. 5. Relationship Torque and Power of generation

Fig.5. shows preliminary testing of generator testing The waveform from the inverter is a sine wave with current and voltage in the same phase and a frequency of 50 Hz. Rms 7.43A

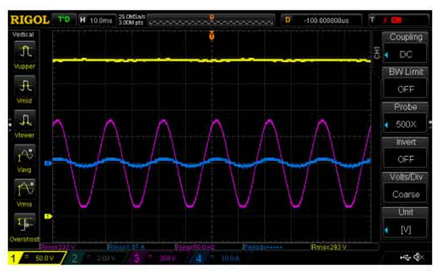

Figure. 6. Relationship Torque and Power of generation

Fig.6. shows The waveform from the inverter is a sine wave with current and voltage in the same phase and a frequency of 50 Hz. Rms 1.07A

Comparing difference current between 7.43A and 1.07 A, the effect of current show the waveform from the inverter is a sine wave (see Fig.5. and Fig.6.)

Table. 1. Classification of the plastic types for conversion into fuel oil

Plastic types	Characteristic	Packaging example	Type of oil
High-density Polyethylene, HDPE	Quite opaque, Strong, High-density	Baby bottles, cosmetic bottles, plastic bags, trash cans, chemical containers	Diesel
Low-density Polyethylene, LDPE	Translucent, Low-density	Frozen food bags, cling film, storage bags and copper clad cables	Diesel
Polypropylene, PP	Light weight, heat resistant	Bottle caps, food containers, hot bags and straws	Diesel
Polystyrene, PS	Fragile, easily broken	Cups, plates and drinking glasses	Gasoline

The crude pyrolysis oil created from plastic is produced by the pyrolysis process which involves heating the plastic in the non-appearance of oxygen, to break down the long-chain hydrocarbons to shorter-chain hydrocarbons. The shorter chain hydrocarbons are used to produce liquid fuels.

Figure 4. Pyrolysis process with plastic waste

The choice of temperature, heating rate and catalyst depends on the feedstock and the desired products. For example, wood and other biomass are typically pyrolyzed at temperatures ranging from 400°C to 600°C to produce bio-oil, while plastic waste can be pyrolyzed at temperatures ranging from 400°C to 700°C to produce liquid fuel.

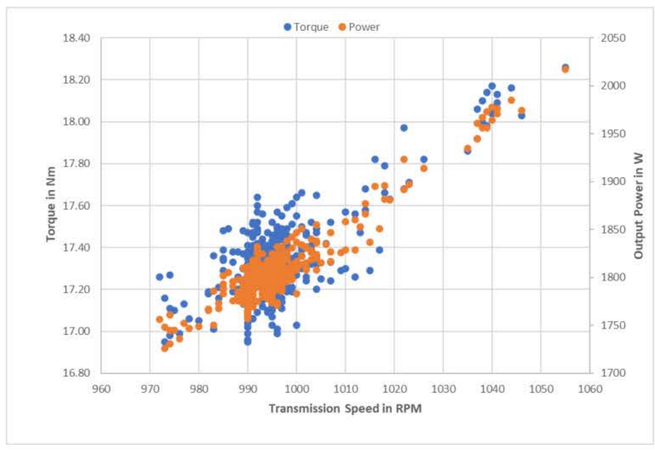

Figure. 7. Relationship Torque and Power of generation

From Figure 7. the preliminary test was show the maximum speed, minimum speed, and average speed of transmission was 1055 rpm, 972 rpm, and 996.74 rpm respectively. The maximum power 2.02 kW, Min. power 1.73 KW, and average of power is 1.81 kW of the generator. An approximate diesel fuel consumption rate, the generator capacity between 20 – 60 kW in case of full loads 1.6 – 4.8 gal/h. The speed can make a difference in fuel consumption because the speed is going up and down and is not constant.

Conclusion

The mains of ejective study the plastic west conversion to energy for supplying the IC-engine to produce an electricity for supplying the gride connection, the grid connection is a small generation system of the smart grid system. The preliminary testing was shown abilities of the crude pyrolysis oil created from plastic, it can be used as fuel for internal combustion engines.

Acknowledgements

This research has received funding support from the NSRF via the Program Management Unit for Human Resources & Institutional Development, Research and Innovation [grant number B13F660133]. Thank you, The School of Renewable Energy and Smart Grid Technology, Naresuan University. Thank you, ADC MICROSYSTEMS COMPANY LIMITED

BRAINPOWER CONGRESS 2023

ร่วมกันสร้างและขับเคลื่อนงานวิจัยขึ้นแนวหน้า
สู่อุตสาหกรรมแห่งอนาคต

Production of biogas from bagasse with the innovation of extracting bacteria from the soil as decomposers

Anchaleeporn Seesatat [a,b] , Surachai Rattanasuk [a] , Kanin Bunnakit [a] , Preecha Sriprapakhan [b,c] , Ritchard Artkla [a], Pisit Maneechot [b*]

[a] Renewable Energy Research Unit (RERU), Faculty of Liberal Arts and Science, Roi-Et Rajabhat University, Selaphum, Roi-Et, 45120, Thailand

[b] School of Renewable Energy and Smart Grid Technology (SGTECH), Naresuan University, Phitsanulok, 65000, Thailand

[c] Takasila Research and Development Center of Energy Department of Physics, Faculty of Science, Maha Sarakham University, Kantara Wichai, Maha Sarakham, 44150, Thailand

Introduction

Thailand's significant reliance on the agricultural sector confers it with a competitive edge. The agricultural establishment encompasses a multitude of components that are intricately linked to the process of production. Cash crops, such as sugarcane, constitute a significant proportion of the biomass within the agricultural sector. The creation of biogas from bagasse is also a topic of significant interest. From a chemical perspective, bagasse exhibits a notable abundance of fiber and a considerably elevated cellulose content. Nevertheless, it is imperative to customize it before utilizing it. This study aimed to explore several approaches for the pre-treatment of bagasse prior to its utilization in biogas production. Specifically, the investigation involved the cultivation of bacteria in soil and the isolation of strains capable of producing the cellulase enzyme. The ultimate goal was to facilitate the conversion of bagasse into glucose, which could then be utilized in biogas production processes. The examination of biogas production systems for both corporate entities and local populations has also been undertaken.

Method

Development of bagasse degradation bacteria

The objective of this study was to isolate cellulase-producing bacteria from soil samples. The experiment commences with the acquisition of a soil sample weighing 1 gram. The subsequent step involves the isolation of cellulase-producing bacteria through the assessment of clearing zone formation on a solid LB medium supplemented with 1% carboxymethyl cellulose (CMC), which is subsequently poured with an iodine solution. Subsequently, the concentration of Reducing Sugar derived from bagasse was analyzed for its potential utilization as a precursor in the generation of biogas.

Production of biogas from bagasse

Biogas production is conducted utilizing exclusively liquid reactants, namely the solid fraction derived from the pretreatment of bagasse with soil-extracted bacteria to generate glucose. This process takes place within a sizeable 1.2 cubic meter digester, facilitating biogas fermentation. The initial procedure involves the addition of 50 liters of glucose reactant and 15 liters of biocatalyst, followed by thorough mixing to remove oxygen by means of nitrogen gas. The process of anaerobic digestion was conducted at a controlled temperature of 39±0.5 °C for a period of 20 days. The control group consisted of untreated bagasse samples. Biogas samples were collected at 24-hour intervals and subsequently subjected to analysis.

Graphical Method

Isolation of cellulase-producing bacteria

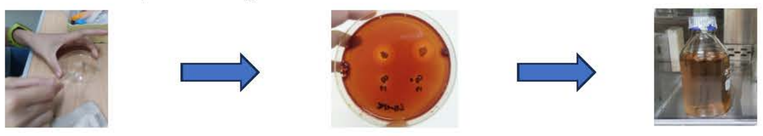

Production of biogas from bagasse

Acknowledgements

This research has received funding support from the NSRF via the Program Management Unit for Human Resources & Institutional Development, Research and Innovation [grant number B13F660133]. The authors also appreciate the Green Millennium Co., Ltd., Bangkok, Thailand for equipment support during the research.

Results and Discussion

Table 1 On the ninth day, there was a decrease in the sugar concentration of the digested rice straw.

Isolate	Reducing sugar concentration
SL1	1.926
SL2	1.788
SL3	1.864
SL4	1.794

Cellulase produced bacteria were taken from the soil in this study. The bacteria with the greatest ability to break down straw has been identified as SL1.

Following each degradation interval, alterations in pH and total volatile fatty acid (TVFA) content have been observed.

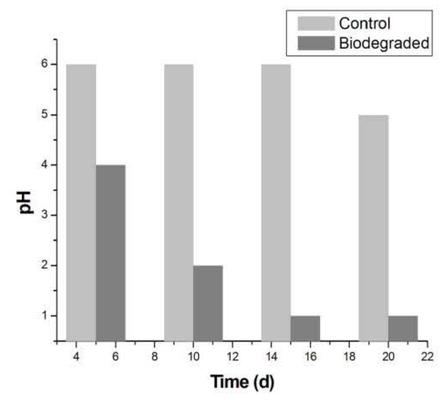

Figure 1 Changes in pH over time

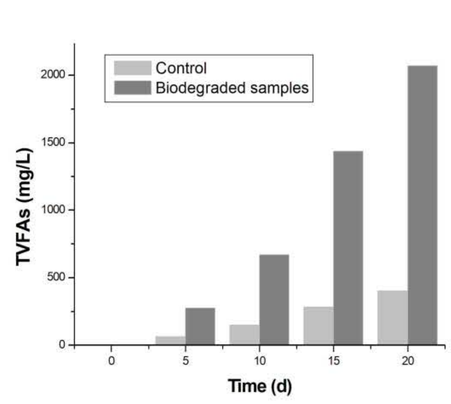

Figure 2 Changes in TVFA concentration over time

Biomethane production

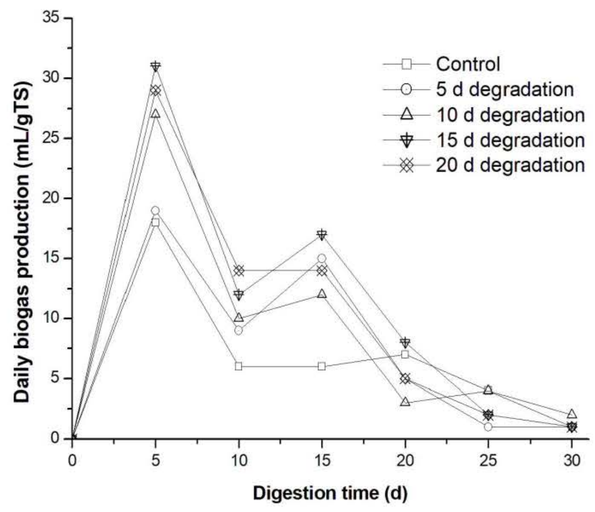

Figure 3 The daily generation of biogas from both untreated and biologically decomposed rice straw.

Conclusion

In this work, bacteria capable of generating cellulase were isolated from soil samples. Previous studies have demonstrated that the bacterial inoculant SL1 exhibits notable cellulolytic and lignolytic activity, making it the most effective candidate for bagasse decomposition. The utilization of lignocellulose can be enhanced by many approaches. The degradation process reaches its peak efficiency within a 15-day timeframe, resulting in significant biogas and methane yields of 316.10 mL/gTS and 171.72 mL/gTS, respectively. Additionally, this optimized period of degradation contributes to a reduction in the overall time required for biogas production.

BRAINPOWER CONGRESS 2023

ร่วมกันสร้างและขับเคลื่อนงานวิจัยขึ้นแนวหน้า
สู่อุตสาหกรรมแห่งอนาคต

Korat TRC Plastic Co., Ltd.

Innovative Production of Glowing Recycled Plastic Filament for 3D Printers

Phatthawit Siripaiboonsub[a], Wannisa Nutkhum[a], Boonyabhorn Duangsa[a], Supatthra Muparang[a], Jetnipat Pimollukanakul[a], Trakulphan Kitpo and Jittiwat Nithikarnjanatharn[a] *

[a]Department of Industrial Engineering Faculty of Engineering and Technology, Rajamangala University of Technology Isan Muang, Nakorn Ratchasima 30000

Rationale

The timely creation of prototype products within a reasonable cost by employing fast prototyping technology is a crucial aspect for the future of the manufacturing industry. Currently, technological innovations in 3D printing have been elevated from conventional printing technology to three-dimensional (3D) printing, allowing the development of cost-effective, high-quality technology. Key components of 3D printing technology include plastic filaments. According to the study, the prices for new types of plastic filaments range from 580 to 1800 baht per kilogram. The new plastic filaments have a high production cost. However, by utilizing filaments produced through the recycling process, the cost of production can be reduced, benefiting both the economy and the environment. Therefore, if the properties of plastics that can reduce electricity consumption during the manufacturing process are studied, it is possible to reduce production costs and energy consumption. This research focuses on using recycled and supplemented light-reactive plastic filaments in 3D printing technology to compare the mechanical and physical properties of the filaments. Additionally, the research examines the light emission duration in the dark of the recycled plastic filaments produced through the recycling process, contributing to the development of plastics in the circular economy, reducing environmental destruction, and promoting sustainable industrial product quality.

Research Methodology

this research involves exploring relevant theories related to the materials used for research, as well as the equipment and tools employed in the research process. It encompasses the rapid prototyping of objects using the Fused Deposition Modeling (FDM) method, designing test objects, conducting mechanical property tests, and analyzing experimental results

Production of Plastic Filaments

Mixing 30% polylactic acid (PLA) and 70% recycled polypropylene, supplemented with the light-reactive additive 'Ultimate Glow' in green color, was conducted using a twin-screw extruder at a temperature of 220 degrees Celsius. The addition of the light-reactive additive was carried out in three proportions: 0.3%, 0.5%, and 1%, as show in Fig 1

Drawing plastic filaments of polylactic acid blended with recycled polypropylene and supplemented with the light-reactive additive was performed using a filament drawing apparatus. The aim was to achieve a filament diameter of 1.75±0.05, as show in Fig 2“

Fig. 1 twin-screw extruder

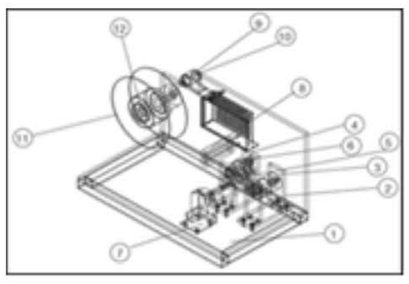

Fig. 2 Plastic filament extruder equipment.

Fig. 3 The characteristics of plastic filaments used for 3D printing

From the process of drawing plastic filaments of polylactic acid blended with recycled polypropylene and supplemented with the light-reactive additive, it was observed that at proportions of 0.5% and 1%, the filament did not maintain a consistent diameter. The size varied between 1.74 to 1.76 mm due to uneven dispersion of the light-reactive additive, resulting in irregular filament size. Conversely, at a proportion of 0.3%, the filament exhibited a consistent diameter, closely resembling the original PLA prototype. As show in Fig 3

Equipment and Tools Used in the Process

The following equipment and tools were utilized in the research process: a 3D printer (Delta Kossel Rostock MicroMake), pre-built software (Flash Print), a Durometer for hardness testing (Shore D), a Fluorescence Spectrophotometer for measuring chemical fluorescence, and a tensile strength testing machine.

Design of Test Objects

Test objects were created according to ASTM 638 Type V standards, including test pieces for surface inspection measuring 15 mm in width, 15 mm in length, and 3 mm in thickness. The STL file format, a standard for 3D printing, was then converted from the data file for creating the test objects, as shown in Fig 4 (A) for mechanical property testing and Fig 4 (B) for surface inspection and layer alignment.

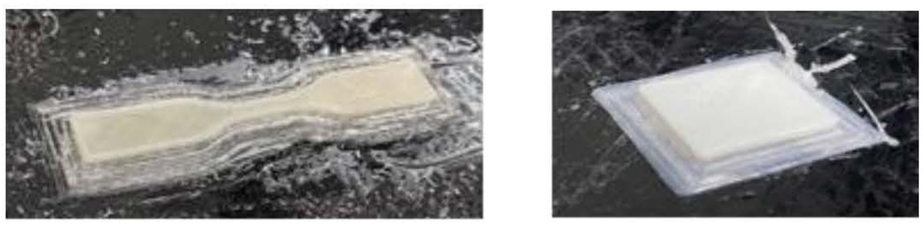

(A) (B)

Fig. 4. The characteristics of the tensile test specimen are used to create 3D printed objects.

Rapid Prototyping Using Fused Deposition Modeling (FDM)

The process involved importing the 3D model file into the Flash Print program for rapid prototyping. The Flash Print program was used to slice the 3D model and set parameters for prototyping, such as the nozzle temperature (set at 230 °C), print bed temperature (set at 80 °C), and 100% infill for the plastic material.

Mechanical and Physical Property Testing

Mechanical property tests included Tensile Properties and Durometer hardness testing (Shore D) according to ASTM D2240. Physical property tests included Melt Flow Index (MFI) testing according to ASTM D1238 and Fluorescence Spectrophotometer testing, stimulating light at four wavelengths (300, 350, 450, and 500 nm) for surface fluorescence when subjected to 3D printing."

Conclusion

Production of recycled polypropylene plastic lines mixed with polylactic acid, supplemented with three different proportions of fluorescent agent

All three proportions of added fluorescent material exhibited similar mechanical properties, yet the 0.3% proportion demonstrated higher stretchability compared to the other two proportions. It also displayed physical similarities to polylactic acid strands with added fluorescent agent, as observed through tearing and the arrangement of plastic layers on the sides. Comparative analysis of mechanical properties between polylactic acid plastic filament with fluorescent additives and recycled polypropylene plastic filament mixed with polylactic acid and fluorescent additives revealed that the former exhibited higher mechanical properties. This difference is attributed to the use of recycled polypropylene plastic strands mixed with polylactic acid and supplemented with a fluorescent agent, resulting in a decrease in mechanical properties. The polylactic acid plastic line with a fluorescent additive has an appropriate wavelength in the ultraviolet range, similar to the recycled polypropylene plastic line mixed with polylactic acid and a fluorescent additive, at a proportion of 0.3 percent. Considering these factors, an additive Proportions of 0.3 percent is deemed optimal for producing filaments for use in 3D printers.

Acknowledgements

This research has received funding support from the NSRF via the Program Management Unit for Human Resources & Institutional Development, Research and Innovation [grant number B13F660133] Thank you , Rajamangala University of Technology Isan. Thank you, Choonhavan Institute For Sustainable SMEs Development. Thank you, **Korat TRC Plastic Co., Ltd.**

Results

Melt Flow Index Test Results:

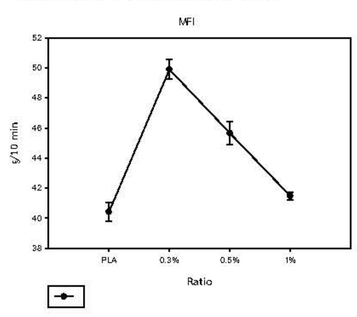

The average melt flow index (MFI) test results for the polylactic acid (PLA) and recycle polypropylene, supplemented with the light-reactive additive composite were 40.408 grams/10 minutes, and for polypropylene-recycled PLA composite with light-reactive additives at concentrations of 0.3%, 0.5%, and 1%, the average MFI results were 49.896, 45.660, and 41.472 grams/10 minutes, respectively. The MFI values were observed to decrease with an increase in the concentration of light-reactive additives, with the 0.3% concentration showing the highest MFI, indicating better flowability. This suggests improved stretchability, especially compared to the 1% concentration, where the MFI was closer to that of regular PLA. As show in Fig 5

Fig. 5 The characteristics of the tensile test specimens

Mechanical Property Test Results:

From Fig 6, the relationship between strain and stress of the test specimen is shown. It can be observed that the stress-strain relationship of the specimen with the proportion of added polypropylene-recycled PLA composite with light-reactive additives is highest. However, Proportions of 0.3, 0.5, and 1, the relationship between strain and stress decreases.

The results of the elasticity test demonstrate the capability of the proportion with the addition of polypropylene-recycled PLA composite with light-reactive additives at 0.3%. It shows a greater ability for elongation compared to other proportions of photosensitive additives. This corresponds to the characteristics of the stress-strain graph of the test specimen, as depicted in Fig 7

Test results for the modulus of elasticity (Young's modulus) of polylactic acid lines with fluorescent additives averaged 873.304 megapascals, and recycled polypropylene lines mixed with polylactic acid added fluorescent agent. The proportions of adding fluorescent agent of 0.3, 0.5, and 1% averaged 463.546 It was observed that polylactic acid lines with added fluorescent agent are 46.92%. in Fig 8

Results of the tensile strength test: Polylactic acid added to the fluorescent agent is The prototype strands were found to have an average tensile strength of 54.6588 megapascals. And the results of the tensile strength test of recycled polypropylene plastic s mixed with polylactic acid added a fluorescent agent. The proportions of adding fluorescent agent of 0.3, 0.5 and 1 percent were on average 27.371 megapascals. From the graph it was found that polylactic acid added fluorescent agent. The tensile strength is higher. This is because the addition of recycled polypropylene has been used and the adhesion of the polymer has decreased, as shown in Fig 9, which is in line with the results of the modulus of elasticity test.

Hardness test results of polylactic acid with a fluorescent additive: 78.667 Shore D, and recycled polypropylene mixed with polylactic acid with a fluorescent additive. The proportion of adding fluorescent agent was 0.3, 0.5, and 1 percent. The average hardness values were 67.390 Shore D. It was found that adding fluorescent agent increased the hardness properties. This corresponds to the modulus of elasticity and tensile strength, as shown in Fig 10.

Physical Property Testing

This pertains to the attributes of a tensile test specimen that reveal the physical features of the workpiece influencing its mechanical properties, as outlined in Table 1.

Table. 1. Characteristics of Physical Absence.

TYPE	Work piece
PLA Original	
PLA+PP+ 0.3 %	
PLA+PP+ 0.5%	
PLA+PP+ 1%	

From the process of molding the polylactic acid plastic line, the fluorescent agent is added. The specimen's surface is consistently uniform and smooth, with a cloudy white color attributed. Compared to the characteristics of the workpiece made from recycled polypropylene plastic mixed with polylactic acid and fluorescent additives. In contrast, when examining workpieces produced proportions of 0.3%, 0.5%, and 1%, certain distinctions emerge. Despite maintaining the characteristics of well-molded workpieces, the surfaces of these specimens are not as smooth.

Light luster test

The results of testing the luster of polylactic acid plastic lines with fluorescent additives found that there is a light wavelength for excitation at 509 nanometers. It is close to the proportion of 0.3%, as show in Fig 11.

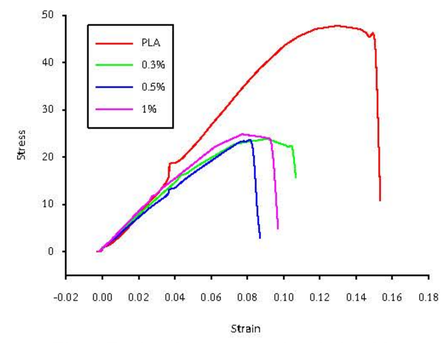

Fig. 6 Testing the stress-strain relationship.

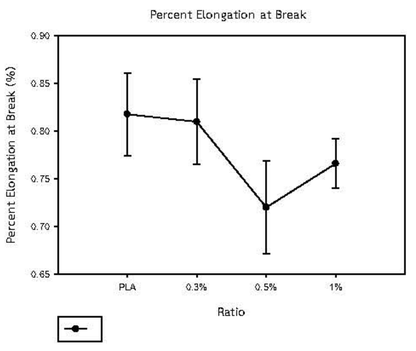

Fig. 7 Characteristics of the test specimen's elongation percentage.

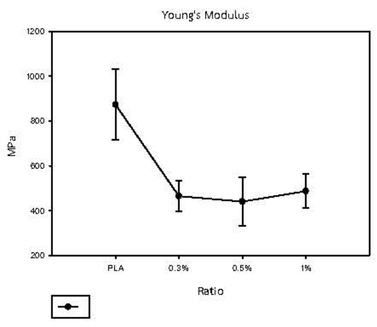

Fig 8 Test specimen characteristics of the modulus of elasticity

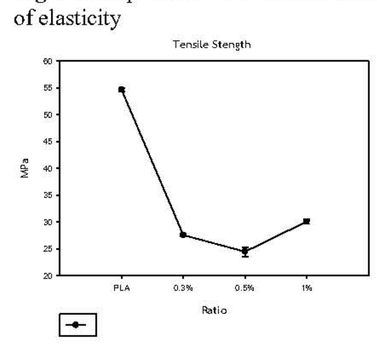

Fig 9 Characteristics of the tensile test specimen

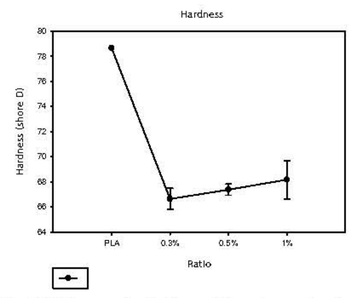

Fig 10 Characteristics of hardness test specimen

Fig 11 glowing workpiece

BRAINPOWER CONGRESS 2023

ร่วมกันสร้างและขับเคลื่อนงานวิจัยขึ้นแนวหน้า
สู่อุตสาหกรรมแห่งอนาคต

Development of luminescent organic dye for ethanol detection via fluorescence technique

Anuwut Petdum [a,b,d], Waraporn Panchan [a,b], Wannee Wasuthep [a,b], Saritsadee Singhathong [c], Panachai Wongsrisupphakul [c], Arnan Silajan [c], Awanwee Petchkongkaew [a,d], Thanasat Sooksimuang [a,b*]

[a] International Joint Research Center on Food Security, 113 Thailand Science Park, Phahonyothin Road, Khlong Luang, Pathum Thani 12120, Thailand.
[b] National Metal and Materials Technology Center (MTEC), 114 Thailand Science Park, Phahonyothin Road, Khlong Luang, Pathum Thani 12120, Thailand.
[c] PTT Oil and Retail Business Public Company Limited, 555/2 Energy Complex, Building B, 12th Floor, Vibhavadi Rangsit Road, Chatuchak District, Bangkok 10900, Thailand.
[d] School of Food Science and Technology, Faculty of Science and Technology, Thammasat University, 99 Mhu 18, Phahonyothin Road, Khong Luang, Pathum Thani 12120, Thailand.
* Corresponding author: thanasas@mtec.or.th

Introduction

Ethanol (EtOH) is one of the most important raw materials for variety of industrial processes including petroleum, medicine, food and beverage. However, the quantity of EtOH in products is very restricted due to safety and regulations. To monitor the ethanol content during industrial production and in products, the preliminary screening of ethanol amount is necessary. Fluorescent sensing technique is one of interesting alternative methods, which provides a fast respond, high accuracy, cost effectiveness and can be applied as a quantitative detection.

This study is a subproject under "Food Security" project. Thus, the main objective is to develop a fluorescent detection system for EtOH in food samples. The pentahelicene, fluorescent organic dyes, were selected as EtOH sensing molecules because these dyes permitted the excellent optical properties benefiting to analytical process of sensing application. In the preliminary test (3 months progress), some selected fluorescent dyes presented a good sensitivity for EtOH detection which had capability to use as fluorescent sensing molecules for EtOH determination.

Methods

The development procedure of pentahelicene molecules as fluorescent sensing molecule for EtOH detection in this work can be described in the following diagrams.

Molecular design, preparation, and characterization.

- ✓ Organic molecular design by combining pentahelicene derivative, a long p-conjugation core; e-acceptor and e-donor.
- ✓ Synthesis and chemical structure characterization including NMR and IR spectroscopy.
- ✓ UV-Visible spectroscopy and fluorescence studies.

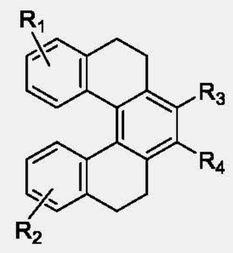

R_1 and R_2 : electron donating groups.
R_3 and R_4 : electron accepting groups.

Figure 1. Chemical structure of pentahelicene dye.

EtOH sensing process.

- ✓ Preliminary screening of selected dyes for EtOH sensing.
- Optimization of sensing system; sample preparation, solvent system and time responsibility.
- Sensitivity studies; limit of detection (LOD), linearity and working range.
- Selectivity and competitive studies; effect of interfering compounds and sensing ability in the presence of interfering species.

Application in real samples.

- Real samples selection, i.e., soy sauce.
- Development of sample preparation method; extraction, solvent systems and reaction time.
- EtOH measurement in real samples.
- Validation parameter; accuracy and precision.

Acknowledgement

This research has received funding support from the NSRF via the Program Management Unit for Human Resources & Institutional Development, Research and Innovation [grant number B13F660129]. For partially supporting this project in terms of financial and infrastructures, we gratefully thank the National Metal and Material Technology Center (MTEC), National Science and Technology Development Agency (NSTDA), PTT Oil and Retail Business Public Company Limited (OR), International Joint Research Center on Food Security (IJC-FOODSEC) and Thammasat University, Thailand.

Results and discussion

Dye 1

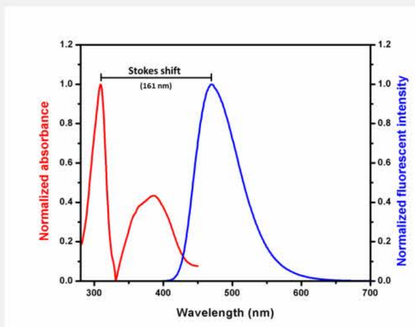

Dye 2

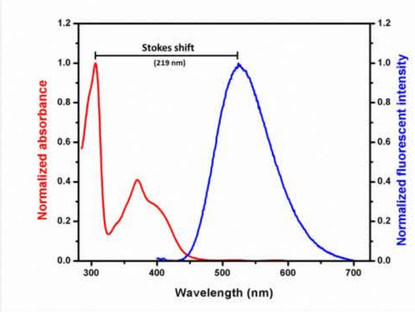

Dye 3

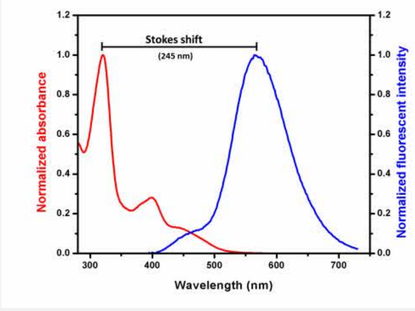

Figure 2. UV-Visible absorption and fluorescent emission spectra of pentahelicene dyes.

Molecular design, preparation and characterization.

Three pentahelicene derivatives with different substituent groups were designed, synthesized and characterized. Three dyes (**Dye 1**, **Dye 2** and **Dye 3**) exhibited a strong fluorescent emission with the maximum peak at 470, 525 and 565 nm, respectively (**Figure 2**). The designed dyes not only presented a high quantum efficiency but also permitted a large Stokes shift around 100 - 250 nm. Because of their high efficiency of optical properties, these dyes were selected as sensing molecules for EtOH detection.

Preliminary screening of EtOH sensing molecules.

Three dyes (**Dye 1**, **Dye 2** and **Dye 3**) as EtOH sensing molecule were quickly screened with EtOH at the concentration of 0, 1, 5, and 10 % v/v by naked eye detection under UV light (**Figure 3**). The emissive color of **Dye 1** was a slight change, while those of both **Dye 2** and **Dye 3** were significant changes (sky blue to orange for **Dye 2** and green to red for **Dye 3**). The results ensured that **Dye 2** and **Dye 3** had the ability to demonstrate for EtOH sensing applications. The EtOH sensing tests of both dyes will be performed, and the results will be described in the next progress report.

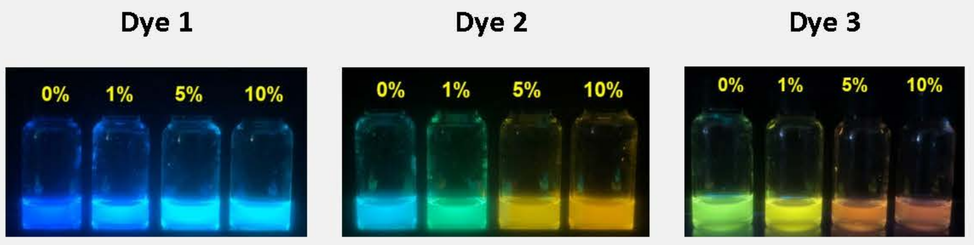

Figure 3. Emissive color of pentahelicene dyes under UV light (365 nm) in the presence of EtOH at different concentration (% v/v)

Conclusion and Future plan

In summary (3 months progress), three dyes were prepared and characterized as EtOH sensing molecule. These dyes exhibited excellent optical properties that were suitable for sensing application. The preliminary sensing results implied that **Dye 2** and **Dye 3** had potential to utilize as EtOH fluorescent sensing molecule. Therefore, both dyes are chosen for intensively study of EtOH sensing process including EtOH sensing optimization, sensitivity, and selectivity; and the progress will be provided in the next report.

BRAINPOWER CONGRESS 2023

ร่วมกันสร้างและขับเคลื่อนงานวิจัยขึ้นแนวหน้า
สู่อุตสาหกรรมแห่งอนาคต

Development of Smart Coatings: Wear and Corrosion-Based Photo Luminescent Sensing for Elevated Temperature Applications

Postdoctoral Researcher: Dr. Narayanasamy Pandiyarajan
Project leader: Asst. Prof. Dr. Peerawatt Nunthavarawong
Co-researcher: Torsak Boonthai, Somprasong Ruannut
Affiliation: The Sirindhorn International Thai-German Graduate School of Engineering (TGGS), King Mongkut University of Technology North Bangkok (KMUTNB), Thailand.
Mechanic Engineering Service Co. Ltd., Bangkok, Thailand.

Introduction:

This research initiative aims to develop a cost-effective and versatile coating with unique properties for various applications. The substrate material chosen for this project is SS400, and the target material for the coating is 60E 13%Chrome steel wire with a diameter of 2.3mm, utilizing Thermal Spray Coating Technology. The primary objectives encompass enhancing the wear and corrosion resistance of the coating through a strategic approach involving the incorporation of sealants. These sealants consist of a combination of silicone resin, aluminum oxide, and garnet stone in varying proportions. Furthermore, this research involves an in-depth assessment of the coating's resistance to wear and corrosion, coupled with the analysis of UV intensity signals. The ultimate goal is to establish a comprehensive database of intelligent coatings that can be applied across different industrial sectors. Additionally, the study intends to develop a predictive model for the wear and corrosion of smart coatings, utilizing machine learning techniques.

Methodology

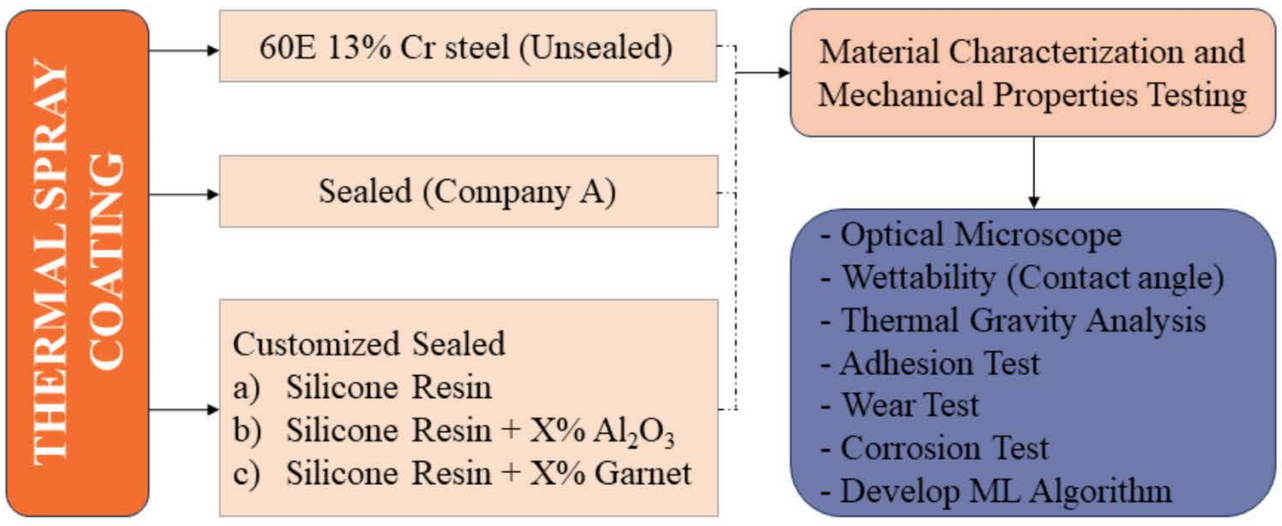

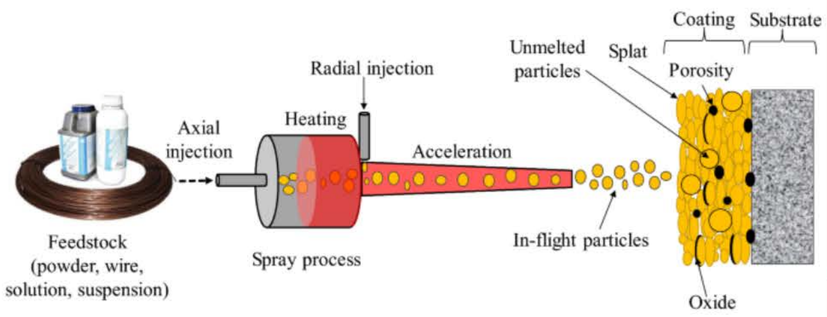

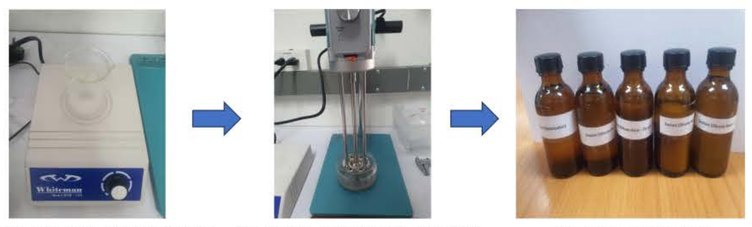

Silicone resin mixed with ethanol solvent in magnetic stirrer for 30 min at 300 rpm

The solution mixed with Al_2O_3 component in dispersing machine for 30 min at 500rpm

Prepared Silicone resin with 35wt.% Al_2O_3 Sealants

Result & Discussion

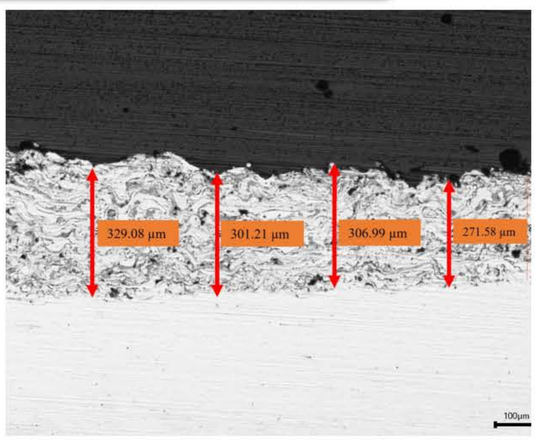

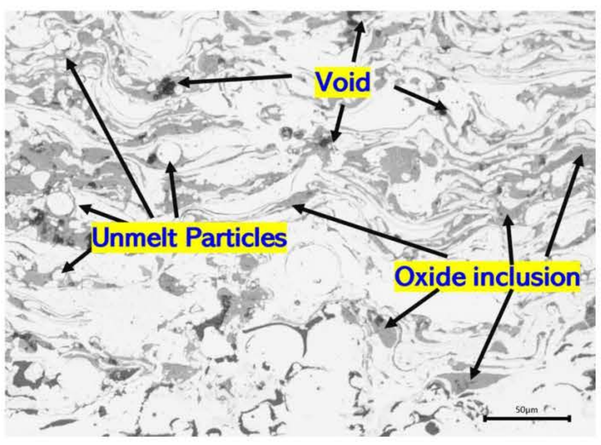

Optical micrograph of coating

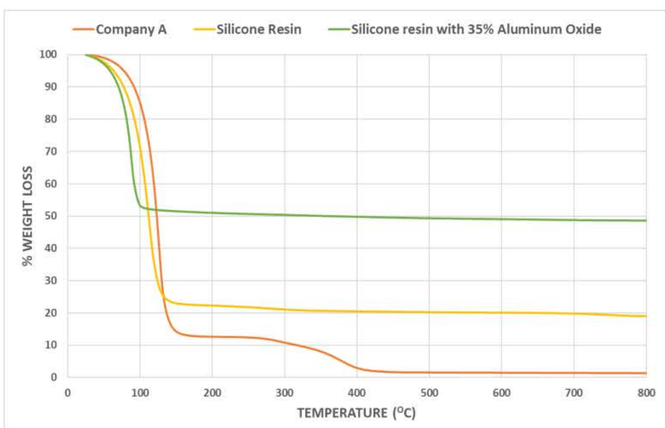

TGA results of sealants

Conclusion

Optical microscopy examination of the coating revealed an average thickness of 296 µm. The porosity was measured at 4.6% using image processing, and the average microhardness of the coating was found to be 362 $HV_{0.5}$. The TGA results demonstrated that the silicone resin with added Al_2O_3 outperformed when compared with Industry A-grade sealants.

Acknowledgment: This research has received funding support from the NSRF via the Program Management Unit for Human Resources & Institutional Development, Research and Innovation [grant number B13F660125]

BRAINPOWER CONGRESS 2023

ร่วมกันสร้างและขับเคลื่อนงานวิจัยขึ้นแนวหน้า
สู่อุตสาหกรรมแห่งอนาคต

Development of Coating using Low-Pressure Spray Machine

Pudsadee Chupong and Asst. Prof. Dr. Karuna Tuchinda*

**Material Manufacturing and Surface Engineering Research Center,
The Sirindhorn International Thai-German Graduate School of Engineering,
King Mongkut's University of Technology North Bangkok**

Statement of Problem :

The steel industry holds great importance in the country's manufacturing sector. Steel possesses crucial properties like corrosion, wear, and high-temperature resistance, making it a common material across various industries. Carbon steel, in particular, finds widespread use. Heat treatment is a preferred method for enhancing material properties. Surface treatment, a part of the heat treatment process, improves surface properties and extends the lifespan of materials. Hardening processes, like DLC coating or PVD processes using materials such as AlCrN, CrN, TiAlN, and TiN, enhance the surface properties of molds. These processes elevate tool performance in manufacturing by improving wear and corrosion resistance. While heat treatment offers numerous advantages, it also presents challenges, such as distortion due to the high temperature (usually over 700 °C), altering the material's microstructure. Issues like cracking from rapid cooling, time consumption, and limitations in material types, sizes, and shapes are noteworthy. Various alternative processes, such as thermal spray, cold spray, and shot peening, exist for improving material properties. Unlike heat treatment, these processes do not alter the microstructure. However, it's essential to note that the thermal spray process also involves high temperatures. The cold spray process becomes a favorable choice to avoid high temperatures.

The cold spray process has two types: high-pressure cold spray and low-pressure cold spray. The cold spray was a coating deposition technology that uses metal powders as feedstock material. The cold spray was a spray technique capable of producing thick metal and, in some cases, metal–ceramic coatings on metal or ceramic substrates at relatively low temperatures, preserving the initial phase composition of feedstock material. The cold spray process uses high energy or high velocity at low temperatures to make metal particle deformation. If the impact velocity exceeds a threshold value, particles endure plastic deformation and adhere to the surface of the substrate.

This research studying low-pressure cold spray and composite coating. Modify the local machine to produce a composite coating. Focusing on the nozzle can create particle velocity more than the critical velocity of the particle for composite coating with low pressure.

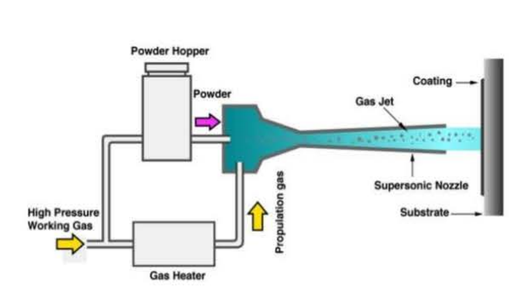

Fig 1. Schematic diagram of cold spray process [http://www.mecpl.com/cold-spray.php]

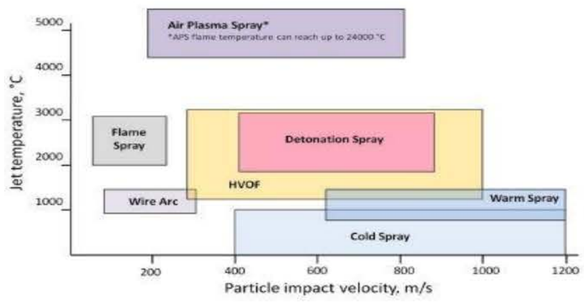

Fig 2. Classification of thermal spray processes in accordance with particle velocity and flame temperature [A.S.M. Ang et al, 2013]

Methods :

1. Study the low-pressure cold spray concept using simulation methods (Finite Element Method) and experiment with composite coating (Al/TiN) by selecting velocities from the simulation results (pressure not exceeding 1 MPa)

2. Modify the local machine to create a coating layer by constructing a spray gun with a heater and choosing a nozzle similar to the commercial design..

Results & Discussion:

The cold spray part

- Simulation results:

- Particle velocity (Vp) affects PEEQ; increasing Vp results in an increased PEEQ length (refer to Fig 3.)

- Particle temperature increases the flattening ratio and reduces the critical velocity of the particle (refer to Fig 4.)

- Choose a particle velocity of more than 400 m/s (exceeding the critical velocity) to calculate the pressure used in the experiment.

- Experimental results:

- Temperature during the process affects thickness and hardness; an increase in temperature leads to an increase in hardness (refer to Fig 5.), and thickness (refer to Fig. 6) increase.

- TiN particle embedding in Al (refer to fig 7.)

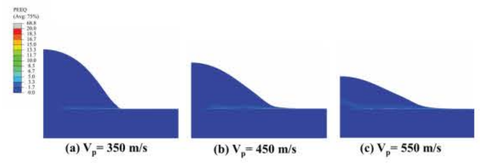

Fig 3. Simulation contour of PEEQ at 30ns of 25 µm Al particles upon an SKD11 hardening substrate at a different particle velocity (Temp 350 °C)

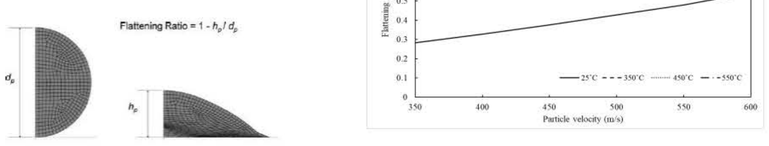

Fig 4. Relationship between the particle velocity and the flattening ratio at different temperatures.

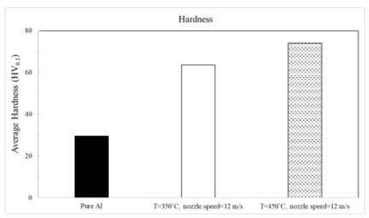

Fig 5. average hardness

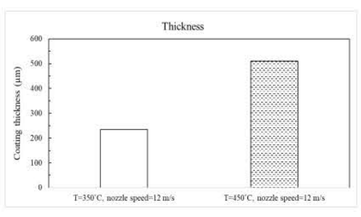

Fig 6. average thickness

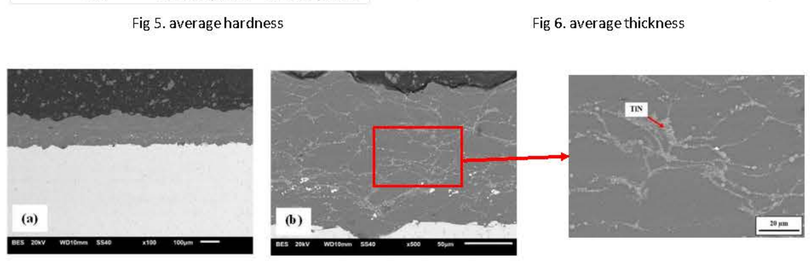

Fig 7. Back-scattered electron micrographs of Al/TiN composite coating at 350 °C

The modified machine part

The particle velocity in cold spray is influenced by the nozzle expansion ratio (i.e., the ratio of the exit area to the throat), except for particle size and density. The particle velocity increases as the nozzle exit diameter increases until the nozzle exit diameter surpasses 2.5 times the nozzle throat diameter, at which point the particle velocity decreases (Li, 2005).

In this work, the throat diameter is designed to be 2 mm, and the exit diameter is 4 mm. This design has been successfully used in the literature (Wen-Ya Li, 2007) (T. Raja Jayasingh, 2014) (refer to Fig. 9).

Some Al/TiN was found on the substrate, confirmed by the EDS results (refer to Figs. 10 - 11), but the layer was thin, with an average thickness of 3.049 µm.

Limitations: pressure 0.6 MPa, temperature input 650 °C, output 300-350 °C.

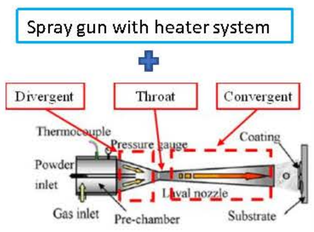

Fig 78 Schematic of cold spray nozzle.

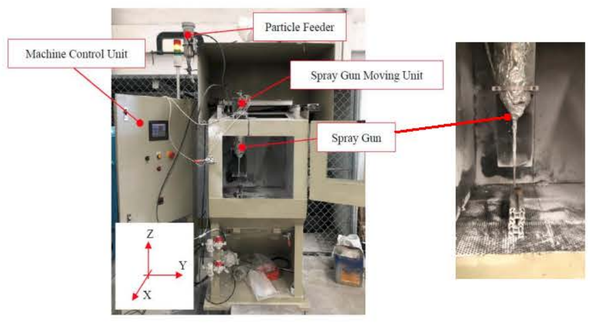

Fig 9. The developed spray machine prototype

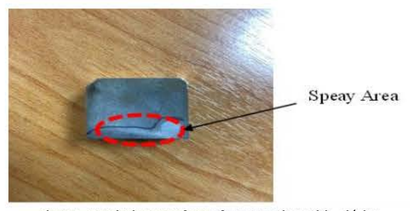

Fig 10. Workpiece surface after spraying with Al/TiN

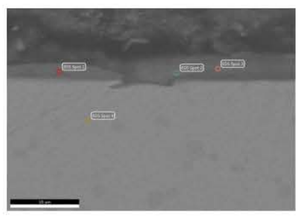

Spectrum	C	N	O	Al	Ti	Cr	Fe	Total
1	30.0	0.6	3.4	0.2	3.3	5.8	56.7	100
2	31.9-	0.6	3.7	0.2	3.3	10.3	50.0	100
3	32.8	0.7	3.8	0.1	2.9	5.3	54.3	100
4	21.8	-	-	-	-	6.1	70.8	100

Fig 11. EDS measuring positions (Al/TiN)

Conclusion:

1. Use Finite Element Method (FEM) to study characteristic particles on the substrate and predict microstructure properties based on the flattening ratio.
2. The prototype spray machine can produce a thin or non-uniform coating, but this marks a good starting point for developing the machine, particularly focusing on the nozzle part.

In the future, it will be possible to modify this machine to create a thick and even coating. This can be achieved by changing the powder feeder system and renewing the nozzle design to suit this machine.

Acknowledgments:

This research has received funding support from the NSRF via the Program Management Unit for Human Resources & Institutional Development, Research and Innovation [grant number B13F660125]

BRAINPOWER CONGRESS 2023

ร่วมกันสร้างและขับเคลื่อนงานวิจัยขึ้นแนวหน้า
สู่อุตสาหกรรมแห่งอนาคต

Development of Thermal-Based NDT Technique to Detect Defect Areas

Pongpak Lap-Arparat & Asst. Prof. Dr. Karuna Tuchinda*

Material Manufacturing and Surface Engineering Research Center,
The Sirindhorn International Thai-German Graduate School of Engineering,
King Mongkut's University of Technology North Bangkok.

Statement of Problem

Inspection is a fundamental process for assessing the condition of components within industrial systems, playing a significant role in ensuring their reliability and preventing operational failures. Nondestructive testing (NDT) techniques have been widely adopted for industrial inspection, with Ultrasonic Testing (UT) and Eddy-Current Testing (ECT) being the preferred methods due to their precision and accuracy. Both UT and ECT rely on the transmission of inspection waves through the object being examined, facilitating the detection of surface and subsurface defects. However, these methods require surface preparation and experienced inspectors, leading to time-consuming inspections and limited coverage. Reducing the inspection time is an industrial interest that is requisite to optimize the industrial operation.

Recent advancements in inspection methods have introduced thermal-based techniques, such as Infrared (IR) camera integration, to capture temperature variations in a broader range. A novel approach known as "**Vibrothermography**" (VT) emerged, combining IR cameras with ultrasonic welders as excitation sources. VT subjects the object to vibrations induced by the ultrasonic welder, and defects like cracks convert mechanical energy into heat, detected as a temperature rise by the coupled IR camera. VT promises quicker and more comprehensive defect detection, as demonstrated by Fravo et al.'s experimental study. However, the exact mechanisms behind the heating in VT remain unclear, necessitating a deeper understanding of the method for its optimal development.

This study aims to advance the practical application of Vibrothermography (VT) in industrial inspections and identify its limitations. The study endeavors to combine experimental and computational approaches to explain the behavior of inspected parts during VT inspections. This effort seeks to develop thermal-based prediction for defect detection, offering a more efficient and effective alternative to conventional inspection methods.

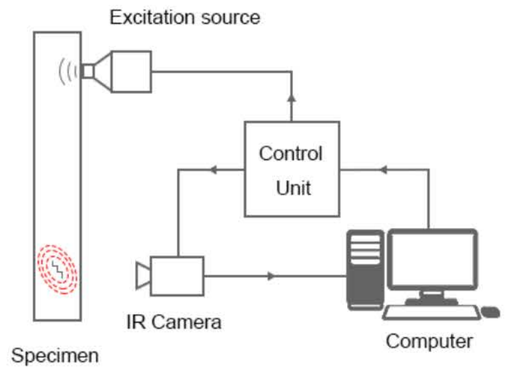

Vibrothermography inspection method

Method

For the preliminary study, the studies primarily investigated the behavior of temperature induced during structural deformation based on deformation-induced heating. The shaft material such as SCM440 steel was selected for the investigation. Two approaches were observed parallelly, the experimental-based study was conducted to investigate the relationship between the temperature and deformation strain. For the computational-based study, vibrothermography was virtually applied on the SCM440 shafts with and without a crack to investigate the strain behavior under ultrasonic excitation.

Experiment: Temperature-Strain Relationship

- Material: SCM440 Steel.
- Testing Conditions:
  - Uniaxial tensile testing with a controlled speed of 0.5 mm/min.
  - ASTM E8 standard specimens with marked inspection points.
  - Aiming temperature and deformation strain during the test.
- Equipment Used:
  1. Epsilon extensometer for gauge strain measurement.
  2. K-type thermocouples coupled with NI-9213 module for temperature measurement
  3. GOM ARAMIS DIC for localized strain measurement at marked inspection points.

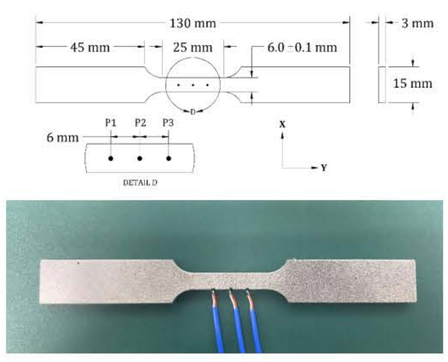

Tensile specimen

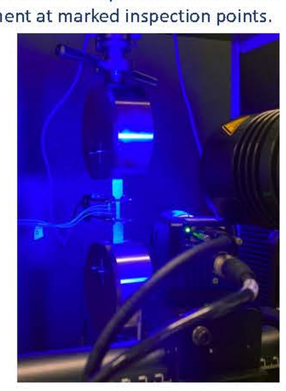

Setup

Simulation: Strain Behavior of Cracked and Uncracked Shafts under Excitation

- ABAQUS FEA: Implicit-dynamic analysis.
- Cracked and Uncracked shafts subjected to vibrate with a low-power ultrasonic transducer.
- Aiming strain distribution under excitation.
- Controlled Parameters of Semi-Elliptical Crack Geometry:
  - $\alpha = a/R = 0.05, 0.1, 0.25, 0.5, 0.75, 1.$
  - $\beta = a/c = 0, 0.25, 0.5, 0.75, 1.$
- Testing Conditions:
  - Axial excitation with cantilever support.
  - Transverse excitation with fixed ends support.

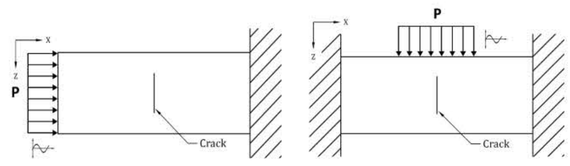

Excitation conditions

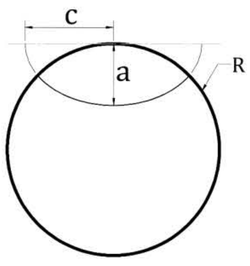

Crack controlled parameters

Results & Discussion

Experiment:

During uniaxial tensile testing, the specimen's temperature (T) continuously increased with deformation, described as:

$$T = T_0 + \Delta T \quad (1)$$

where, T_0 is initial temperature and ΔT is temperature change.

For the temperature-strain relationship, the temperature and strain values at the inspection points were collected and the means were determined. The mean temperature change was then plotted against the mean true strain, taking into consideration the state prior to necking, due to the consistency of the specimen deformation ($\varepsilon_{eq,uni}$). The polynomial curve fitting exhibits a strong fit with R^2 = 0.9985 and can be expressed as follows,

$$\Delta T = -86.515\varepsilon_{eq,uni}^2 + 26.437\varepsilon_{eq,uni} - 0.0758 \quad (2)$$

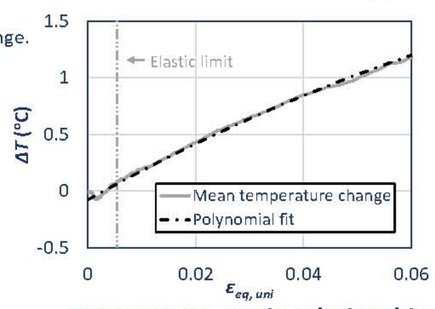

Temperature-strain relationship

Prediction of temperature based on the temperature-strain relationship

- Temperature prediction under similar conditions of uniaxial tensile testing.
- Considering temperature induced in gauge section prior to necking.
- Equipment Used:
  1. Epsilon extensometer for gauge strain measurement.
  2. FLIR a655sc IR camera for temperature measurement.
- Strain alterations were obtained from both experiment and Finite Element Method (FEM)
- Strains were sequentially substituted into Eq. (2) and Eq. (1) for predicted temperatures.
- Temperature gradient and the computational strain distribution reveal a comparable color contour.
- Estimation Accuracy:
  - Good estimation with a maximum absolute error of approximately 0.4 °C

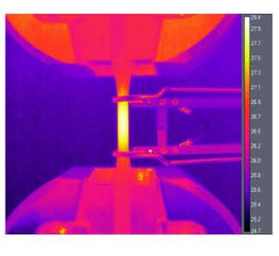

IR camera

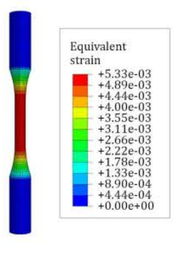

FEM

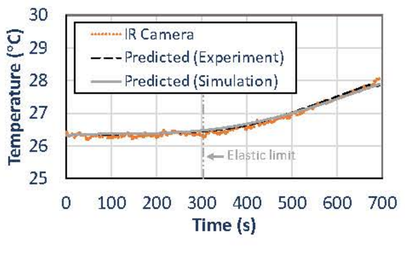

Temperature prediction

Simulation:

- Computational results revealed strain distribution change over time.
- Uncracked shaft:
  - Exhibited low strain corresponding to excitation, with a maximum of 3.89×10^{-9} and 4.72×10^{-9} for axial and transverse excitation.
- Cracked Shaft:
  - Displayed significantly higher strain, concentrated around the crack tip.
- Consider the first peak, the strain close to the crack tip was normalized with the maximum strain of the uncracked shaft.
- Influence of Crack Geometry:
  - Higher α = Higher strain.
  - Higher β = Higher strain.

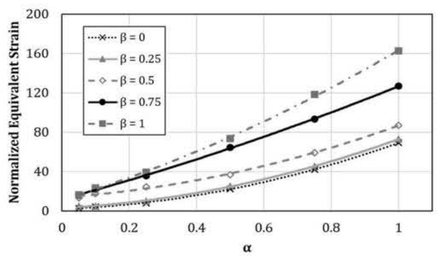

Axial excitation

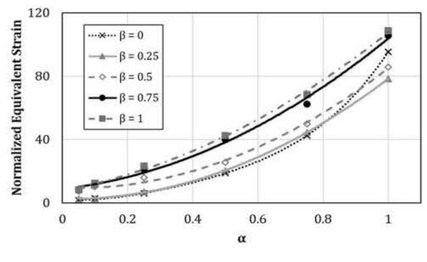

Transverse excitation

Experimental investigation of the shaft response.

- The shaft response under the excitation was investigated experimentally, for instance, transverse excitation of the uncracked shaft.
- Equipment Used:
  1. Designed jig and fixture.
  2. Low-power ultrasonic transducer.
  3. GOM ARAMIS DIC.
- Consider the magnitude of displacement due to the extremely low strain distribution.
- Normalized deformation magnitudes from experiment and simulation at steady-state revealed a good agreement of the computational model beyond the angular displacement of $\frac{\pi}{4}$ with a percentage error of less than 5%.
- Temperature prediction was additionally applied, revealing extremely low temperature differences which were 1.03×10^{-7} °C for axial excitation and 1.25×10^{-7} °C for transverse excitation.

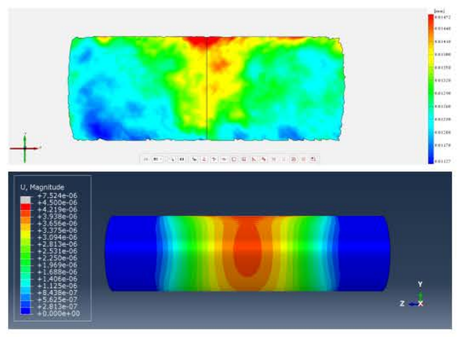

Contour of deformation magnitude

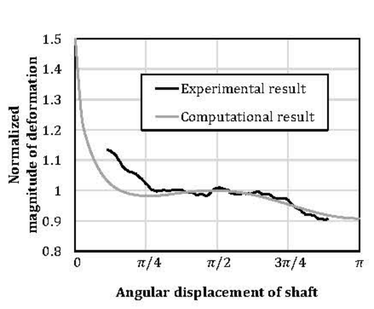

Comparison of normalized deformation magnitude

Temperature prediction on the cracked shaft.

- The relationship was utilized to estimate the temperature of the cracked shaft with β = 1, α = 1 under excitations which found as the highest strain generation.
- The maximum temperature differences were 1.67×10^{-5} °C and 1.46×10^{-5} °C for axial and transverse excitation which much lower the thermal sensitivity of the IR camera (0.03 °C).
- Emphasizing the insufficient of the current excitation source for practical use.
- The maximum temperature differences were significantly higher compared to the uncracked shaft, indicating the possibility of crack detection under sufficient excitation.

Acknowledgements

This research has received funding support from the NSRF via the Program Management Unit for Human Resources & Institutional Development, Research and Innovation [grant number B13F660125].

Conclusion

- Under uniaxial tensile testing, the temperature increases corresponding to the strain of the tensile specimens.
- The deformation temperature can be estimated effectively when the corresponding strain alteration is known.
- The developed temperature prediction technique has the potential to be effective when utilized with a high-sensitivity IR camera and sufficient power of excitation source.
- The results suggest that the temperature prediction technique can effectively estimate defective areas due to the strain distribution around a crack.

BRAINPOWER CONGRESS 2023

ร่วมกันสร้างและขับเคลื่อนงานวิจัยขั้นแนวหน้า
สู่อุตสาหกรรมแห่งอนาคต

Lifetime Improvement of Capillary used in Laser Solder Ball Jetting Process

Suparoj Premjarunan[*,a], **Asst. Prof. Dr. Karuna Tuchinda**[*,b]
*Material Manufacturing and Surface Engineering Research Center,
The Sirindhorn International Thai-German Graduate School of Engineering,
King Mongkut's University of Technology North Bangkok
[a] Author
[b] Corresponding Author, Principal Investigator

INVENTION TO INNOVATION

Problem statement

Laser Solder Ball Jetting Process is Fluxless Laser Soldering method which is possible to perform laser fluxless reflow soldering of solder discs on pre-tinned Cu pads. The new method of laser-based solder jetting technology, Solder Ball Bumper Jet (SB^2-Jet), have been developed by Pac Tech-Packaging Technologies GmbH of Germany and Pac Tech USA. This method providing throughput of soldering at the rate of 10 balls/s which can fulfills most of requirements for today's packaging of optoelectronics. Laser Solder Ball Jetting Process have numbers of benefit, such as high throughput and high accuracy even in miniature device. However, high throughput of process can cause the failure of capillary material (cemented carbide is the most common material used) in short time and have to be changed with new capillary which can create downtime in manufacturing. Downtime from capillary changing time should be added into the process schedule which can reduce the output of the production and more cost of capillary tip would be added into capital cost.

To improve the material used for capillary, it was studied that improvement WC-Co with cryogenic treatment result in smaller wear volume expected compared to untreated WC-Co.

This study aims to improve mechanical properties of capillary using cryogenic treatment which could lead to lifetime improvement and reduce the manufacturing cost. Several possible failure modes associated to lifetime of capillary tip which is the critical area controlling process accuracy of Laser Solder Ball Jetting machine were investigated, such as, thermal expansion, erosion wear associated with fluid jet and particle impact. However, thermal expansion of WC-Co was very low at soldering temperature and generated limited stress compared to hard particle impingement. Therefore, the study focused on mechanical properties associated with fatigue life.

Method

Commercial grade of WC-Co, i.e., KA10 according to Sanalloy Industry Co., Ltd. was used in this study to represent capillary material. Mechanical properties characterization were employed to investigate the properties of WC-Co before treatment, i.e., hardness testing, sliding wear testing and nanoindentation testing.

After WC-Co testing, the material was cryogenic treated under different cryogenic conditions, i.e., holding time at cryogenic temperature, and cryogenic temperature. Cryogenic temperature was divided into 2 different conditions, i.e., shallow cryogenic treatment (SCT) and deep cryogenic treatment (DCT) (-140 and -200 degrees Celsius, respectively). Holding time divided into 2 conditions, i.e., 12 and 36 hours. Samples after treatment were then be tested by the same method before treatment for comparison and study the effect of cryogenic treatment. Condition of each samples shown in Table 1.

Table 1. Cryogenic treatment condition for each sample

Sample	Cryogenic Temperature (°C)	Holding time (hours)	Cooling rate (°C/min)
NCT	-	-	-
SCT12	-140	12	1
SCT36	-140	36	1
DCT12	-200	12	1
DCT36	-200	36	1

Result and Discussion

The result shown that holding time of 36 hours exhibit higher hardness and lower wear volume compared to holding time of 12 hours. Lower cryogenic temperature led to higher hardness and lower wear volume as shown in Figure 1 and 2 for hardness and wear volume, respectively.

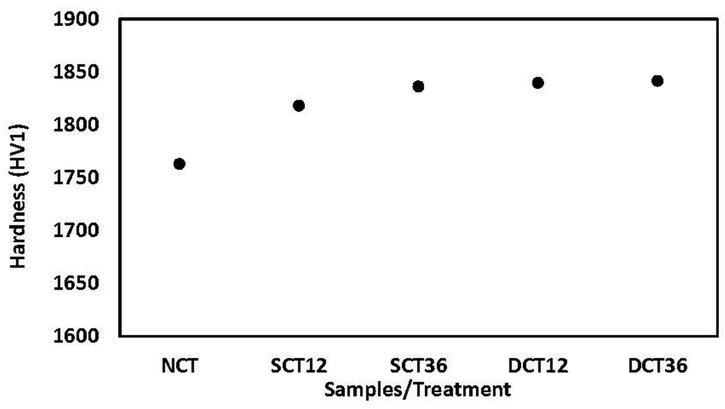

Figure 1. Hardness from different case of cryogenic treatment

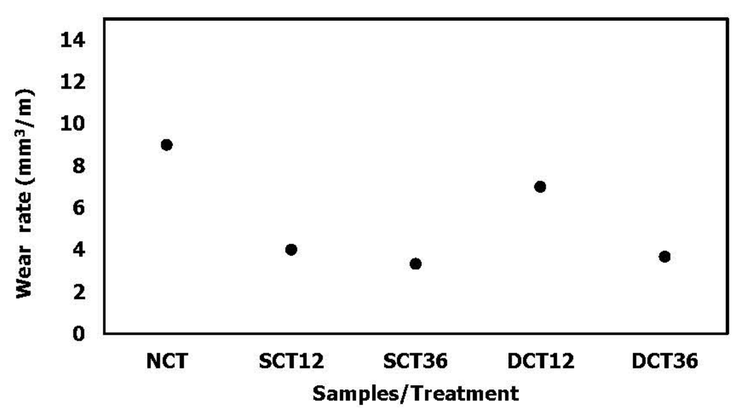

Figure 2. Wear volume from sliding wear testing of different case of cryogenic treatment

Moreover, result of nanoindentation can be used to calculate Young's Modulus. The result shown that WC-Co after cryogenic treatment exhibit higher Young's Modulus and lower deviation as shown in Figure 3. Young's Modulus of DCT is highest followed by SCT and NCT respectively. In case of deviation of Young's Modulus result, NCT showed highest deviation followed by SCT and DCT showed lowest deviation. The deviation of Young's Modulus indicate that mechanical properties showed better distribution after cryogenic treatment. The same trend also applied to nanohardness. The nanohardness from nanoindentation testing result also showed that cryogenic treatment improve hardness and reduce their deviation in nanoscale as shown in Figure 4.

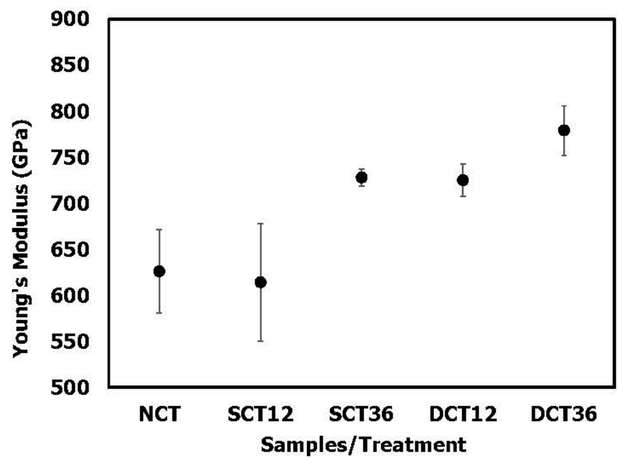

Figure 3. Young's Modulus from each case (Calculated from Reduced Modulus from nanoindentation testing)

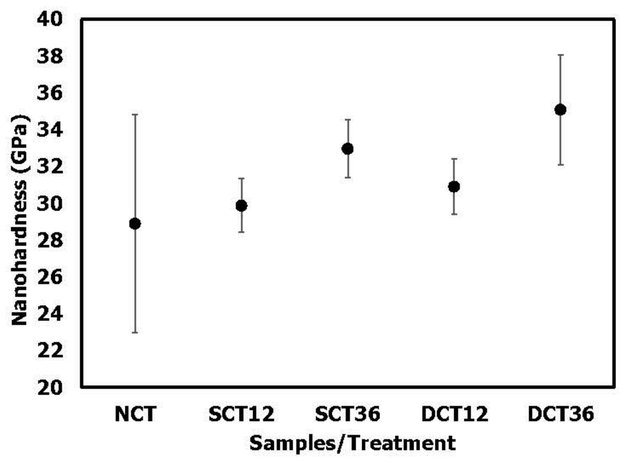

Figure 4. Nanohardness from each case

Conclusion

Longer holding time and lower cryogenic temperature led to higher hardness and lower wear volume which could lead to higher fatigue strength and longer lifetime.

The result from nanoindentation testing shown that DCT showed highest Young's Modulus followed by SCT and NCT respectively. Cryogenic treatment also improves the distribution of microstructure as shown in lower distribution range after cryogenic treatment (SCT, DCT).

Therefore, Cryogenic treatment of cemented carbide material improve mechanical properties and more homogeneous.

However, more study should be done to investigate the effect of cryogenic treatment to capillary material properties in more detail, such as, cooling rate effect on mechanical properties or the effect of cryogenic treatment on microstructure and residue stress

Acknowledgements

This research has received funding support from the NSRF via the Program Management Unit for Human Resources & Institutional Development, Research and Innovation [grant number B13F660125]

BRAINPOWER CONGRESS 2023

ร่วมกันสร้างและขับเคลื่อนงานวิจัยขึ้นแนวหน้า
สู่อุตสาหกรรมแห่งอนาคต

Rheological analysis for single-use package manufacturing from thermoplastic starch

Yaowaret Maiket[1], Rungsima Yeetsorn[2], Karuna Tuchinda[2], Jatesuda Jirawutthiwongchai[3]

[1] King Mongkut's University of Technology North Bangkok, Bangkok 10800, Thailand

[2] The Sirindhorn International Thai-German Graduate School of Engineering, King Mongkut's University of Technology North Bangkok, Bangkok 10800, Thailand

[3] Siam Modified Starch Co.,Ltd. Pathum Thani- Lat Lum Kaeo Road, Koo Bang Luang, Lat Lum Kaeo, Pathum Thani 12140 Thailand

Objectives

- To analyze the fluid flow behavior and guide the adjustment of molding process conditions for TPS and TPS blend.
- To analyze the relationship between thermoplastic flow behavior data and the design of formulas involving different compositions of TPS and TPS blend.
- To analyze the relationship between thermoplastic flow behavior data and the properties of various products made from TPS and TPS blend.

Scope of work

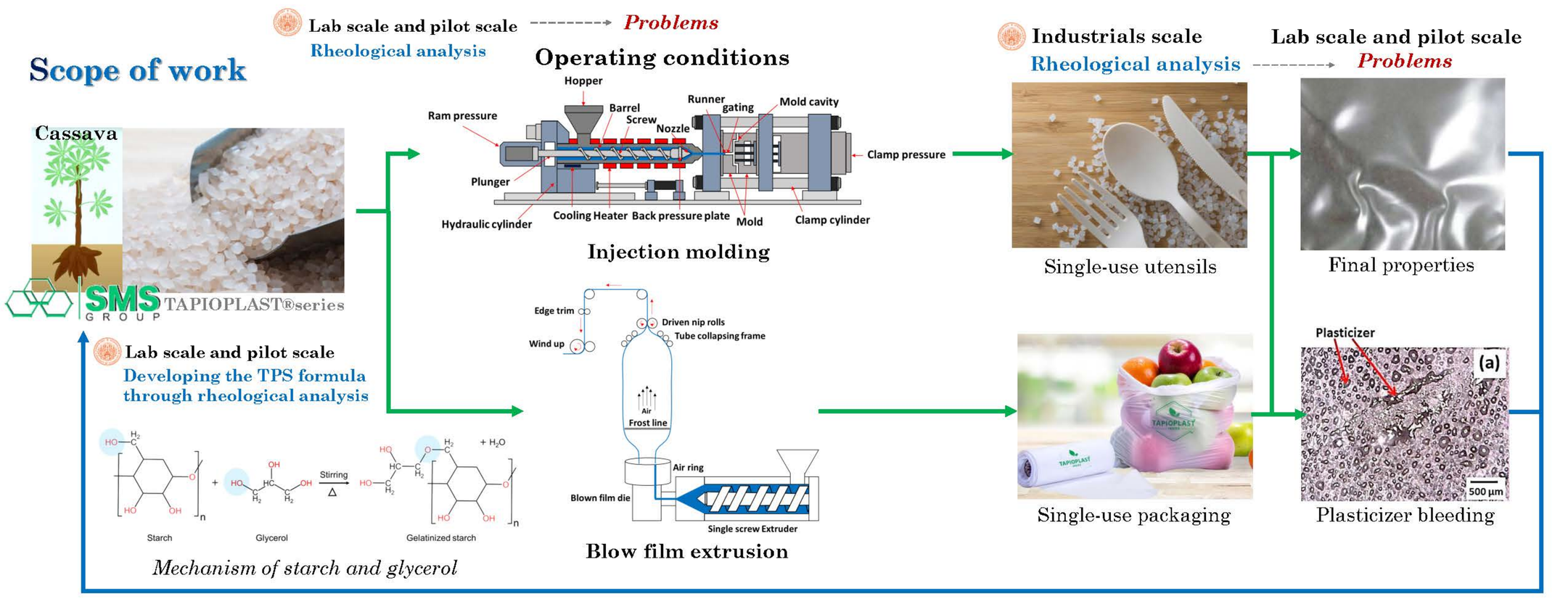

Results and discussion

Sample preparation (10 Samples)

LDPE, LLDPE, HDPE, PLA, PBAT, CG41-D, CS25, CM30, TPS FC, TAPIOPLAST®

Materials characterization
Physical properties
• Density and bulk density
• Hardness
• Tribological test
Thermal properties
• Differential scanning calorimeter (DSC)
Mechanical properties
• Tensile test (Static and dynamic modes)
• Drop weight testing
Permeabilities
• Oxygen permeation analysis (OTR)
• Water vapor permeation analysis (WVTR)

Injection molding machine;

- Understanding machine

Machine: Injection molding
Country: Taiwan
Model: EN-30
Machine system: Hydraulic pump

Part fix on mold after mold open

Part after de-molding

Clamping unit	Value
Clamp force	30 Ton (Max)
Clamping system	Hydraulic direct clamp
Tie bar distance	260 x 260 mm
Plate distance	400 x 400 mm
Mold open stoke	N/A
Minimum mold thickness	200 mm
Ejector stoke	N/A
Locating ring (diameter)	60 mm

Injection unit	Value
Screw diameter	22 mm
Screw L/D	30
Screw stoke	80 mm (Max)
Injection pressure	N/A
Injection speed	N/A
Nozzle radian	N/A

Rotational rheometer testing; - Finding condition

Tempera-ture (°C)	Pre-heating time 0 min	5 min	10 min	15 min	20 min	30 min
170						N/A
180						
190						
200						N/A
210				N/A	NA	N/A

Examine the characteristics of the polymer melt under varying pre-heating times at different testing temperatures for TAPIOPLAST CS25.

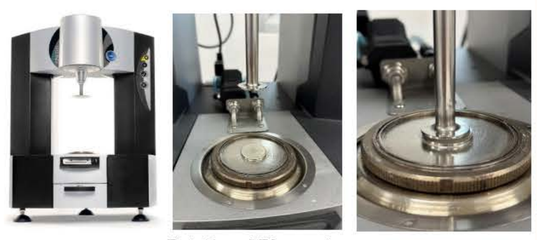

Rotational Rheometer

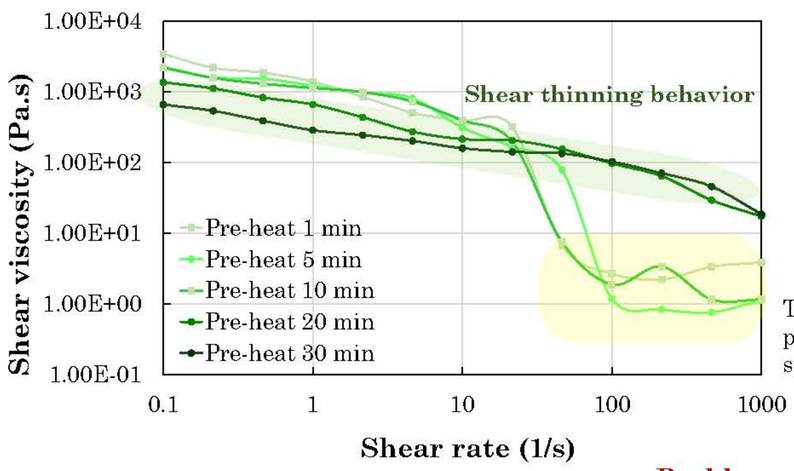

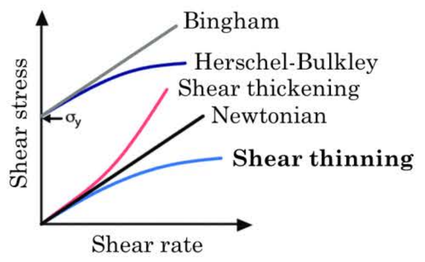

The pre-heating times for TAPIOPLAST CS25 polymer at 190°C before conducting a shear sweep test using a rotational rheometer.

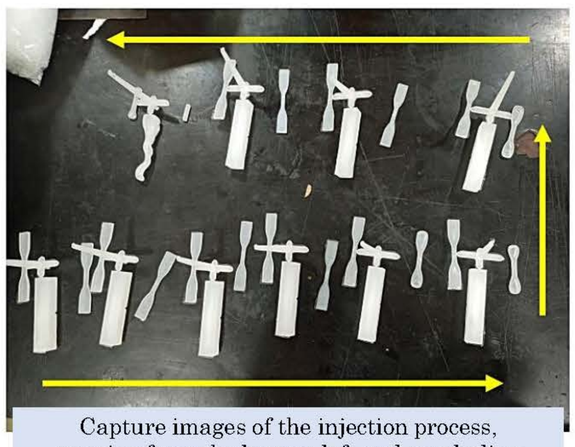

Capture images of the injection process, starting from the bottom left and concluding at the upper left.

Problems

1. During continuous processing, the system demonstrates instability, resulting in short shots and an increased occurrence of sink marks.
2. Operators consistently adjust parameters to maintain stability.
3. The identified cause of the problem is a material leak at the nozzle, leading to material loss with each shot. This necessitates frequent adjustments by the operator for every shot.

Material leakage

Part short shot

Conclusions

1. Obtain the physical, thermal, mechanical, and permeability properties of the sample.
2. Assess the conditions of the rotational rheometer.
3. Identify issues with the injection molding machine.

Current Outputs

1. The data presents a flow behavior of TPS and TPS blends were tested using the rheometer 1 copy/sample.
2. The data presents a detailed analysis of the relationship between the flow behavior of TPS and TPS blends and the properties of the final product 1 copy/sample.

Acknowledgement

This research has received funding support from the NSRF via the Program Management Unit for Human Resources & Institutional Development, Research and Innovation [grant number B13F660125].

BRAINPOWER CONGRESS 2023

ร่วมกันสร้างและขับเคลื่อนงานวิจัยขั้นแนวหน้า
สู่อุตสาหกรรมแห่งอนาคต

Development of Frontier Researchers in Nanomaterials for Supporting Industrial Research Problems

:: Improving the performance of thermoelectric materials by adding acetylene black nanocomposites

Dulyawich Palaporn[1], Supree Pinitsoontorn[1,2,*]

[1]*Department of Physics, Faculty of Science, Khon Kaen University, Khon Kaen 40002, Thailand.*

[2]*Institute of Nanomaterials Research and Innovation for Energy (IN-RIE), Khon Kaen University, Khon Kaen, 40002, Thailand.*

*Corresponding author's email address: psupree@kku.ac.th

Introduction

Acetylene carbon black (ACB)

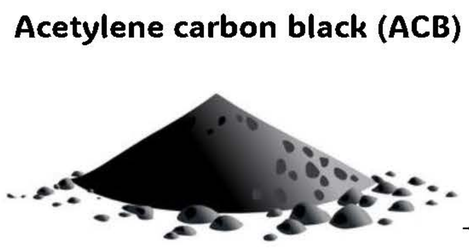

Petroleum industry

- Small particle size
- High surface area
- Chemical Stability
- Conductive properties

Composite

Thermoelectric material

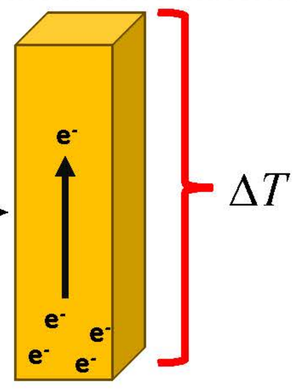

- Reduce carrier concentration
- Increase Seebeck coefficient
- Suppress thermal conductivity

The performance of conversion can be determined by dimensionless figure of merit (*zT*) as shown in EQ(1).

Seebeck coefficient — Electrical conductivity

$$zT = \frac{S^2\sigma}{\kappa}T \quad (1)$$

Thermal conductivity — Absolute temperature

Experiment

Acetylene carbon black (ACB)

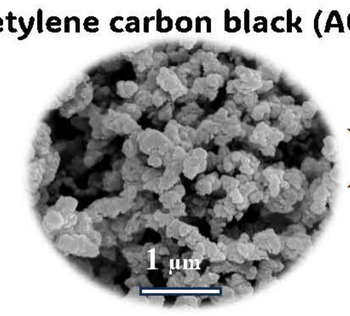

2 $AgNO_3$ Powder

Ag_2Se composite Powder

1. ACBs have been dispersed in deionized (DI) water and Ethylene Glycol (EG) in ultrasonic bath.
2. $AgNO_3$ Powder was added and dissolved in the mixed solution.
3. The Na_2SeSO_3 solution was poured into the mixed solution to be reducing agent.
4. The final powder was gathered and rinsed several times by DI water and ethanol.

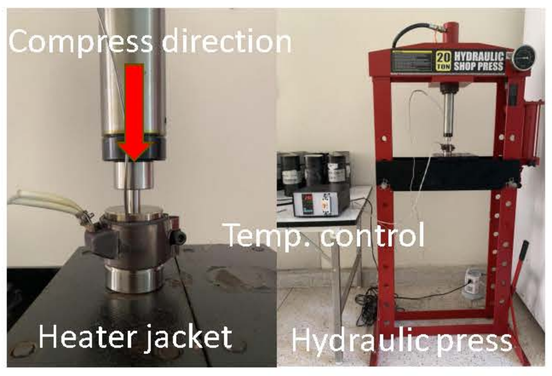

5. Ag_2Se powder was warm-pressed
   - at 523 K
   - 30 minutes
   - 600 MPa at
   - environmental atmosphere

Result and discussion

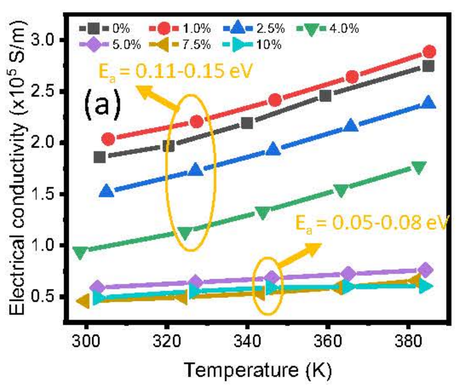

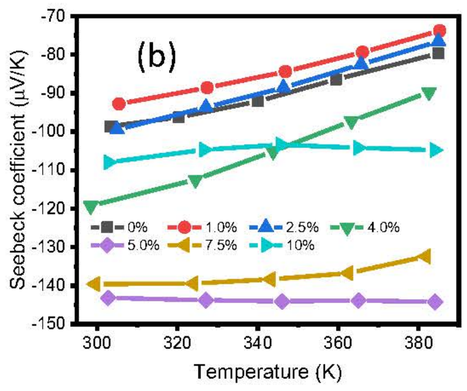

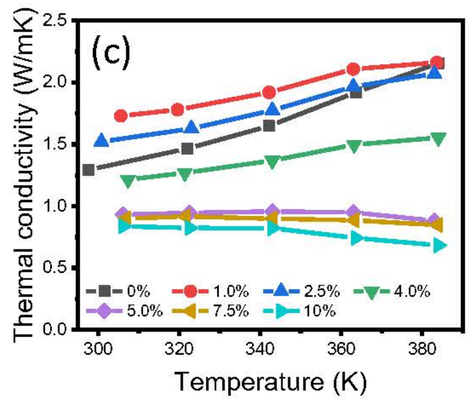

- Electrical conductivity decrease when the ACB content exceeds 1.0 wt.%, from 1.8 to 0.5 x 10^5 S/m.
- Seebeck coefficient increase from -100 μV/K to -150 μV/K for 5.0 wt.% sample.
- Negative values of the Seebeck coefficient the decrease with temperature confirm the n-type semiconductor-like behavior.

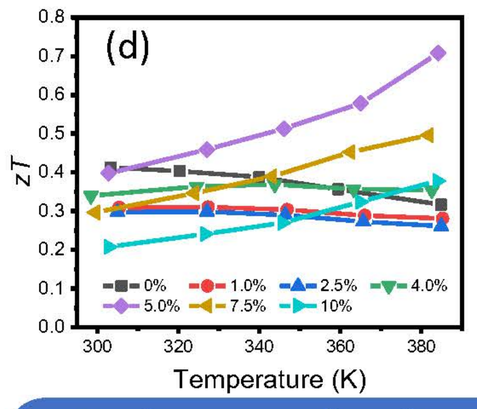

- The filling out of ACB composites in the pores support phonon transportation. Increase in lattice thermal conductivity and total thermal conductivity in 1.0 and 2.5 wt.% samples.
- Electronic thermal conductivity become more effective than lattice thermal conductivity after ACBs are added more than 4.0 wt.% and decrease to 0.9 W/mK after 5.0 wt.% sample.
- At room temperature, the *zT* of pristine and 5.0 wt.% sample can not distinguish.
- At higher temperature, the *zT* of 5.0 wt.% sample exhibits higher and reaches the highest of 0.75 at 383 K.

Conclusion

- The addition of ACB can fill out the pores and It contributes to decrease in carrier concentration.
- It can suppress thermal conductivity to lower than 1.0 W/mK when the ACBs are composited higher than 5.0 wt.%.
- The *zT* of 0.75 at 383 K is obtained for 5.0 wt.% sample.

Acknowledgement

This research has received funding support from the NSRF via the Program Management Unit for Human Resources & Institutional Development, Research and Innovation [grant number B13F6600126]

BRAINPOWER CONGRESS 2023

ร่วมกันสร้างและขับเคลื่อนงานวิจัยขั้นแนวหน้า
สู่อุตสาหกรรมแห่งอนาคต

Enhancing Electrical and Mechanical Properties of Acetylene Carbon Black/Cement Paste Composites

Development of Frontier Researchers in Nanomaterials for Supporting Industrial Research Problems

Nattapong Chuewangkam[a,b], Tarabordin Yurata[c], Supree Pinitsoontorn[a,b*]

[a] Department of Physics, Faculty of Science, Khon Kaen University, Khon Kaen 40002, Thailand
[b] Institute of Nanomaterials Research and Innovation for Energy (IN-RIE), Khon Kaen University, Khon Kaen 40002, Thailand
[c] IRPC Public Company Limited, Rayong 21000, Thailand
* Corresponding author: psupree@kku.ac.th

Introduction

Acetylene Carbon Black (ACB) particles are a carbon product obtained through the thermal decomposition process of acetylene gas. They have high mechanical properties and friction resistance. ACB also exhibits favorable electrical properties, leading to numerous studies that explore its combination with other materials to develop electrically conductive materials. This suggests that ACB has the potential for further advancements, contributing value to various products. Therefore, this project anticipates the advancement of these materials, paving the way for innovative breakthroughs.

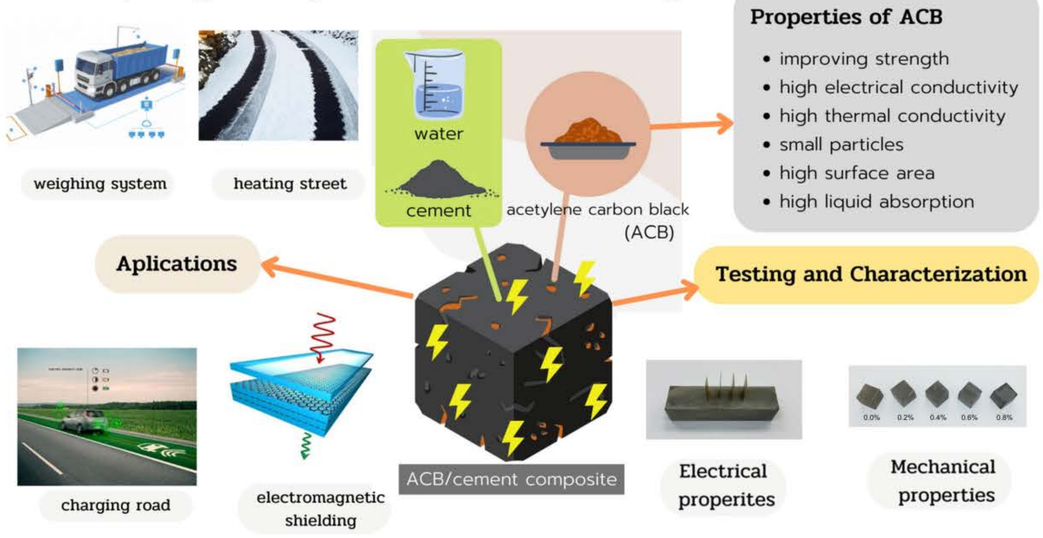

Experimental

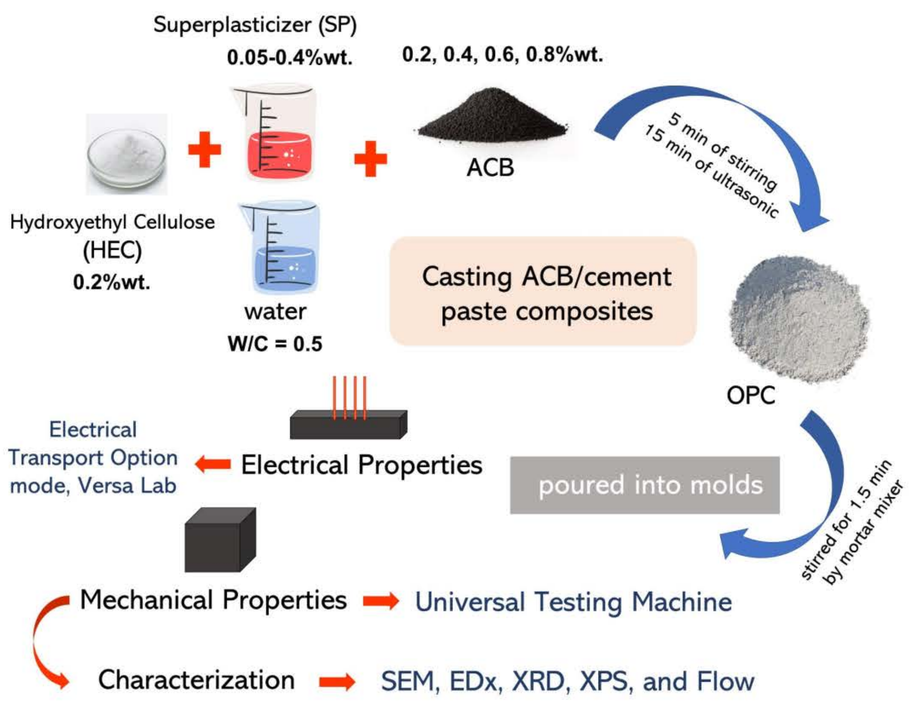

Conclusion

- ACB shows favorable electrical properties, driving research into its combination with other materials for electrically conductive materials, suggesting potential advancements.
- ACB's addition lowers electrical resistivity due to its very low resistance, acting as a bridge for efficient electron flow in the cement paste.
- Compressive strength declined with 0.4%wt. ACB at 7 and 14 days, attributed to reduced cement per unit. No impact on strength was observed after 28 days, indicating ACB's integration within the microstructure and its ability to maintain strength.

Results & Discussion

Optimize Admixture for Casting

ACB raw

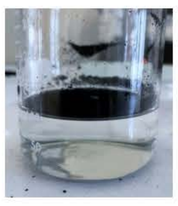

effect of hydrophobic

- At the outset, the challenge lies in the hydrophobic nature of casting ACB/cement samples, causing uneven distribution within the specimen.
- Optimal conditions involve the utilization of 0.2% weight of HEC and 0.05-0.4% weight of SP, resulting in a smooth flow and easy casting in a mold.

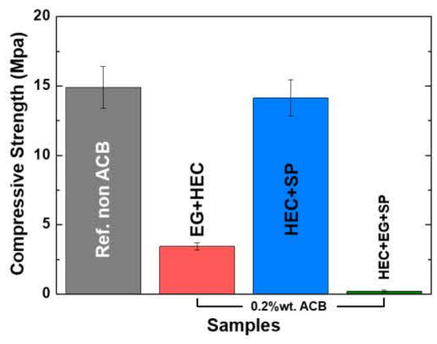

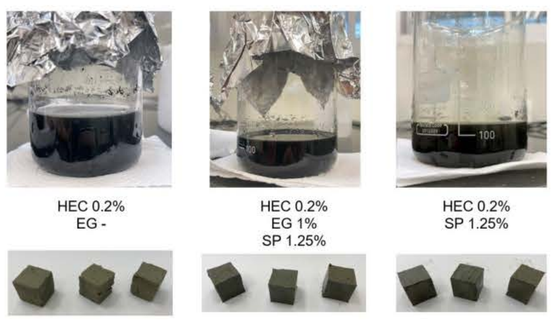

Electrical Properties

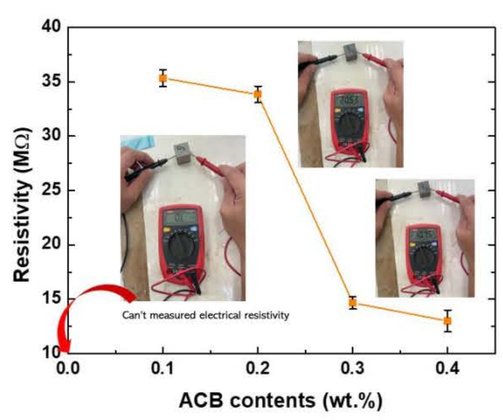

- The measurement using a multimeter and a more detailed measurement conducted with ETO mode (Versa Lab).
- The electrical resistivity decreases as more ACB is added. This happens because ACB has a very low resistance (1.6×10^{-3} kΩ•mm), allowing for highly efficient electrical conductivity in the cement paste.

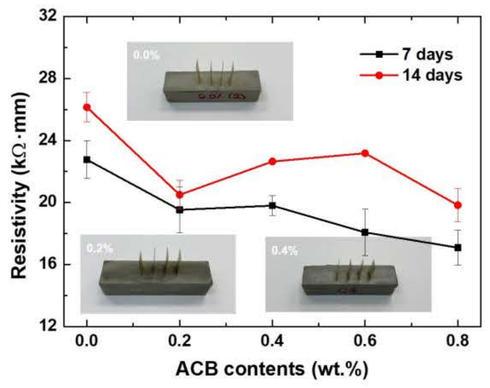

- For the curing time of cement, the electrical resistance goes up due to the reaction between cement and water forming an aluminosilicate phase. Which has higher resistance.

Mechanical Properties

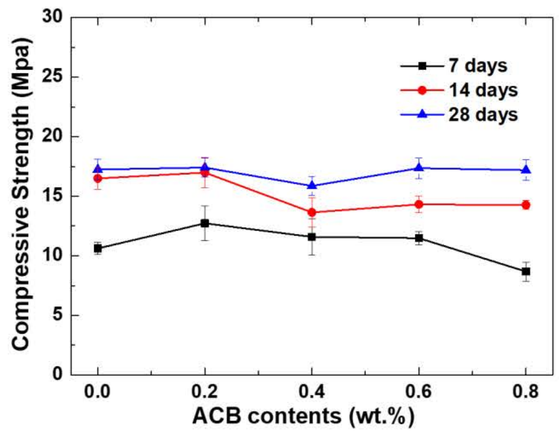

- The curing periods of 7 and 14 days, adding more 0.4%wt. of ACB resulted in a decline in compressive strength. This was due to a low amount of the binder.
- However, for the 28 days curing period, the addition of ACB had no impact on compressive strength due to a complete cement reaction. ACB embeds itself within the microstructure's pores

Acknowledgements

This research has received funding support from the NSRF via the Program Management Unit for Human Resources & Institutional Development, Research and Innovation [grant number B13F660126]

BRAINPOWER CONGRESS 2023

ร่วมกันสร้างและขับเคลื่อนงานวิจัยขั้นแนวหน้า
สู่อุตสาหกรรมแห่งอนาคต

"Development of Frontier Researchers in Nanomaterials for Supporting Industrial Research Problems"

Development of Natural Rubber Nanocomposites as an Air Filter for CO_2 Capture & Energy Harvesting

Postdoctoral Researcher : Dr. Teerayut Prada
Principle Investigator : Assoc. Prof. Viyada Harnchana
Project Leader : Prof. Supree Pinitsoontorn
Affiliation : Department of Physics, Khon Kaen University

Introduction

Global warming has become an increasingly critical global issue, largely due to the presence of greenhouse gases, with carbon dioxide (CO2) emerging as one of the main causes. These emissions are primarily generated by the burning of fossil fuels and a variety of industrial activities, including manufacturing, mining and construction, drawing attention to the urgent need for comprehensive solutions. Carbon capture and storage (CCS) technology is a promising way to reduce greenhouse gas emissions and mitigate the effects of climate change. However, conventional CCS techniques such as absorption, membrane separation and cryogenic processes face significant challenges, including cost effectiveness, energy efficiency and overall performance. In response to these issues, this study presents an air filtration system based on a triboelectric nanogenerator (TENG-based air filtration system) (Fig. 1) specifically designed for particulate matter and CO_2 capture.

Figure 1. TENG-based air filter for CO_2 capture.

The TENG-based air filtration system consists of two parts, one of which is made of porous natural rubber with adsorbent materials for filtration and the other of a triboelectric material. The phenomenon of triboelectrification on a TENG part creates an electric field that attracts and easily traps CO_2 molecules on the filter, as shown in Fig. 2. In addition, the porous structure of the natural rubber (NR) foam layer, which carries carbon adsorbents such as activated carbon and mesoporous silica, effectively improves CO_2 capture efficiency. The TENG-based air filtration system offers significant potential as a cost-effective and highly efficient air filter for CO_2 capture.

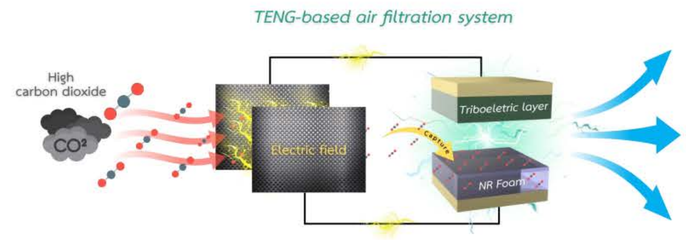

Figure 2. The structure and operation of TENG-based air filtration system for CO_2 capture.

Methods

The production of the natural rubber foam filter (NR-foam filter) begins with the mixture of natural latex with adsorbent materials, such as activated carbon (AC). This mixture is processed for 1 minute with a foam generator to ensure compatibility. The NR foam solution is then poured as a thin layer onto a glass surface. The foam solution was then heated overnight at 60 °C, resulting in a robust and effective air filter for a TENG-based air filtration system (see Fig. 3).

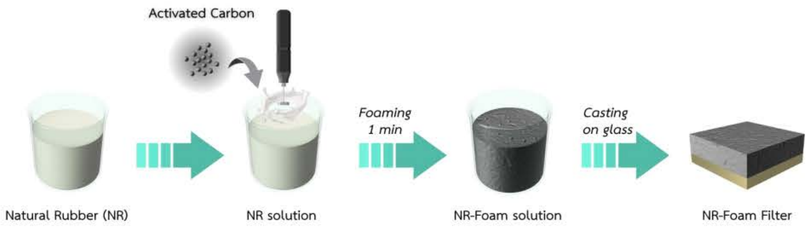

Figure 3. Preparation procedure of NR-Foam filter for TENG-based air filtration system.

Fig. 4 shows a schematic representation of the experimental setup for the evaluation of CO_2 adsorption. To remove any physically or chemically adsorbed CO_2 in the sorbent materials, the filter was treated overnight at 60 °C and the chamber was purged with N2 gas to remove any remaining residue. The CO_2 and N_2 gasses were then premixed in the gas mixer chamber before being sent to the gas inlet analyzer positioned upstream of the filter. CO_2 adsorption was studied using CO_2 analyzers based on the measurement of the difference between the total CO_2 detected at the inlet and the CO_2 detected at the outlet.

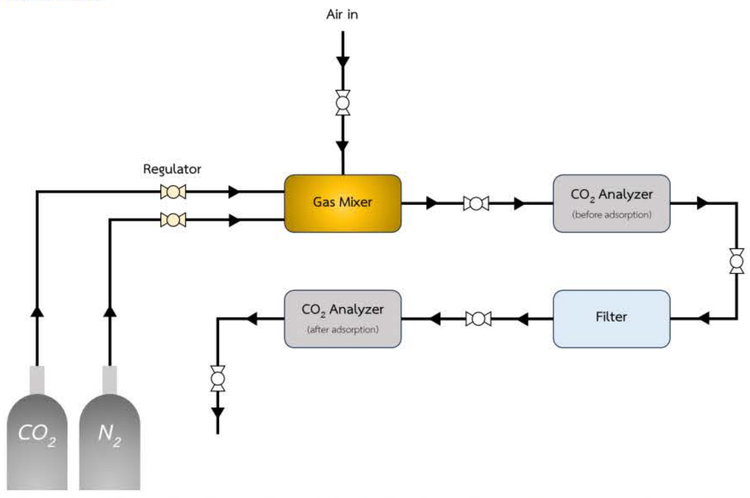

Figure 4. Schematic illustration of the CO_2 adsorption setup used in this study.

Results & Discussion

To develop air filters from natural rubber foam, it was found that the use of natural rubber latex subjected to the foaming process to produce a film resulted in a surface with more pores and roughness than using normal natural rubber latex to produce a film. This is because the foaming process creates a network of tiny air pockets in the rubber, which increase the surface area and make the material more porous. The rough surface of the foam rubber is also beneficial for air filtration, as it provides a larger surface area for particles to adhere to. When activated carbon, an absorbent material, was mixed into the foam rubber, the activated carbon was able to distribute itself evenly in the material and on the surface. The even distribution of the activated carbon in the NR foam is important for effective air filtration as it ensures that the particles are evenly distributed throughout the material.

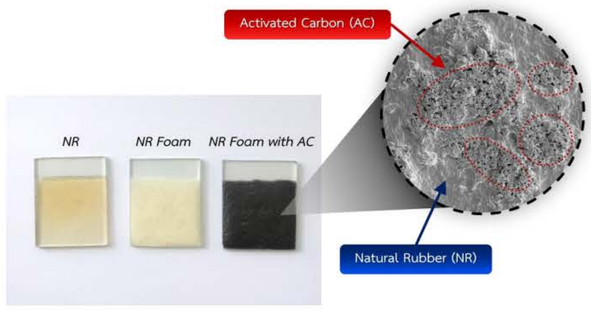

Figure 5. Photographs of NR film, NR foam and NR foam with activated carbon as an adsorption material.

The triboelectric effect is a process in which two materials that come into contact or rub against each other become electrically charged. This is because the materials have a different affinity for electrons. The material that tends to lose electrons becomes negatively charged, while the material that tends to gain electrons becomes positively charged. NR foam filters were tested for their ability to generate electricity through the triboelectric effect by testing them in combination with Teflon or polytetrafluoroethylene (PTFE), which has a higher affinity for electrons than rubber. When the two materials were brought into contact, they exchanged charges, resulting in a voltage difference across their surfaces. The voltage difference induced a current in a conductive aluminum (Al) electrode which was connected to both materials via a load, as shown in Fig. 6. The voltage generated by the NR-foam filter mixed with AC was approximately 90 V, which was twice the voltage generated by an ordinary natural rubber film. The electricity generated by the NR foam filter can be used to generate an electric field to improve the efficiency of CO_2 capture. These results suggest that NR-foam filters have the potential to be used as a new type of CO_2 capture material. The filters are relatively inexpensive to produce and have a high efficiency in generating electricity. The electricity generated can be used to create an electric field to improve the efficiency of CO_2 capture.

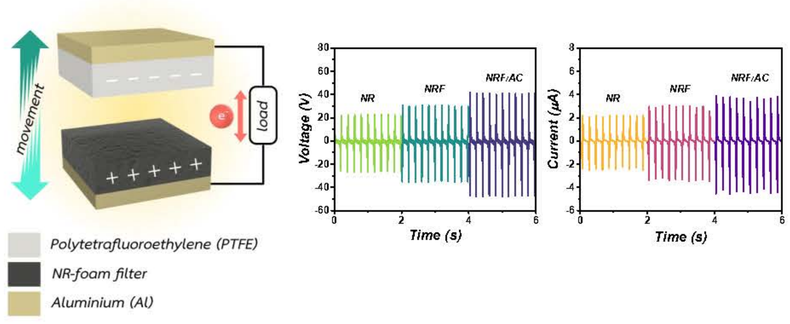

Figure 6. The operation of TENG with electrical output voltage and current.

To evaluate the effectiveness of CO_2 capture by an NR-foam filter layer, a customized test setup was used, which is shown in Fig. 4. The gas was introduced into the system and its passage through the air filter sheet was monitored to quantify the efficiency of CO_2 removal. Using a NR-foam filter, the result showed a maximum CO_2 removal rate of 75%, as shown in Figure 7. However, this high removal efficiency was accompanied by sub-optimal air permeability, suggesting that the filter may not be suitable for applications requiring high airflow. Furthermore, no electrical energy produced from TENG was used to enhance CO_2 attraction in the experiment, suggesting that further optimization could be achieved by using this technique.

Figure 7. The result of CO_2 adsorption system with an NR-foam filter.

Conclusion

NR-foam filters exhibit potential for dual applications in air purification and CO2 capture. Foaming increased the porosity and surface roughness, which improves the efficiency of air filtration. The addition of activated carbon ensured uniform distribution and significantly increased filtration performance. NR-foam filters generated remarkable electrical output (approximately 90 V), making them cost-effective energy sources for CO2 capture. Further optimization using the electrical energy of the triboelectric nanogenerator could maximize the filtration performance. Overall, NR-foam filters prove to be promising, affordable and energy-efficient solutions for sustainable air purification and CO2 capture processes.

Acknowledgements

This research has received funding support from the NSRF via the Program Management Unit for Human Resources & Institutional Development, Research and Innovation
[grant number B13F6600126]

BRAINPOWER CONGRESS 2023

ร่วมกันสร้างและขับเคลื่อนงานวิจัยขั้นแนวหน้า
สู่อุตสาหกรรมแห่งอนาคต

Development of Frontier Researchers in Nanomaterials for Supporting Industrial Research Problems

Topic: Development of carbon dioxide carriers by nanobubble techniques for enhancing economic plant growth

Sornamol Traiphop [a], Sriprajak Kronsuk [a, b] *, Supree Pinitsoontorn [a, b], Prutchayawoot Thopan [c], Likit Temprom [c]

[a] Institute of Nanomaterials Research and Innovation for Energy (IN-RIE), NANOTEC-KKU RNN on Nanomaterials Research and Innovation for Energy, Khon Kaen University, Khon Kaen 40002, Thailand

[b] Department of Physics, Faculty of Science and Institute of Nanomaterials Research and Innovation for Energy (IN-RIE), Khon Kaen University, Khon Kaen 40002, Thailand

[c] Department of Applied Physics, Faculty of Engineering, Rajamangala University of Technology Isan, Khon Kaen 40000, Thailand

Introduction

Plant growth is crucial factor in establishing the yield of crops. Enhancing the plant growth certainly produces a good yield of crops in both quality and quantity.

To promote the plant growth, plant nutrients and photosynthesis reaction are essential parameters. Plant nutrients received from the soil such as nitrogen and potassium, can reduce the effects of plant stress. Additionally, photosynthesis in the leaves of the plant is the main source for their growth. Water (H_2O), carbon dioxide (CO_2) and sunlight are precursors of the photosynthesis reaction.

The photosynthesis rate can be increased by elevating the CO_2 concentration. Accordingly, nanobubble (NBs) techniques play a role in increasing CO_2 concentration in water, know as CO_2 NBs. The CO_2 NBs can be used as foliar fertilization to promote plant growth. Therefore, the stabilization of CO_2 NBs is essential.

To enhance stability, we generated CO_2 NBs and added the surfactant, Span 60 (SP60), and a combination of Span 60/Tween 20 (TW20) to the CO_2 NBs. Additionally, the expected effect of adding the surfactant is the slow release of CO_2 gas to the stoma of plant, superbly promoting plant growth.

Methods

1. Generation of CO_2 nanobubbles (CO_2 NBs) by decompression generator

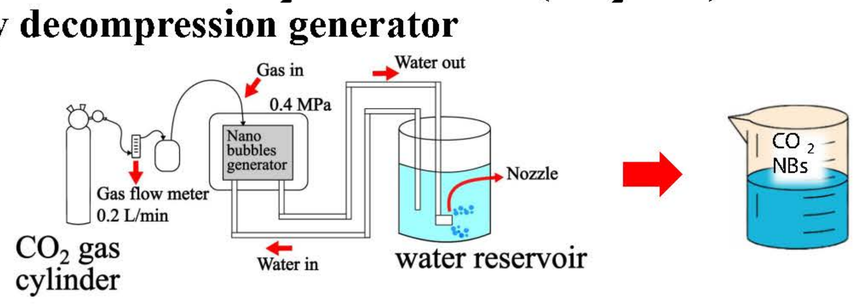

2. Preparation of non-ionic surfactant (Span60 and Tween20) via balling method

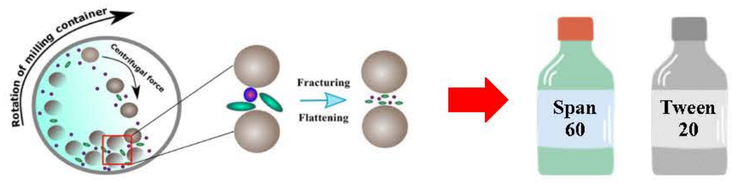

3. Combination of CO_2 NBs and non-ionic surfactant

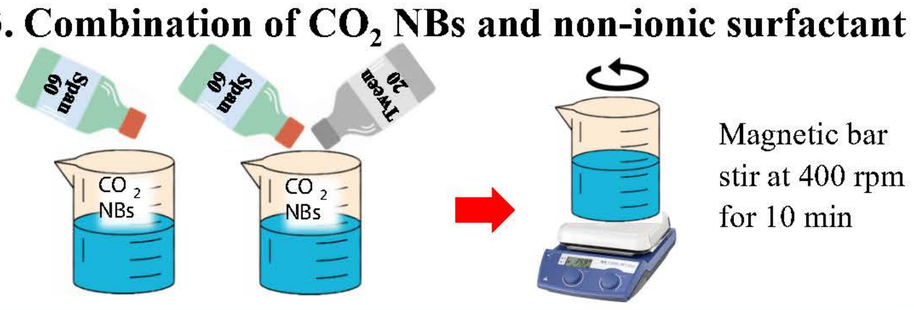

Magnetic bar stir at 400 rpm for 10 min

Results & Discussion

❑ **Samples**

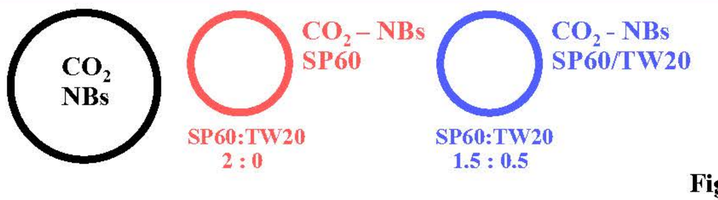

❑ **Physical properties**

Fig 1.

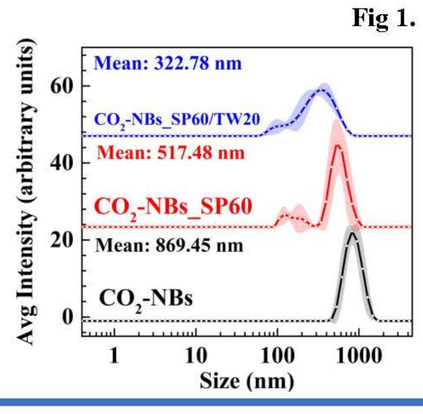

Fig 2.

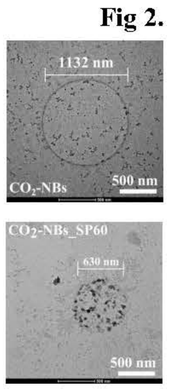

Fig 3.

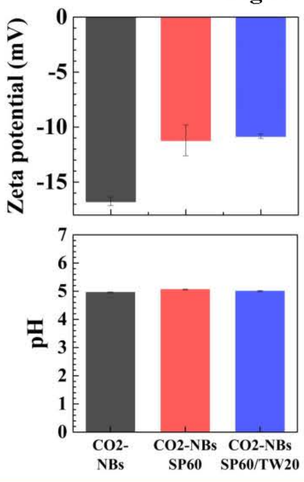

❑ **Stability**

Fig 4.

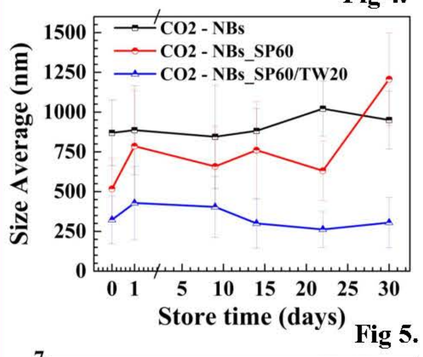

Fig 5.

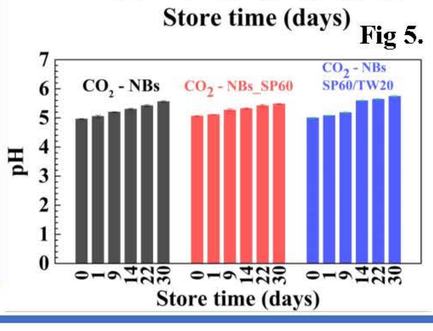

Fig 6.

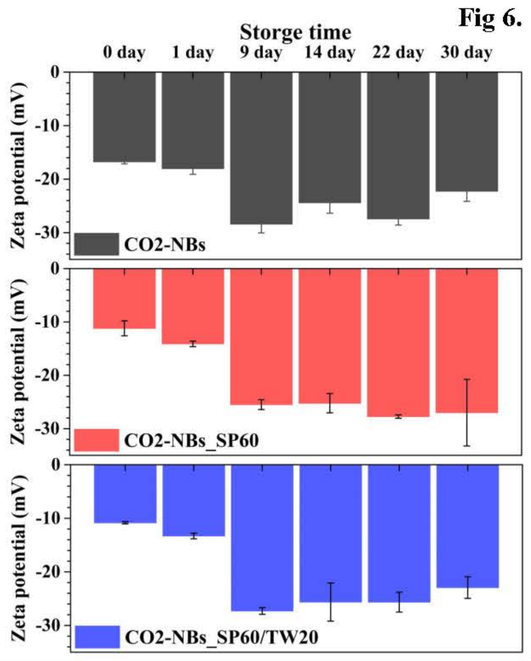

Conclusion

- CO_2 -NBs with average bubbles size 869.45 nm can survive for 1 month in RO water and size average slightly increased to 1000 nm when store for 3 week.
- Addition of Span 60 and Span 60/Tween 20 can reduce the average particle size and Zeta potential of CO_2 –NBs, but this was not affected to the pH value.
- pH value and Zeta potential of 3 samples were increased with increasing the store time.
- Tween 20 addition affect the stability of bubbles in CO_2 -NBs _Sp60 sample. It encourage size retention of bubbles.

Acknowledgements

This research has received funding support from the NSRF via the Program Management Unit for Human Resources & Institutional Development, Research and Innovation [grant number B13F6600126]

BRAINPOWER CONGRESS 2023

ร่วมกันสร้างและขับเคลื่อนงานวิจัยขั้นแนวหน้า
สู่อุตสาหกรรมแห่งอนาคต

Development of Frontier Researchers in Nanomaterials for Supporting Industrial Research Problems

Green Porous Carbon Derived from Sawdust Activated by a Seawater Activator for a Supercapacitor Application

Authit Phakkhawan[1], Suppanat Kosolwattana[2*], Pawinee Klangtakai[1,3†], Supree Pinitsoontorn[1,3]

[1]*Department of Physics, Faculty of Science, Khon Kaen University, Khon Kaen, 40002, Thailand.*

[2]*Department of Chemistry, Faculty of Science, Khon Kaen University, Khon Kaen, 40002, Thailand.*

[3]*Institute of Nanomaterials Research and Innovation for Energy (IN-RIE), Khon Kaen University, Khon Kaen, 40002, Thailand.*

**Corresponding Author' E-mail:* [*]suppako@kku.ac.th, [†]pawinee@kku.ac.th

Introduction

Over the past decade, energy storage systems have garnered extensive attention due to the increasing demand for electric vehicles, wearable electronics, and portable devices in daily life. Supercapacitors, which offer high power densities, safe operation, and long-term stability, among various energy storage devices, play a crucial role in bridging the gap between batteries and dielectric capacitors.

Based on charge storage mechanisms, supercapacitors can be divided into two categories: electrical double-layer capacitors (EDLC) and pseudocapacitors (PDC). EDLC, the first type, relies on electrostatic charge separation at the electrode/electrolyte interface without involving a chemical reaction. Consequently, EDLC provides rapid charge-discharge rates and long-term stability. In contrast, the second type, PDC, relies on a combination of the EDLC mechanism and an electrochemical reversible redox reaction. As a result, PDC offers higher specific capacitance but lower cycling stability than EDLC.

Activated carbon (AC) emerges as a promising candidate for EDLC electrodes due to its abundant availability, cost-effectiveness, and environmentally friendly nature. AC derived from biowaste such as rice husk, orange peel, reed straw, bamboo, and sugarcane bagasse can be easily prepared using an activation process. There are two types of the activation: physical and chemical activation. AC prepared by chemical activation provides higher specific surface areas than physical activation.

This study synthesized activated carbon (AC) from sawdust biomass using a seawater activator, specifically chemical activation. This approach is novel, as there have been no prior reports on AC derived from the sawdust activated through the seawater for supercapacitive applications. Moreover, this method enhances the value of the sawdust and reduces manufacturing costs.

Methods

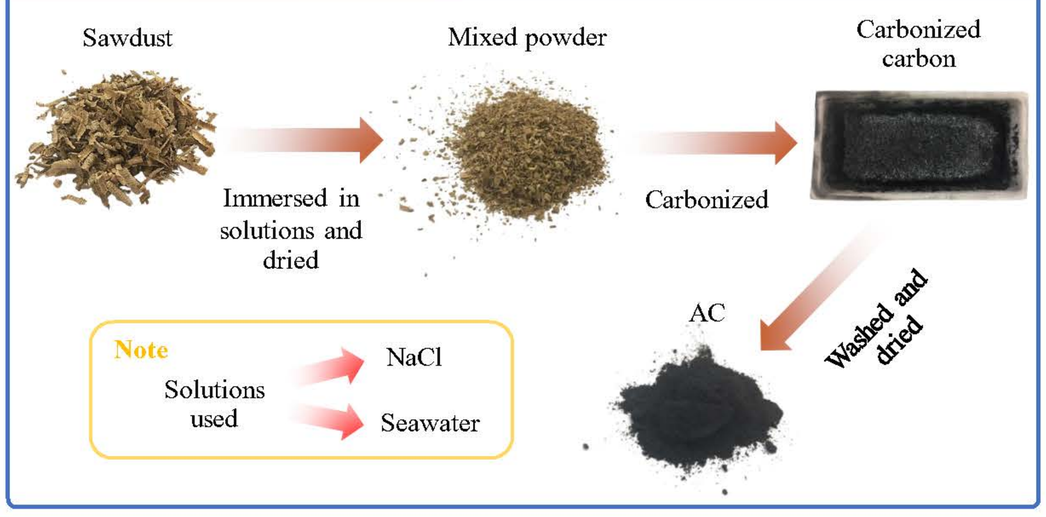

Results & Discussion

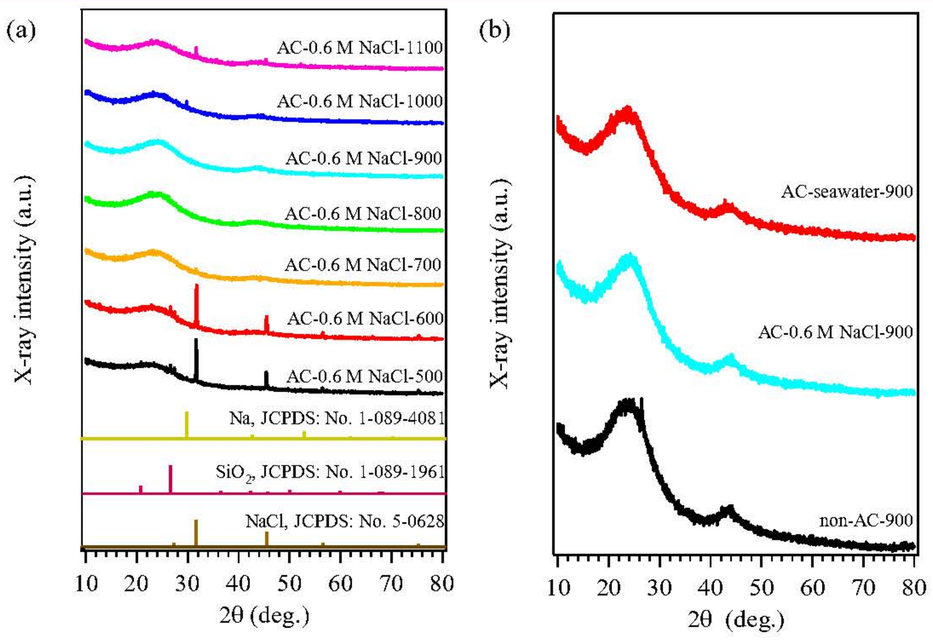

Fig. 1 XRD spectra of (a) ACs treated with a 0.6 M NaCl solution at different temperatures and (b) ACs treated with various activators at 900 °C.

XRD results

At different temperatures

- Activated carbons (ACs) treated with the 0.6 M NaCl solution at 800 °C (AC-0.6 M NaCl-800) and 900 °C (AC-0.6 M NaCl-900) exhibit pure amorphous carbons, whereas other ACs contain impurities.

XRD results

At various activators

- All ACs activated by various activators at 900 °C (non AC-900, AC-0.6 M NaCl-900, and AC-seawater-900) possess pure amorphous carbons.

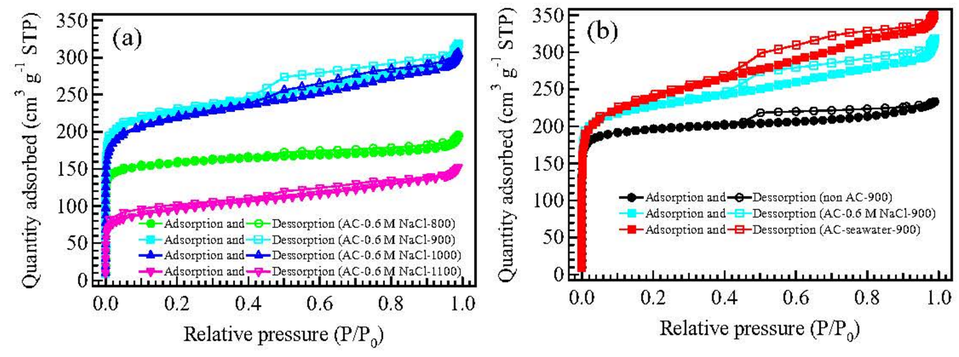

Fig. 2 N_2 adsorption/desorption isotherms of (a) ACs treated with the 0.6 M NaCl solutions at different temperatures and (b) ACs treated with various activators at 900 °C.

N_2 adsorption/desorption isotherms

At different temperatures

- AC-0.6 M NaCl-900 powder provides the highest quantity absorbed, meaning its largest specific surface area.

At various activators

- AC-seawater-900 and AC-0.6 M NaCl-900 powders show higher quantity absorbed than non-AC-900, indicating that two AC powders produce higher specific surface area than non-AC-900.

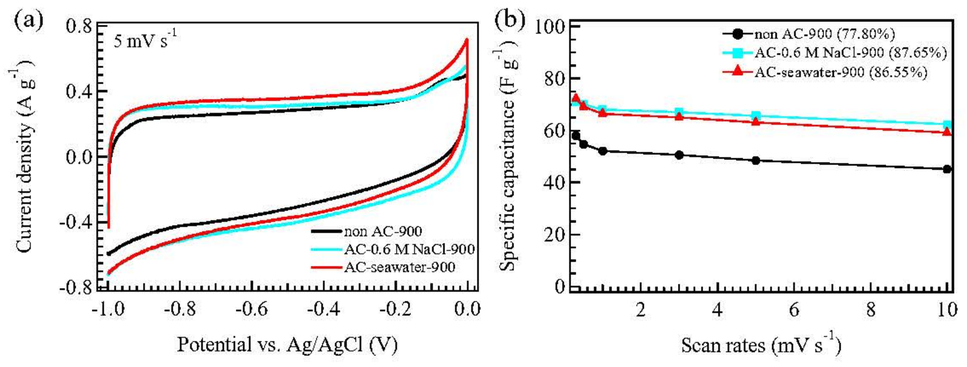

Fig. 3 CV curves of ACs treated with various activators at 900 °C (a) and specific capacitance of all AC electrodes calculated from CV curves.

CV

- All AC electrodes exhibit rectangular curves, indicating a nearly ideal behavior characteristic of EDLC, as seen in Fig. 3a.

At low scan rates (Fig. 3b)

- AC-seawater-900 electrode gives the highest specific capacitance due to its largest specific surface area.

At high scan rates (Fig. 3b)

- AC-0.6 M NaCl-900 electrode shows the highest specific capacitance which might be due to its highest electrical conductivity.

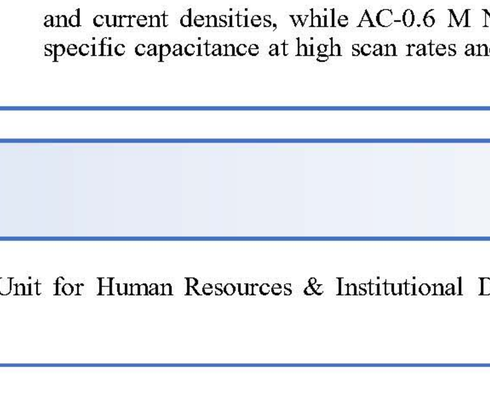

GCD

- AC-seawater-900 electrode achieves the highest specific capacitance at low current densities because of its largest specific surface area.
- AC-0.6 M NaCl-900 electrode possesses the highest rate capability, which is likely attributed to its highest electrical conductivity.

Fig. 4 Specific capacitance of all AC electrodes calculated from GCD curves.

Conclusion

- Activated carbon (AC) derived from sawdust was successfully prepared using either a NaCl or seawater activator.
- At different temperatures, AC-0.6 M NaCl-900 powder provides the largest specific surface area.
- At various activators, AC-seawater-900, and AC-0.6 M NaCl-900 powders present higher specific surface area than non-AC-900 powder.
- Specific capacitance of AC-seawater-900 and AC-0.6 M NaCl-900 electrodes is higher than that of non-AC-900 electrode.
- AC-seawater-900 electrode exhibits the highest specific capacitance at low scan rates and current densities, while AC-0.6 M NaCl-900 electrode demonstrates the highest specific capacitance at high scan rates and current densities.

Acknowledgements

This research has received funding support from the NSRF via the Program Management Unit for Human Resources & Institutional Development, Research and Innovation [grant number B13F6600126]

BRAINPOWER CONGRESS 2023

ร่วมกันสร้างและขับเคลื่อนงานวิจัยขึ้นแนวหน้า
สู่อุตสาหกรรมแห่งอนาคต

Development of Frontier Researchers in Nanomaterials for Supporting Industrial Research Problems

Synthesizing Calcium Carbonate ($CaCO_3$) Material from Natural Waste Materials Using Carbon Dioxide Adsorption for Applications in Capacitors and Humidity-Sensing Devices.

Kaniknun Sreejivungsa[1], Suppanat Kosolwattana*[2], Prasit Thongbai*[1,3] and Supree Pinitsoontorn[1,3]

[1] Department of Physics, Faculty of Science, Khon Kaen University, Khon Kaen 40002, Thailand
[2] Department of Chemistry, Faculty of Science, Khon Kaen University, Khon Kaen 40002, Thailand
[3] Institute of Nanomaterials Research and Innovation for Energy (IN–RIE), Khon Kaen University, Khon Kaen, 40002, Thailand. Corresponding Arthor *Email: suppako@kku.ac.th, pthongbai@kku.ac.th

Introduction

Colossal dielectric permittivity materials have been extensively researched over the years due to their increasing demand in markets and applications in microelectronics [1]. Most of the examined materials show a large dielectric permittivity (ε'). However, the enhanced dielectric response is often accompanied by an increased loss tangent (tan δ) with poor temperature stability in certain properties of dielectric materials [2]. Hence, achieving equilibrium between ε' and tan δ is a primary focus of scientific research and practical applications. Materials that exhibit colossal dielectric constants without the use of lead, and their thermal stability, are attractive for applications in the microelectronics industry, such as memory devices and capacitors. Barium titanate (BaTiO3) [3], lithium-titanium-nickel oxide (LixTiyNi1-x-yO or LTNO) [4], and ceramics are several groups known as giant or colossal dielectric permittivity materials. These materials can be created using an internal barrier layer capacitance (IBLC) structure [5] in a one-step fabrication process. The interesting material is $CaCu_3Ti_4O_{12}$ (CCTO) , derived from waste shells, offering the additional advantage of repurposing waste into capacitors. This study focuses on synthesizing calcium carbonate ($CaCO_3$) from waste shells through carbon dioxide adsorption. The obtained material is then employed in the preparation of CCTO, which can exhibit high dielectric values while maintaining low dielectric loss.

This study to synthesize calcium carbonate from waste shells, subsequently utilizing it in the preparation of CCTO through a solid-state reaction. The X-ray diffraction (XRD) technique is employed to investigate the phase structures of $CaCO_3$, with a focus on optimizing the dielectric properties of CCTO for applications in capacitors and humidity-sensing devices. The study reveals that sintering CCTO at 1060°C results in an optimal dielectric constant (ε') of approximately 114,550 and a loss tangent (tan δ) of about 0.096 at 1 kHz. However, the tan δ of dielectric materials needs improvement for practical applications to enhance the dielectric response. The mechanisms for enhancing the dielectric performance of CCTO are discussed in detail.

Methods

Scheme 1 shows the preparation of CCTO through a solid-state reaction involves the following steps. Initially, powders of calcium carbonate ($CaCO_3$) derived from waste shells, copper oxide (CuO), and titanium dioxide (TiO_2) are weighed in appropriate stoichiometric ratios. These powders are then thoroughly mixed to achieve a homogeneous blend via a solid-state reaction. The mixture is subsequently subjected to high-temperature sintering using a furnace. During this process, the powders undergo a series of chemical transformations, resulting in the formation of the desired compound, CCTO. The reaction parameters, such as temperature and duration, are critical in determining the phase purity and crystalline structure of the final product. Following the reaction, the obtained CCTO is cooled, ground into a fine powder, and may undergo additional processing steps to enhance its properties.

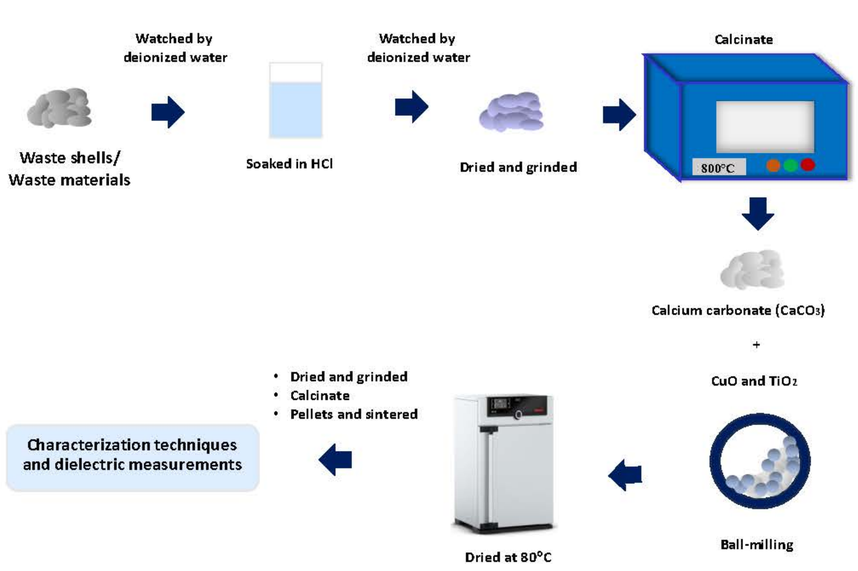

Scheme 1. The synthesis process of CCTO from waste materials.

Result and Discussion

The prepared $CaCO_3$ can then be characterized using X-ray diffraction (XRD), as shown in Figure 1. As observed, there is a difference between natural waste shells and those calcined at 800°C for 3 hours. XRD results revealed the presence of $CaCO_3$ Aragonite (JCPDS no. 01-076-0606), $CaCO_3$ Calcium Carbonate (JCPDS no.01-085-1108), and $Ca(OH)_2$ Calcium Hydroxide (JCPDS no. 01-076-0570).

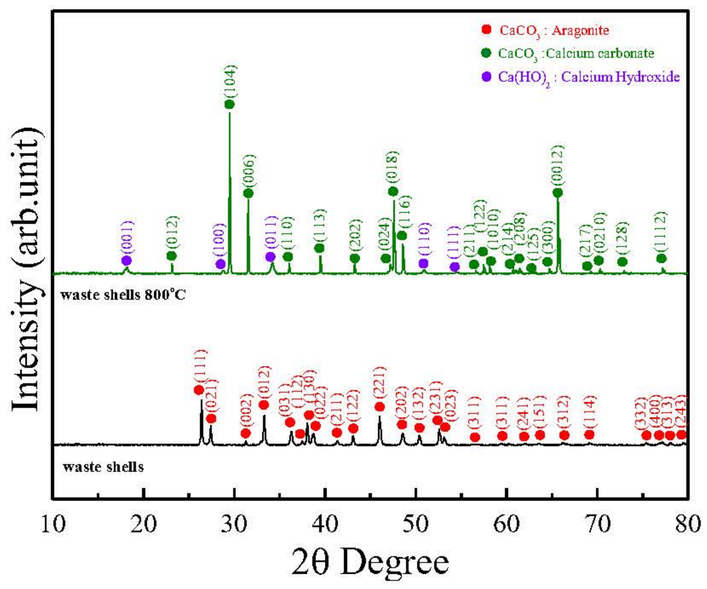

Figure 1. The XRD patterns of waste shells, highlighting the distinctions between natural waste shells and those calcined at 800°C for 3 h .

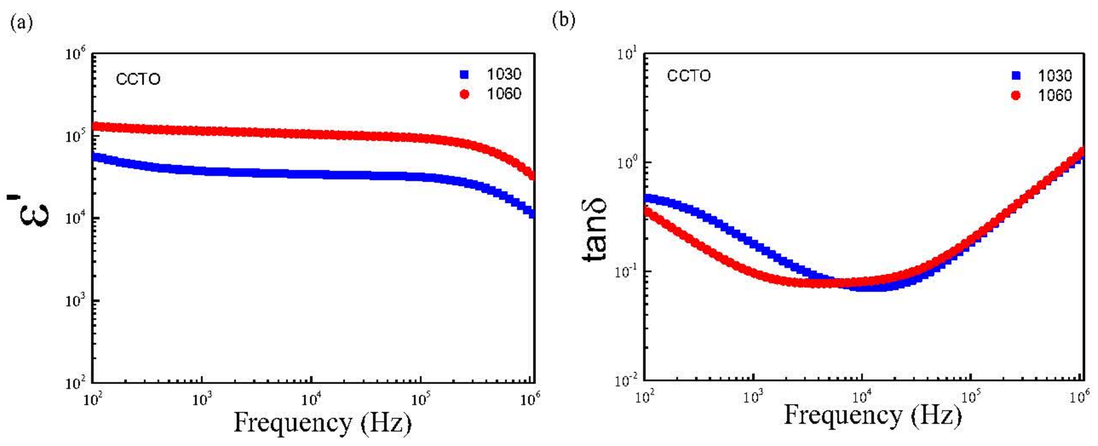

Figure 2. The frequency dependence of (a) ε′ and (b) tanδ at room temperature for CCTO ceramics sintered at different temperatures is investigated.

The frequency dependence at room temperature of ε′ and tanδ for CCTO with various temperature sintered is illustrated in Figure 2. In the present study, a distinct frequency dependence is observed for ε′ and tanδ in CCTO ceramics sintered at different temperatures. Notably, the ε′ values at 1 kHz for ceramics sintered at 1060°C are significantly higher (114,550) than those sintered at 1030°C (37,350). This enhancement is attributed to the denser microstructure of the CCTO sintered at 1060°C, corresponding to the relative density of each ceramic sample. Furthermore, the observed lower tanδ value for the CCTO sample sintered at 1060°C (0.096), in comparison to that sintered at 1030°C (0.178), aligns with the higher grain boundary resistance (Rgb) of the 1060°C sintered CCTO. This outcome suggests that the microstructure of the 1060°C sintered sample contributes to reduced energy dissipation, resulting in a lower loss tangent. It's noteworthy that the dielectric constant could be further enhanced by strategically adjusting preparation parameters. Parameters such as sintering temperature, sintering time, and doping offer avenues for optimization. The fine-tuning of these factors in the fabrication process has the potential to positively impact the dielectric constant, providing opportunities for tailoring the material properties to meet specific application requirements.

Conclusion

To synthesize calcium carbonate ($CaCO_3$) from waste shells and subsequently utilize it in the preparation of $CaCu_3Ti_4O_{12}$ (CCTO) through a solid-state reaction, the X-ray diffraction (XRD) technique is employed to investigate the phase structures of $CaCO_3$. The focus is on optimizing the dielectric properties of CCTO for applications in high-energy storage capacitors and humidity change sensing devices. The study reveals that sintering CCTO at 1060°C results in an optimal dielectric constant (ε') of approximately 114,550 and a loss tangent (tan δ) of about 0.096 at 1 kHz.

Acknowledgements: This research has received funding support from the NSRF via the Program Management Unit for Human Resources & Institutional Development, Research and Innovation [grant number B13F6600126.]

Reference

1. Wang Y, Jie W, Yang C, Wei X, Hao J. Colossal Permittivity Materials as Superior Dielectrics for Diverse Applications. **Advanced Functional Materials** 2019; 29: 1808118.

2. Mao P, Wang J, Xiao P, Zhang L, Kang F, Gong H. Colossal dielectric response and relaxation behavior in novel system of Zr4+ and Nb5+ co-substituted CaCu3Ti4O12 ceramics. **Ceramics International** 2020; 47.

3. Buscaglia V, Buscaglia MT, Canu G. BaTiO3-Based Ceramics: Fundamentals, Properties and Applications. In: Pomeroy M, editor. Encyclopedia of Materials: Technical Ceramics and Glasses. Oxford: Elsevier; 2021. p. 311-344.

4. Thongbai P, Yamwong T, Maensiri S. Microstructure and modified giant dielectric response in Ga-doped La1.5Sr0.5NiO4 ceramics. **Materials Letters** 2012; 82: 244-247.

5. Li J, Li F, Zhuang Y, Jin L, Wang L, Wei X, et al. Microstructure and dielectric properties of (Nb + In) co-doped rutile TiO2 ceramics. **Journal of Applied Physics** 2014; 116: 074105.

BRAINPOWER CONGRESS 2023

ร่วมกันสร้างและขับเคลื่อนงานวิจัยขึ้นแนวหน้า
สู่อุตสาหกรรมแห่งอนาคต

Biomass derived laser-induced graphene for capsaicin detection in chili pepper samples

Asamee Soleh[1,2,3], Kasrin Saisahas[1,3], Dongsayam Somapa[4], Namchoke Somapa[4] and Warakorn Limbut[1,2,3]*

[1] Forensic Science Innovation and Service Center, Prince of Songkla University, Hat Yai, Songkhla 90110, Thailand
[2] Center of Excellence for Trace Analysis and Biosensor, Prince of Songkla University, Hat Yai, Songkhla 90110, Thailand
[3] Division of Health and Applied Sciences, Faculty of Science, Prince of Songkla University, Hat Yai, Songkhla 90110, Thailand
[4] Master Lab Incorporation Company Limited, 12 Prayasuren, 35 Bangchun Klongsamwa, Bangkok 10510, Thailand
*Corresponding author: Tel: 074-288563; Fax: 074-446681; E-mail address: warakorn.l@psu.ac.th

Background and Rational

Oil palm biomass

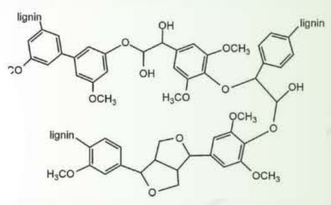

Lignin

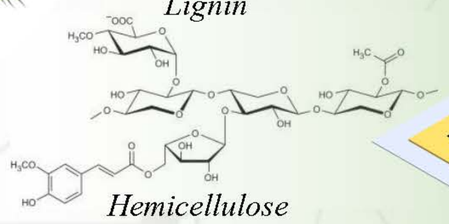

Hemicellulose

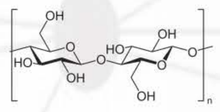

Cellulose

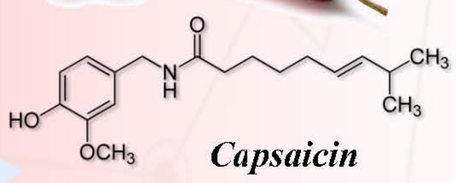

Capsaicin

Estimate the pungent level of raw chili

Control the pungent level during the production process

Quality control of finished products

Objective

We aim to develop a sustainable electrochemical sensor for the detection of the pungency of chili peppers. This sensor will be based on a laser-induced graphene electrode derived from palm oil biomass.

Methods

➢ Fabrication of biomass-LIG electrode

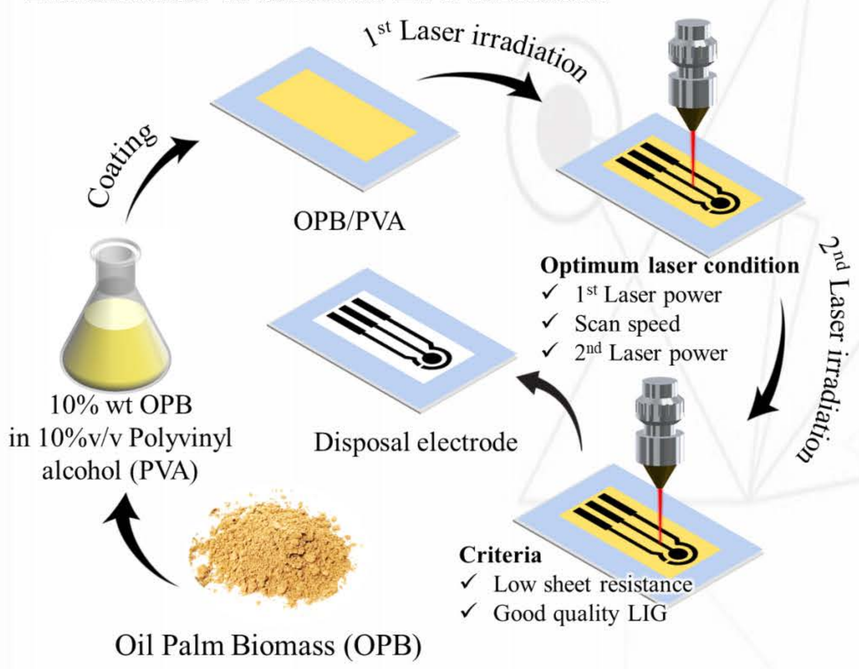

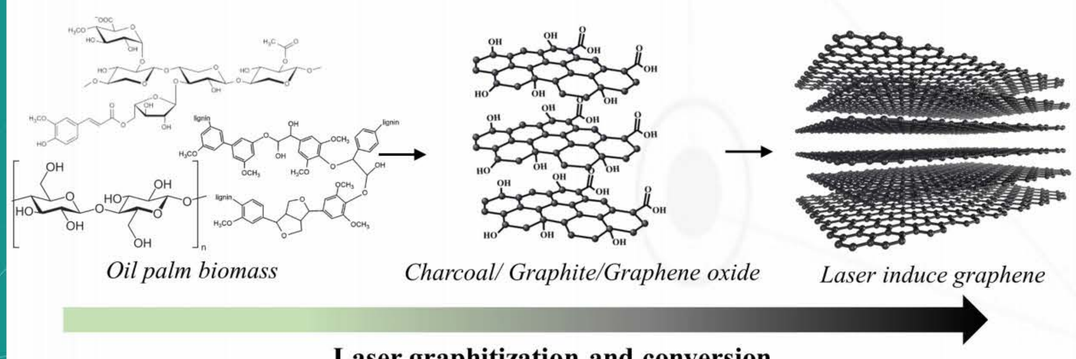

Results

➢ Optimization of laser irradiation process

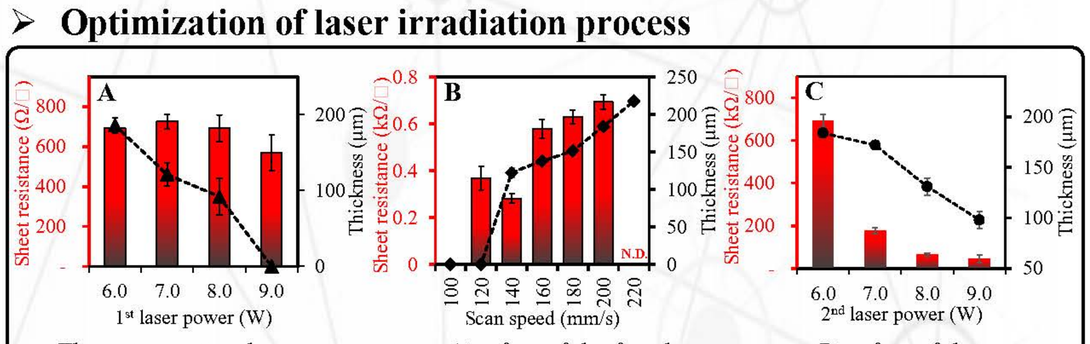

The optimization laser parameter; (A) effect of the first laser power; (B) effect of the scan speed; (C) effect of the second laser power.

➢ Characterizations of morphology

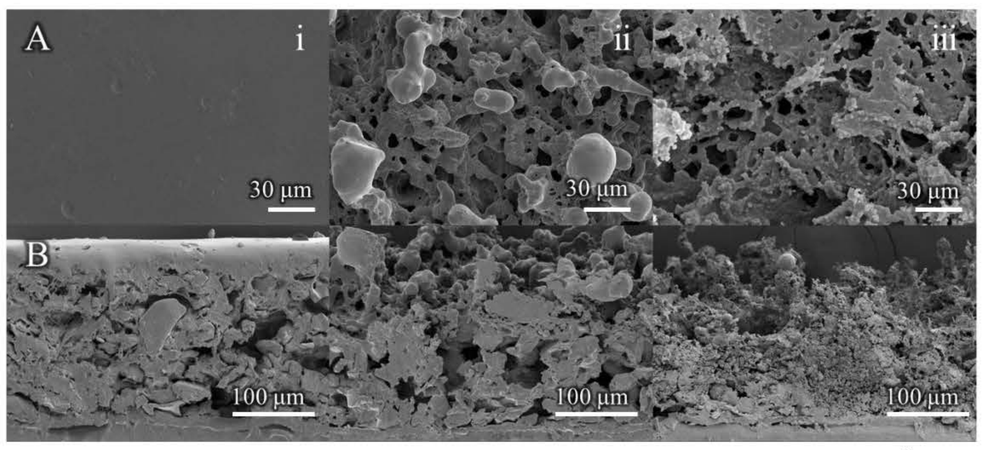

(A) Top-view and (B) cross-sectional SEM images of OPB-PVA (i), 1st-LIG (ii), and 2nd-LIG (iii).

➢ Electrochemical characterization

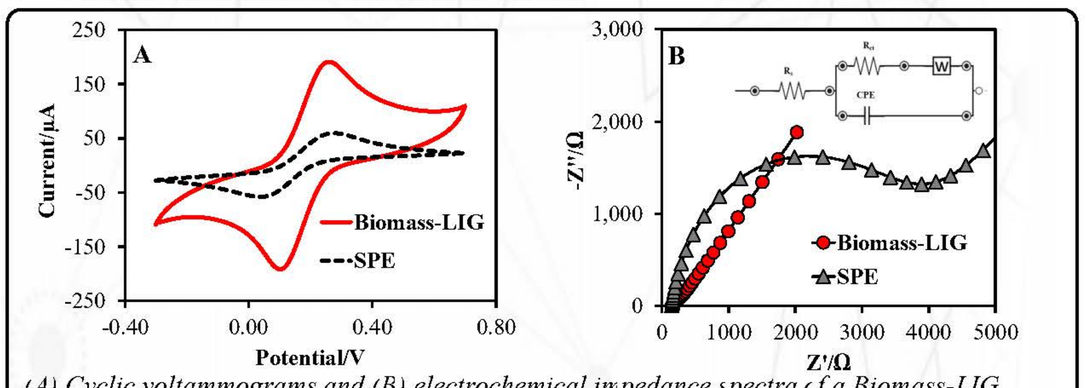

(A) Cyclic voltammograms and (B) electrochemical impedance spectra of a Biomass-LIG and commercial SPE in 5.0 mM $[Fe(CN)_6]^{3-/4-}$ containing 0.10 M KCl.

➢ Capsaicin detection

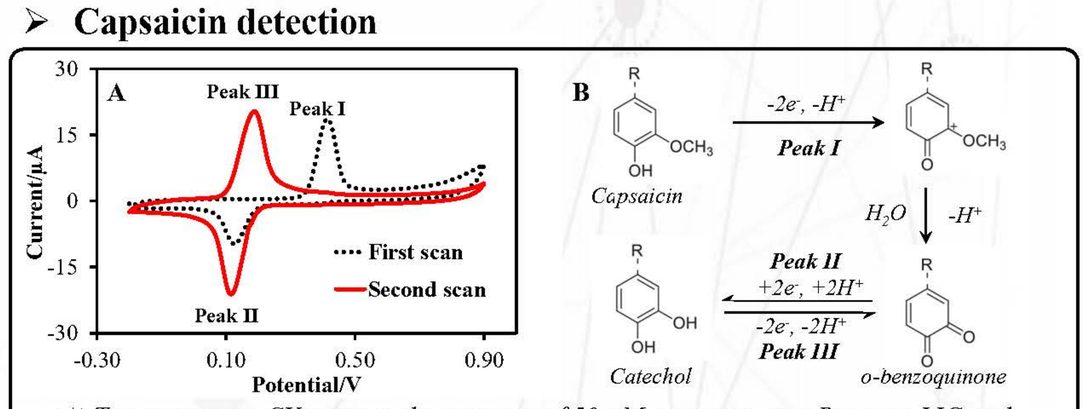

(A) Two successive CV scans in the presence of 50 μM capsaicin on a Biomass-LIG and (B) mechanism of the electrochemical oxidation and reduction of capsaicin.

Conclusions

A laser-induced graphene disposable electrode made from biomass was successfully developed using a simple and facile fabrication method involving laser irradiation. This electrode exhibits good electrochemical properties and has been successfully applied to the determination of capsaicin.

Acknowledgements

This research has received funding support from the NSRF via the Program Management Unit for Human Resources & Institutional Development, Research and Innovation [grant number B13F660128]

BRAINPOWER CONGRESS 2023

ร่วมกันสร้างและขับเคลื่อนงานวิจัยขึ้นแนวหน้า
สู่อุตสาหกรรมแห่งอนาคต

The development of an electrochemical sensor for the detection of creatinine and albumin in human fluids

Supatinee Kongkaew [1,2,3], Dongsayam Somapa[4], Namchoke Somapa[4] and Warakorn Limbut[1,2,3*]

[1] Forensic Science Innovation and Service Center, Prince of Songkla University, Hat Yai, Songkhla 90110, Thailand
[2] Center of Excellence for Trace Analysis and Biosensor, Prince of Songkla University, Hat Yai, Songkhla 90110, Thailand
[3] Division of Health and Applied Sciences, Faculty of Science, Prince of Songkla University, Hat Yai, Songkhla 90110, Thailand
[4] Master Lab Incorporation Company Limited, 12 Prayasuren, 35 Bangchun Klongsamwa, Bangkok 10510, Thailand
*Corresponding author: Tel: 074-288563; Fax: 074-446681; E-mail address: warakorn.l@psu.ac.th

Introduction

Diabetic kidney disease (CKD)
or
Diabetic nephropathy (DN)

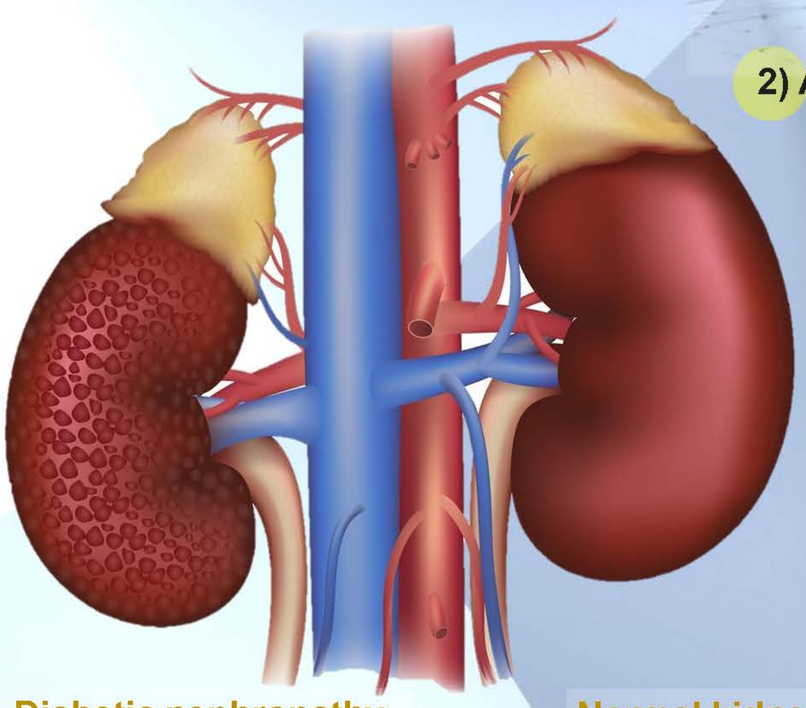

Diabetic nephropathy — Normal kidney

Approximately **20** to **40**% of **diabetic** patients develop ***CKD.***

CKD is the most common cause of ***End-Stage Renal Disease*** **(ESRD) worldwide.**

Indicators

1) Albuminuria: >300 milligrams/ 24 hours or 200 micrograms /minutes
2) Albumin-to-creatinine ratio (ACR): > 300 milligrams albumin /grams creatinine

A device for screening and diagnosing CKD is required urgently.

Methods

Synthesis of AC-PKS from palm kernel

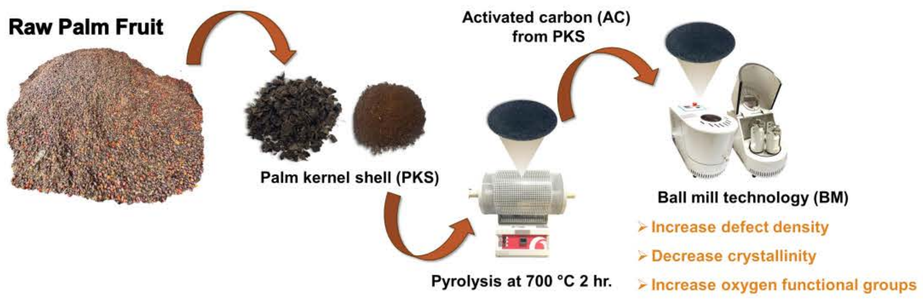

Label-free immobilization process

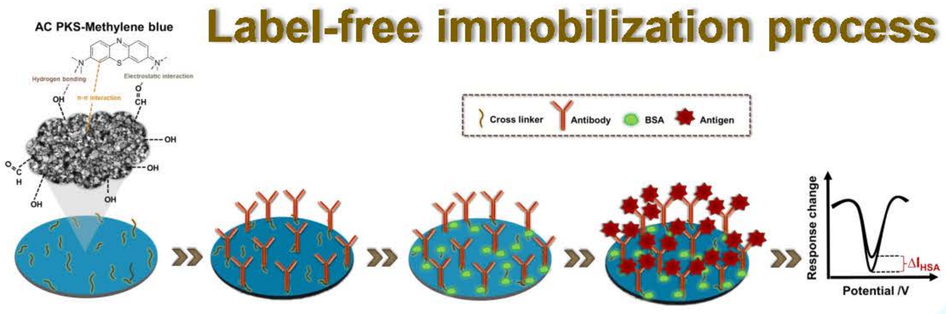

Conclusion

Activated carbon was successfully synthesized from palm kernel shell using the pyrolysis method. The use of ball mill technology results in a reduction in the gain size of AC-PKS material to nanoscale, as well as an increase in oxygen functional groups on the surface of AC-PKS. During the BM process, the dispersion in organic solvent went through an increase. The presence of oxygen functional groups on the PKS surface facilitates the absorption of methylene blue, which can act as a redox probe for further label-free albumin biosensor.

Acknowledgements

This research has received funding support from the NSRF via the Program Management Unit for Human Resources & Institutional Development, Research and Innovation [grant number B13F660128]

Results and discussion

AC-PKS morphology characterization

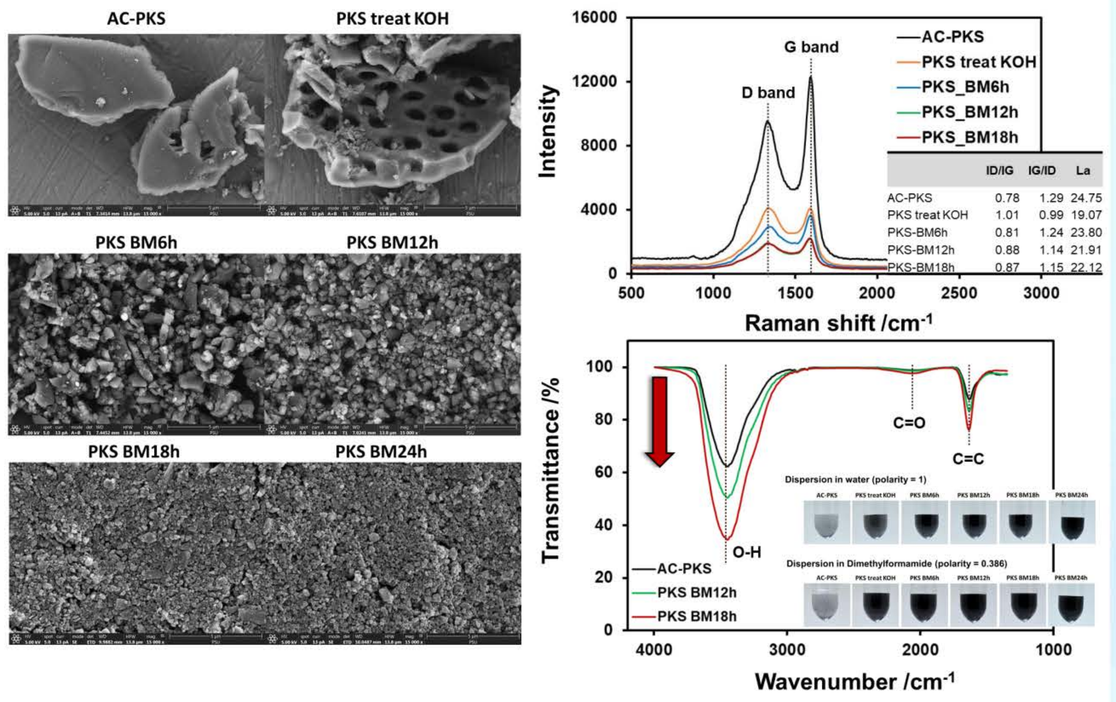

AC-PKS electrochemical characterization

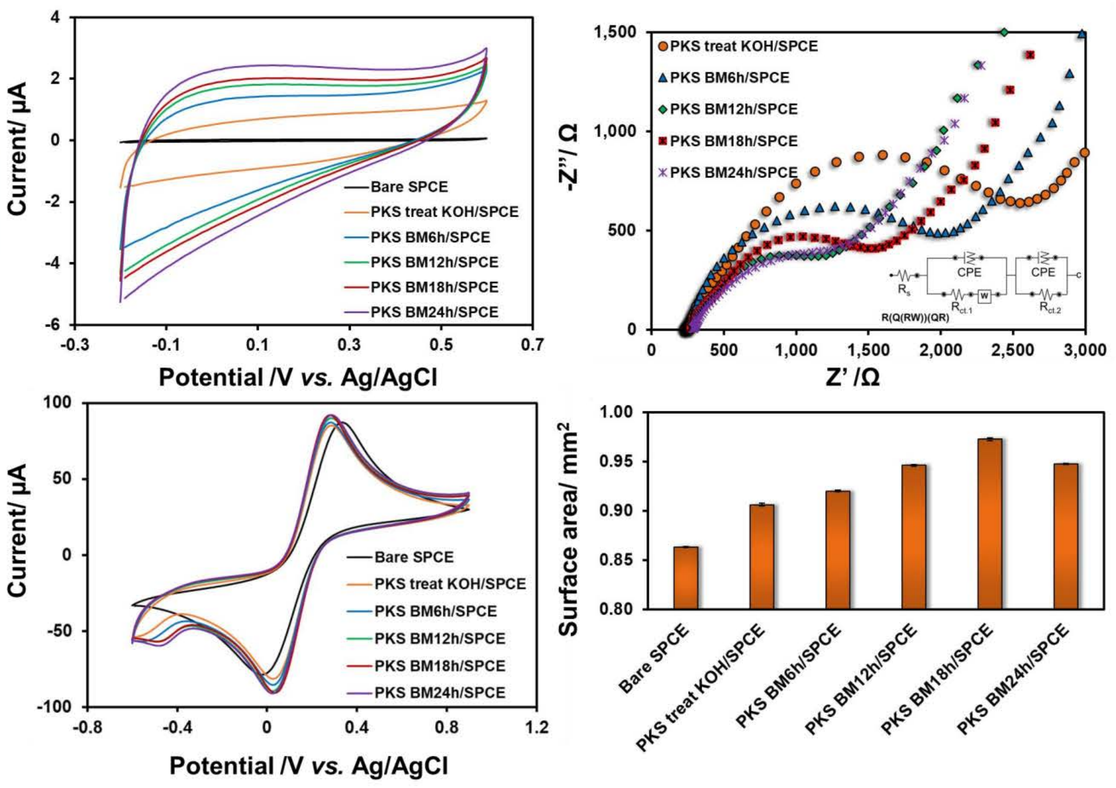

AC-PKS absorbed Methylene blue

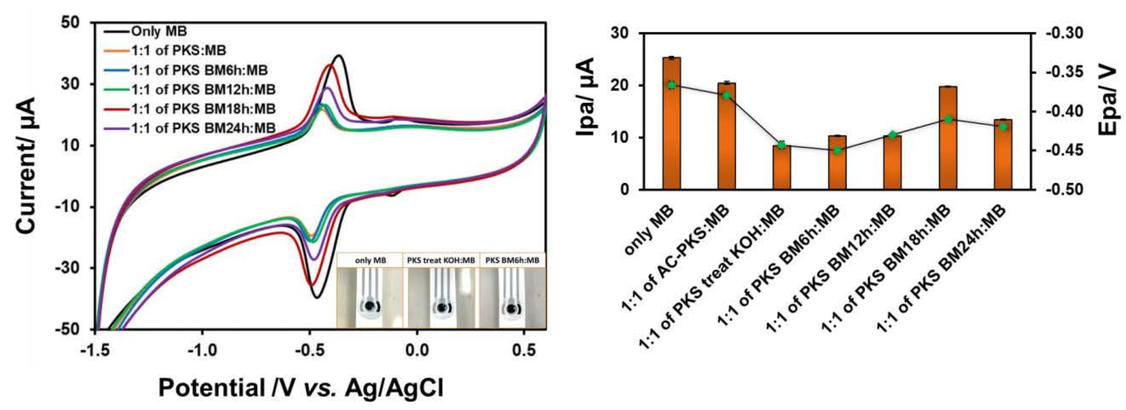

BRAINPOWER CONGRESS 2023

ร่วมกันสร้างและขับเคลื่อนงานวิจัยขั้นแนวหน้า
สู่อุตสาหกรรมแห่งอนาคต

Portable electrochemical sensor for the detection of curcumin in turmeric samples

Kritsada Samoson[1,2,3], Dongsayam Somapa[4], Namchoke Somapa[4] and Warakorn Limbut[1,2,3*]

[1] Forensic Science Innovation and Service Center, Prince of Songkla University, Hat Yai, Songkhla 90110, Thailand
[2] Center of Excellence for Trace Analysis and Biosensor, Prince of Songkla University, Hat Yai, Songkhla 90110, Thailand
[3] Division of Health and Applied Sciences, Faculty of Science, Prince of Songkla University, Hat Yai, Songkhla 90110, Thailand
[4] Master Lab Incorporation Company Limited, 12 Prayasuren, 35 Bangchun Klongsamwa, Bangkok 10510, Thailand
*Corresponding author: Tel: 074-288563; Fax: 074-446681; E-mail address: warakorn.l@psu.ac.th

Background and Rational

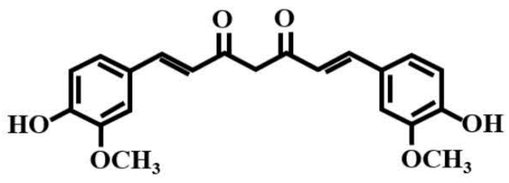

Curcumin (CUR)

Curcuma longa L.

Therapeutic benefits

- Cardiovascular diseases
- Depression
- Allergies
- Colitis
- Psoriasis
- Cancers

Conventional methods

Gas Chromatography

Spectrophotometer

High Performance Liquid Chromatography (HPLC)

Limitations

- Large equipment
- High operating costs
- Complicated procedure
- Long analysis time
- Unsuitable for on-site detection

Electrochemical method

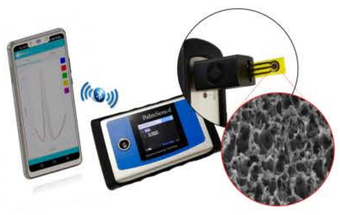

Portable CUR sensor

- Portability
- Simplicity
- Fast response
- High sensitivity
- Suitable for on-field analysis

Objective

To develop a new portable electrochemical sensor for the detection of curcumin (CUR) based on a nitrogen and sulfur-doped laser-induced graphene electrode (N-S@LIG)

Methods

➢ Fabrication of N-S@LIGE electrode

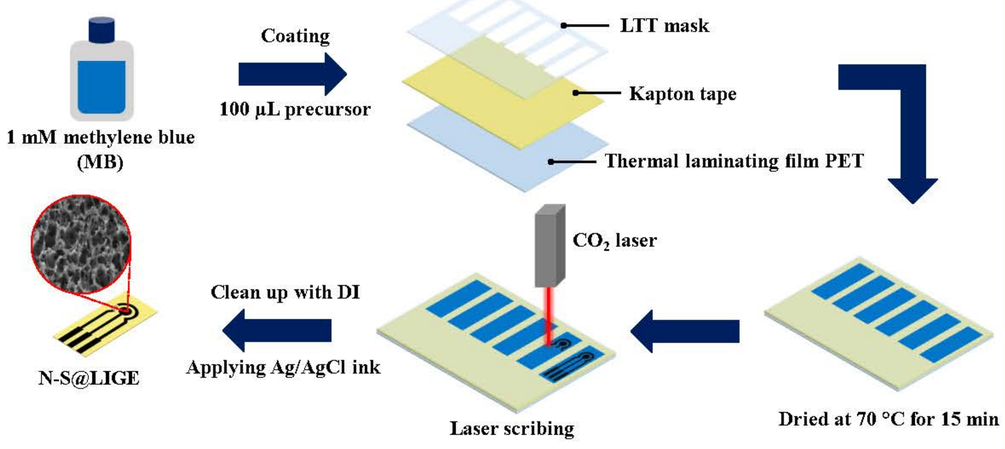

➢ Electrochemical measurement

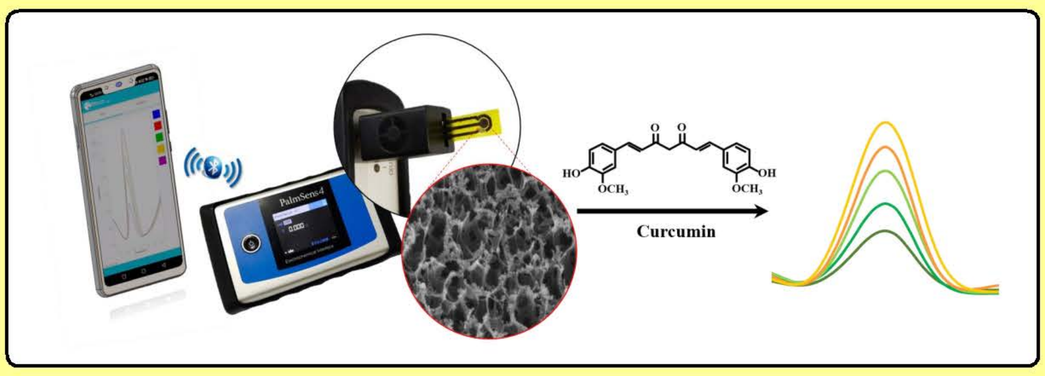

Results

➢ Characterizations of morphology

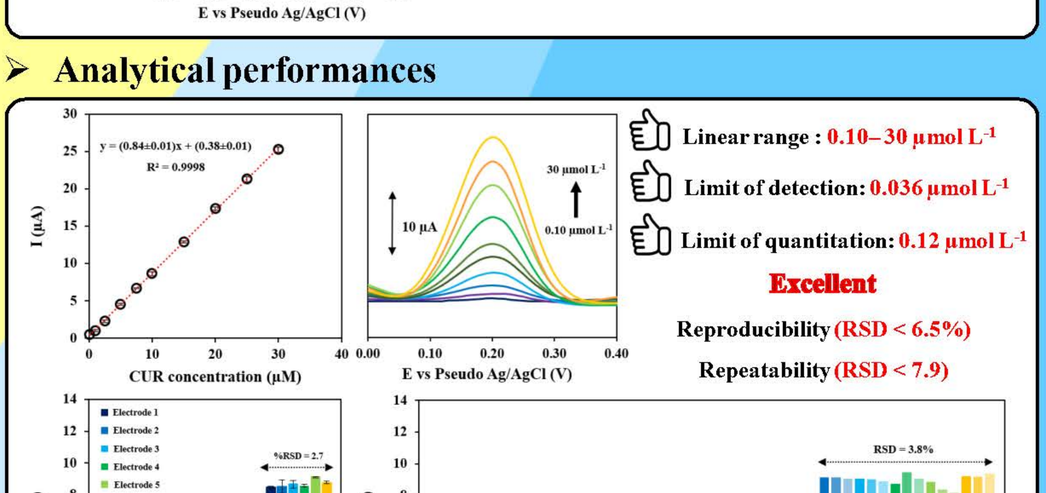

➢ Electrochemical characterization

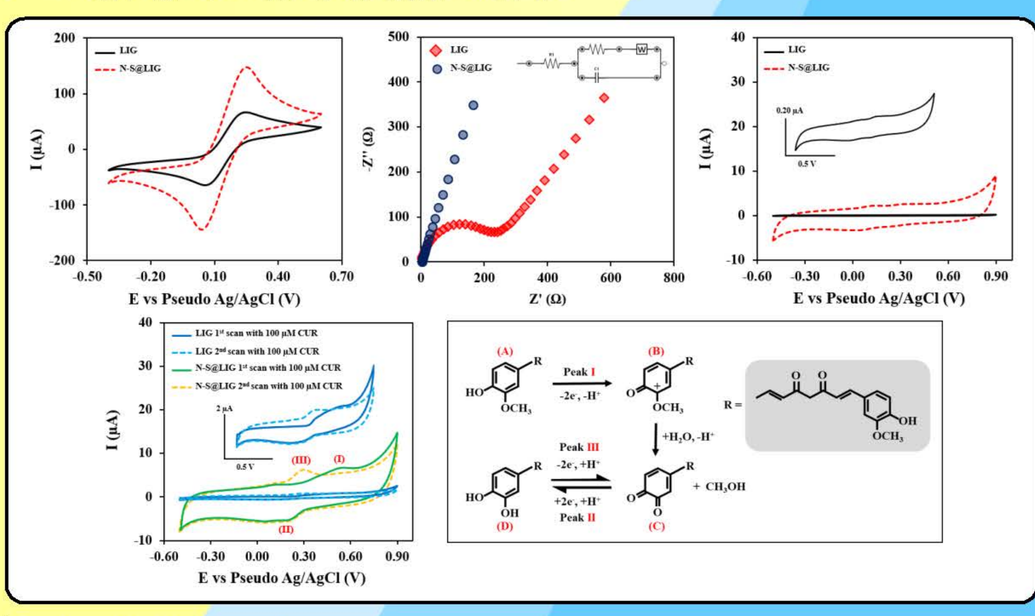

➢ Analytical performances

- Linear range : 0.10–30 µmol L^{-1}
- Limit of detection: 0.036 µmol L^{-1}
- Limit of quantitation: 0.12 µmol L^{-1}

Excellent

Reproducibility (RSD < 6.5%)

Repeatability (RSD < 7.9)

Conclusions

A portable CUR sensor was successfully developed based on N-S@LIGE. The proposed method provided a wide linear range, low detection limit, excellent reproducibility and good repeatability. Moreover, this sensor could possibly be applied for the determination of CUR in cultivated rhizomes and commercial turmeric products.

Selected References

1. D. Zhang, X. Ouyang, J. Ma, L. Li and Y. Zhang, Electroanalysis, 2016, 28, 749-756.
2. H. Zhou, C. S. Beevers and S. Huang, Current drug targets, 2011, 12, 332-347.
3. S. Prasad and A. K. Tyagi, Food & Function, 2015, 6, 3412-3419.

Acknowledgements

This research has received funding support from the NSRF via the Program Management Unit for Human Resources & Institutional Development, Research and Innovation [grant number B13F660128]

BRAINPOWER CONGRESS 2023

ร่วมกันสร้างและขับเคลื่อนงานวิจัยขึ้นแนวหน้า สู่อุตสาหกรรมแห่งอนาคต

Electrochemical sensors for detection of mercury in cosmetics

Chanakarn Sanguarnsak[1,2,3], Kiattisak Promsuwan[1,2,3], Dongsayam Somapa[4], Namchoke Somapa[4] and Warakorn Limbut[1,2,3*]

[1] Forensic Science Innovation and Service Center, Prince of Songkla University, Hat Yai, Songkhla 90110, Thailand

[2] Center of Excellence for Trace Analysis and Biosensor, Prince of Songkla University, Hat Yai, Songkhla 90110, Thailand

[3] Division of Health and Applied Sciences, Faculty of Science, Prince of Songkla University, Hat Yai, Songkhla 90110, Thailand

[4] Master Lab Incorporation Company Limited, 12 Prayasuren, 35 Bangchun Klongsamwa, Bangkok 10510, Thailand

*Corresponding author: Tel: 074-288563; Fax: 074-446681; E-mail address: warakorn.l@psu.ac.th

Introduction

SIDE EFFECTS

CONVENTIONAL METHODS

Limitations

- ✓ Expensive
- ✓ Time consuming
- ✓ Large instrument
- ✓ Need skill operation
- ✓ Complicated procedure

ELECTROCHEMICAL METHOD

- Fast analysis
- High sensitivity
- Simple operation
- On-field analysis
- Portable

Methods

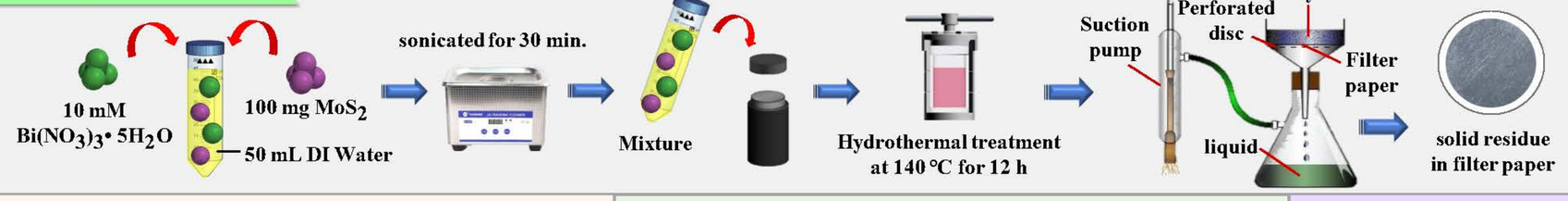

Synthesis of $Bi(NO_3)_3/MoS_2$

Preparation of the $Bi(NO_3)_3/MoS_2$ Nanocomposite

Electrode Fabrication

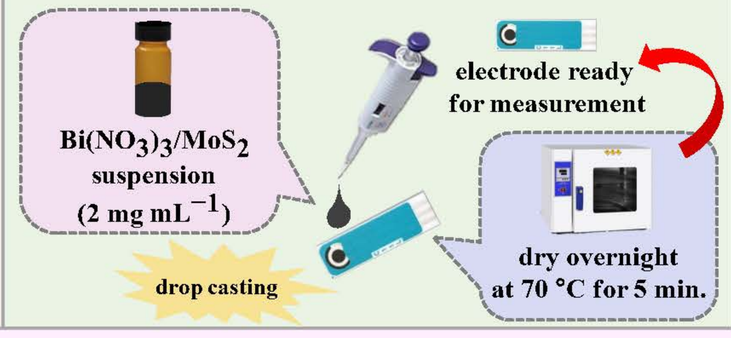

Electrochemical measurement

Schematic illustration of bismuth particle absorbed on the surface of molybdenum disulfide (MoS_2) and Hg^{2+} bind to sulfur on the surface of MoS_2

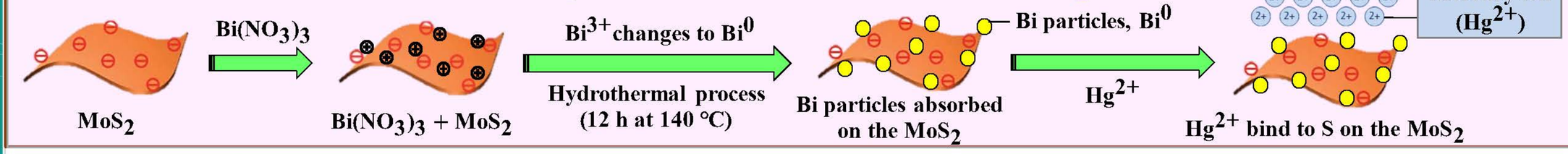

Results

Optimizations

Optimization of electrode fabrications

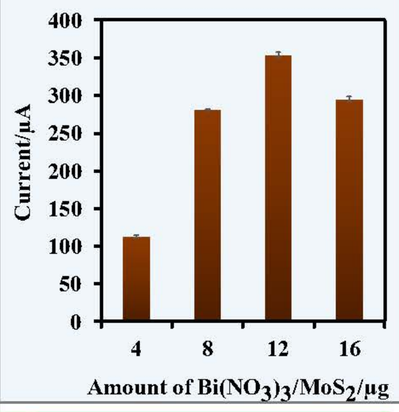

Optimization of operational conditions

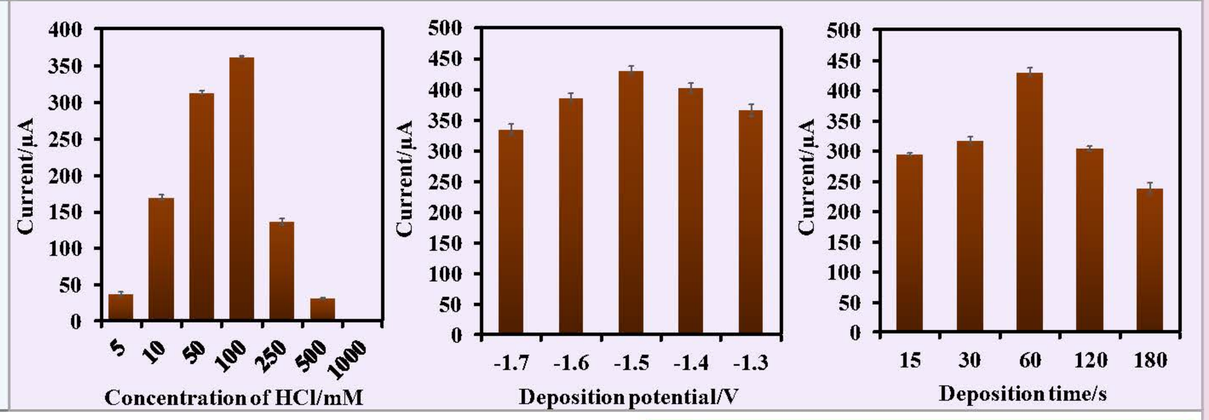

Linearity

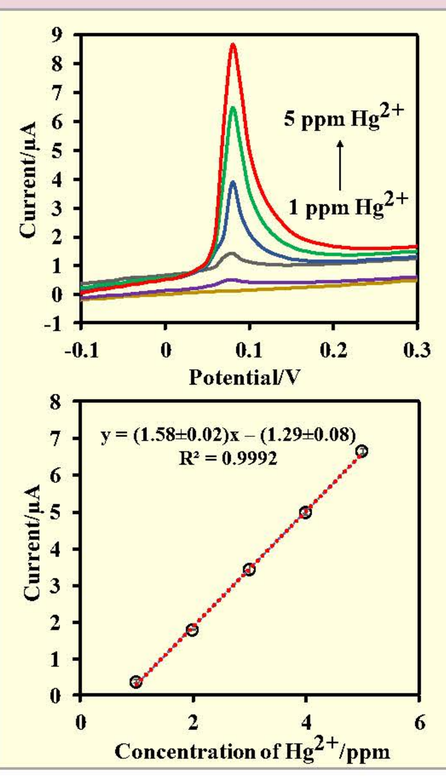

Conclusions

Mercury is a toxic metal that can cause severe toxic effects, including kidney damage, anxiety, depression, and peripheral neuropathy. In this study, "$Bi(NO_3)_3/MoS_2$" was used as a working electrode for the development of an electrochemical sensor for the detection of mercury (II) ions. The study also involved optimizing the analyte and operating conditions, aiming to improve the selectivity, sensitivity, and reliability of the electrode for mercury detection.

Acknowledgements

This research has received funding support from the NSRF via the Program Management Unit for Human Resources & Institutional Development, Research and Innovation [grant number B13F660128]

BRAINPOWER CONGRESS 2023

ร่วมกันสร้างและขับเคลื่อนงานวิจัยขั้นแนวหน้า
สู่อุตสาหกรรมแห่งอนาคต

TECHNOLOGY OF INNOVATIVE SENSOR TO ENHANCE THE COMPETITIVENESS OF THE METAL PLATING INDUSTRY

Phanumas Yomthiangthae[a], Tatchai Hongyangyuen[a] and Yuttanant Boonyongmaneerat[*b]

[a]Nexus Surface Innovation Co., Ltd.

[b]Metallurgy and Materials Science Research Institute, Chulalongkorn University, Bangkok 10330 Thailand

INTRODUCTION

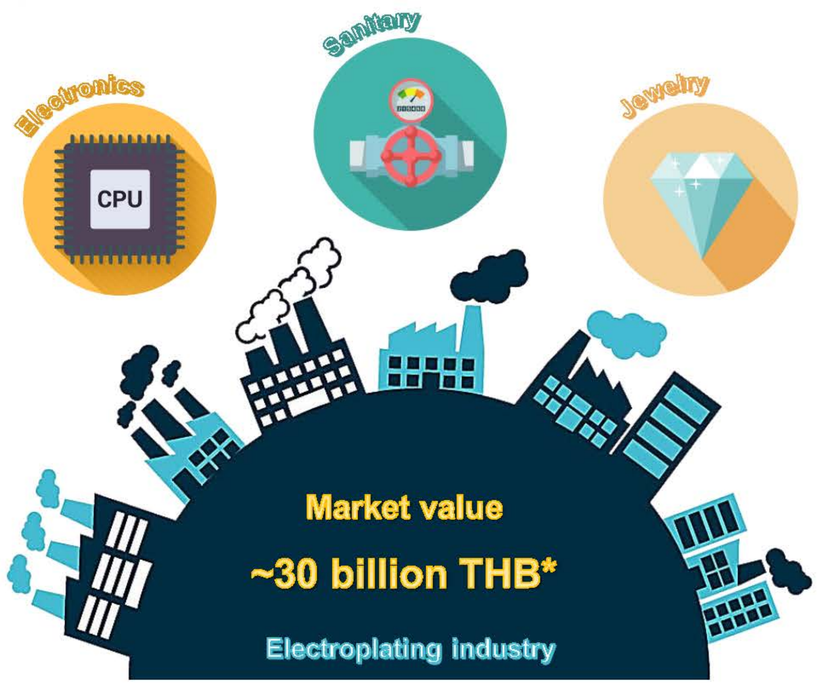

Data from Thailand Electroplating Network

Precious metals

Laboratory-based method

X-ray diffraction (XRD), Inductively coupled plasma (ICP)

- Complicated process
- Costly instrument
- Long analysis time

Objectives

To develop an easily handled system for the detection of gold (as Au(I)) in the plating solution and the wastewater containing precious metals.

METHODS

Optimizing parameters

- To study experimental conditions that affected the detection of Au(I)

Applying to field test

- Testing of a protocol for the detection of Au(I) in the plating solution and the wastewater containing precious metals

01 | 02 | 03 | 04

Selecting equipment

- The potentiostat is portable and easy-to-use, compatible with a miniaturized system

Method validation

- Analytical performance is examined to study sensitivity, selectivity, and repeatability.

Composition of a sensor

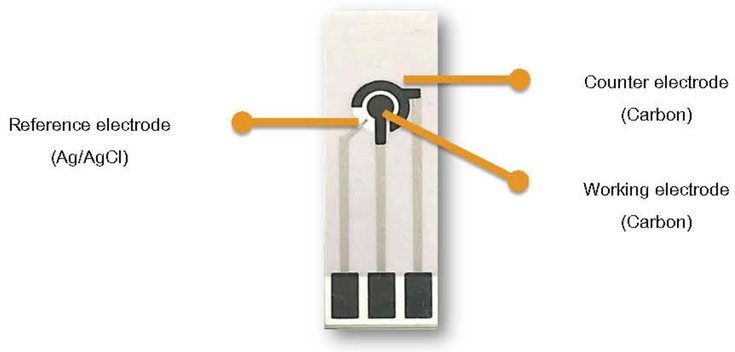

Screen-printed carbon electrode

Electrochemical detection of Au(I) ions

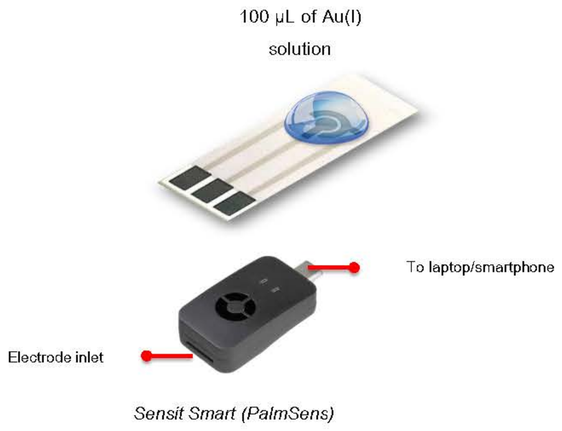

Sensit Smart (PalmSens)

Electrochemical response of Au(I)

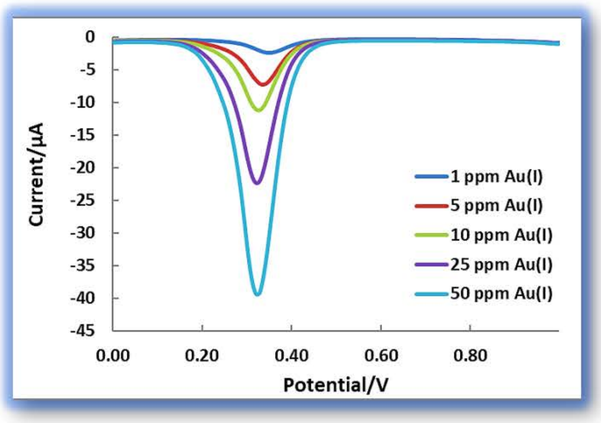

RESULTS & DISCUSSION

Optimization of electrochemical parameters

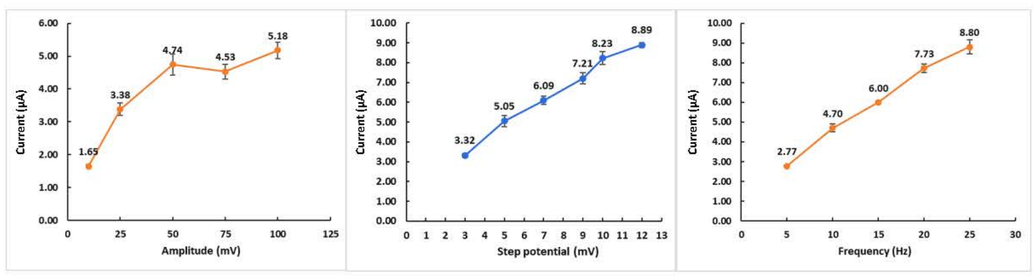

Analytical performance

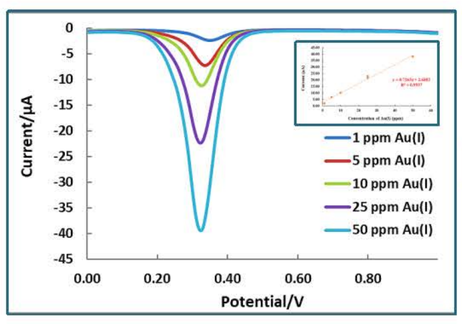

Square wave voltammograms with different concentration (1 – 50 ppm) of standard Au (I) in aqua regia

Linear range (ppm)	Regression
1.00 - 50.00	y = 0.7265x + 2.6802 (R^2 = 0.9937)

Au(I) (ppm)	RSD (%)
1	5.13
10	5.65
50	2.90

- RSD values were found in the range from 2.90% to 5.65%.
- The proposed method provided high precision for Au(I) detection.

CONCLUSION

- **The development of an electrochemical method for the detection of gold (Au(I)) was proposed.**
- **The measurement was performed on an unmodified screen-printed carbon electrode compatible with a portable potentiostat, enabling the potentiality for the on-field analysis.**
- **The linear concentration was obtained in the range of 1 – 50 ppm, which is possibly adequate to determine Au(I) in the real plating solution and the wastewater containing precious metals.**

ACKNOWLEDGEMENTS

This research has received funding support from the NSRF via the Program Management Unit for Human Resources & Institutional Development, Research and Innovation [grant number B13F660137].

BRAINPOWER CONGRESS 2023

ร่วมกันสร้างและขับเคลื่อนงานวิจัยขั้นแนวหน้า
สู่อุตสาหกรรมแห่งอนาคต

IDE LEVEL ASSESSMENT FOR THAILAND ELECTROPLATING INDUSTRY

Pongsakorn Kantichaimongkol[a], Thanyalux Wanotayan[a] and Yuttanant Boonyongmaneerat*[b]

[a]Nexus Surface Innovation Co., Ltd.; [b]Metallurgy and Materials Science Research Institute

INTRODUCTION

The metal plating industry in Thailand is a great representative of the country's potential supporting industries due to its large size (worth approximately 30,000 million baht and growing approximately 10 percent each year, data from the Ministry of Commerce) and can connect with the production of various products in the global value chain. However, the overall entrepreneurs have difficulty expanding and growth into higher value product/market, which leads most of the industry into cost intensive market. This project is focused on developing the practical IDE measurement system, "innovation driven enterprise readiness level", which is tailored made for electroplating industry.

What is innovation-driven enterprise (IDE)?

According to Professor Bill Aulet of MIT, innovation driven entrepreneurship (IDE) is defined as the pursuit of opportunities focused on products or repeatable services beyond the local market. While there isn't any set "Rule" to become IDEs but the success IDEs usually have the following characteristics.

- They focus on global markets or high value markets.
- The company is based on some sort of innovation (tech, business process, model).
- They learn from mistakes/defects and can take opportunities from the knowledge acquired from solving these problems.
- The company starts by investing time, effort & resources, but in time will have exponential growth.
- They tend to have high adaptability to market situations, changing of technology and customer. They can sustain their business.

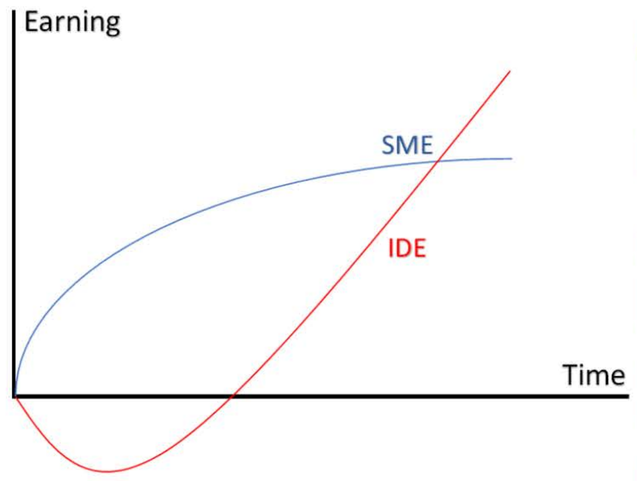

Although the characteristics of IDEs are similar to startup company, but it is actually the opposite. The startup company is an example of the new company/business which choose to be IDEs since start.

PAIN

While the importance of becoming IDEs is evident but the understanding of "what" and "how" to become IDEs is questionable, the Technical Readiness Level (TRL), a type of measurement system used to assess the maturity level of a particular technology, is also designed for projects, and clearly focused on technology. This project is a result of SMEs not knowing which stage they are in the progression to IDEs and how to further develop.

The Readiness Assessment for IDE Startups from the study of Prof. Dr. Nathasit Gerdsri, Readiness Assessment for IDE Startups: A Pathway toward Sustainable Growth, focuses on other aspects such as Manufacturing readiness level, to made the model easier for entrepreneurs to track and identify the next developing plan. This increases the model function for broader use in the startup field. This project propose further adjustment of the model for electroplating industry in Thailand SME.

ACKNOWLEDGEMENTS

This research has received funding support from the NSRF via the Program Management Unit for Human Resources & Institutional Development, Research and Innovation [grant number B13F660137].

SOLUTION

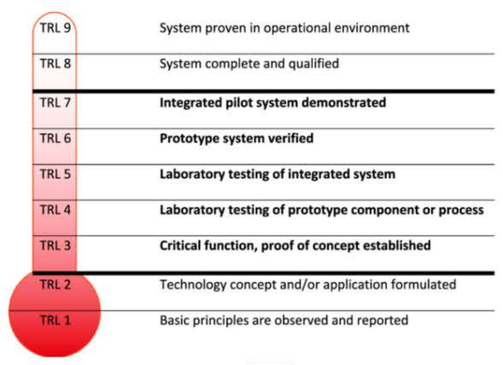

Technology Readiness Level Project

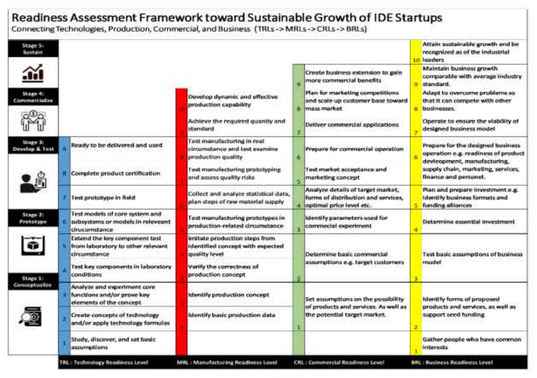

Readiness assessment Startup company

Reference: Gerdsri, N.; Manotungvorapun, N. Readiness Assessment for IDE Startups: A Pathway toward Sustainable Growth. *Sustainability* **2021**, *13*, 13687. https://doi.org/10.3390/su132413687

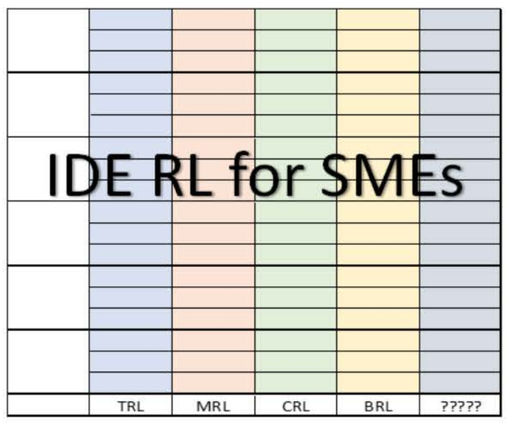

IDE Readiness Assessment for SMEs